A study of ion transport in anion exchange membranes

by

Xinzhi Cao

B.Sc. (Hons.), University of Waterloo, 2017

B.BA., Shan Dong Normal University, 2016

Thesis Submitted in Partial Fulfillment of the
Requirements for the Degree of
Doctor of Philosophy

in the
Department of Chemistry
Faculty of Science

SIMON FRASER UNIVERSITY

Spring 2024

Declaration of Committee

Name:	**Xinzhi Cao**
Degree:	**Doctor of Philosophy**
Title:	**A study of ion transport in anion exchange membranes**
Committee:	**Chair:** Robert Britton Professor, Chemistry
	Steven Holdcroft Supervisor Professor, Chemistry
	Corina Andreoiu Committee Member Professor, Chemistry
	Loren Kaake Committee Member Associate Professor, Chemistry
	Hogan Yu Examiner Professor, Chemistry
	Kunal Karan External Examiner Professor, Chemical and Petroleum Engineering University of Calgary

Abstract

To achieve net-zero energy-related and industrial CO_2 emissions by 2050, the International Energy Agency has declared that the share of renewables in the energy supply must increase from 20% in 2020 to 80% in 2050. A hydrogen-based economy is part of a solution to reduce CO_2 emissions through water electrolysis and fuel cells. The use of an anion exchange membrane enables the utilization of a non-platinum group catalyst, reducing the commercialization cost of the electrochemical cell. However, a significant concern of using anion exchange membranes is the carbonation reaction of OH^- with atmospheric CO_2, converting OH^- to larger and less mobile anions like HCO_3^- and CO_3^{2-}. This thesis analyzes the conductivity of the anion exchange membrane to explore the physicochemical properties of the membrane in various ion forms (e.g., Cl^-, HCO_3^-, CO_3^{2-}, and OH^-) with or without reinforcement composite. The conductivity was measured using linear sweep voltammetry (LSV) and electrochemical impedance spectroscopy (EIS) techniques in both the in-plane and through-plane directions. The water sorption properties of the membrane were characterized by dynamic vapour sorption (DVS). Additionally, the ion transport in the membrane is visualized using a pH indicator-doped membrane to investigate the effects of the carbonation reaction. The change of pH in the membrane is determined using UV-vis spectroscopy. As a result of water electrolysis, OH^- is generated by electrolytically splitting water. The electrolytically generated OH^- flushes out the HCO_3^- initially present in the membrane. A blueshift was observed in the UV-vis absorption spectrum of the indicator-doped membrane. Additionally, the pH range at which the indicator-doped membrane changes colour is lower than that of the indicator in an aqueous solution. This difference could be explained as a pKa change of the indicator in the membrane or an increased ion concentration in the ion-conducting domains compared to the bulk solution. Collectively, the work presented in this thesis suggests that the reinforcement substrate increased the through-plane conductivity but not the in-plane conductivity, and the conductivity in its pure OH^- form achieved by electrolytically generating OH^- via water electrolysis is 400% times higher than its HCO_3^- form.

Keywords: anion exchange membranes; fuel cells; water electrolysis; CO_2 electrolysis; pH indicator; carbonation; conductivity

Acknowledgements

I would like to express my heartfelt gratitude to my supervisor, Prof. Steven Holdcroft, for his unwavering support, guidance, and invaluable insights throughout my research. I also extend my sincere thanks to my committee members, Prof. Corina Andreoiu and Prof. Loren Kaake, for their time, expertise, and constructive feedback.

I would like to thank the following people without any specific order:

To Dr. David Novitski, for introducing me to the project, teaching me to use a lot of instruments, giving me advice on the importance of building the essential skills and habits from the start, and helping me to prepare the manuscript for my first published work at SFU.

To Dr. Alessandra Stacchini Menandro, for sharing her extensive knowledge of spectroscopy and discussing my spectroscopy results.

To Dr. Peter Mardle, for passing his knowledge and helping me understand electrochemistry more, supporting my results and suggestions for my reports.

To Dr. Patric Fortin, Dr. Qiliang Wei, Dr. Shaoyi Xu, Dr. Thomas Skalski, Dr. Chase Radford, Dr. Apurva Gangrade, Dr. Amelia Hohenadel Hinshaw, Dr. Simon Cassegrain, Dr. Anastasiia Konovalova for their support and recommendations of my research.

All members of Holdcroft group for providing help and support in the laboratory.

Table of Contents

List of Tables

List of Figures

List of Videos

Chapter 1.

Introduction

The advancement of modern civilization has brought about significant convenience and increased energy demand. However, the increased use of fossil fuels for industry, transportation, and other activities has resulted in a rise in greenhouse gas emissions, particularly carbon dioxide (CO_2), which has contributed to the issue of global warming and climate change.[1] The concentration of atmospheric CO_2 has reached 420.30 ppm, representing a nearly 50 percent increase since the start of the industrial age (retrieved from NOAA's global monitoring lab in March 2023). As a result, finding ways to reduce the production of CO_2 or actively remove it from the atmosphere has become a crucial research topic. Therefore, the use of hydrogen fuel to replace fossil fuels and the recycling of CO_2 are two potential solutions to combat the rising concentration of CO_2 in the atmosphere and thus complete the carbon cycle as shown in Figure 1. In the 1970s, John Bockris introduced the concept of a hydrogen economy, which involves the use of hydrogen as an energy carrier to replace fossil fuels which are responsible for greenhouse gas emissions and contribute to climate change.[2,3] This process has the potential of being completely carbon free because hydrogen can be produced from renewable sources such as wind and solar power and utilized to produce power for a wide range of applications, particularly as a transportation fuel due to its rapid burning speed, high effective octane number and wide flammability in air.[4] At the same time, CO_2 recycling has been proposed, where CO_2 is no longer considered a waste end-product of the carbon cycle but a cheap and abundant carbon source to produce valuable chemicals like formic acid, carbon monoxide, methanol, methane, ethylene, ethanol, and acetate.[5] This study focuses on the anion exchange membrane (AEM) which is a crucial component used in many electrochemical devices, such as anion exchange membrane water electrolysis (AEMWE) which produces H_2 fuel, anion exchange membrane fuel cell (AEMFC) which generates power using H_2 fuel, and anion exchange membrane CO_2 electrolysis (AEMCO_2E) which converts CO_2 to valuable chemicals.

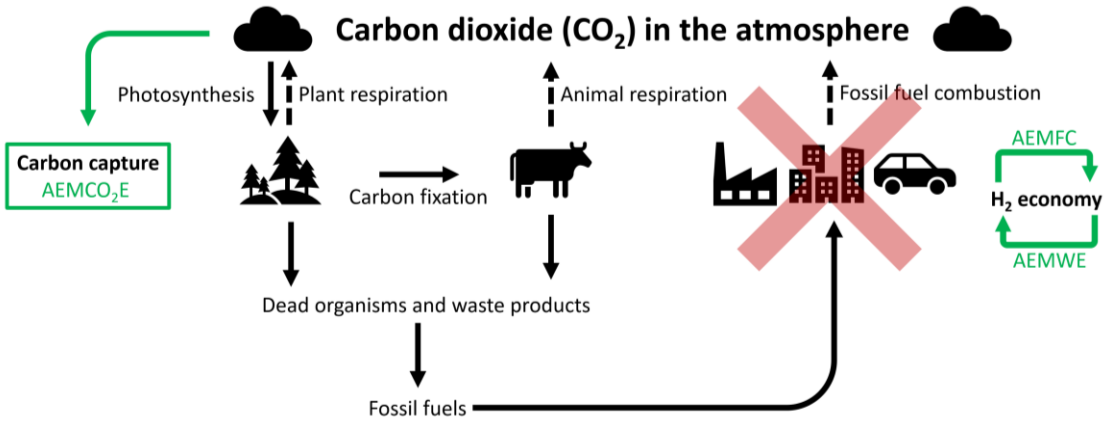

Figure 1-1. Role of anion exchange membrane in managing atmospheric carbon dioxide content in the carbon cycle.

The anion exchange membrane (AEM) is a polymer membrane electrolyte that comprises positively charged functional groups that are either bound to or integrated into the polymer backbone.[6] It has received significant research attention in various energy storage and conversion devices, including hydrogen fuel cells, water electrolysis, and CO_2 electrolysis. The fixed positively charged functional groups in AEM facilitate the transport of anions between the cathode and anode in an electrochemical system. Of particular interest are the anion exchange membrane fuel cell (AEMFC) that convert chemical energy stored in H_2 fuel to electricity without producing CO_2,[7–9] anion exchange membrane water electrolysis (AEMWE) that produces high-purity H_2 fuel by consuming only water and clean renewable energy such as wind and solar energy,[10–13] and anion exchange membrane CO_2 electrolysis (AEMCO_2E) that converts atmospheric CO_2 into valuable chemical products.[14,15] These applications contribute to maintaining atmospheric CO_2 content levels and preventing future global warming. In this study, it is important to investigate the properties and performance of anion exchange membranes in electrochemical devices to explore their potential as a reliable method of recycling atmospheric CO_2 and reducing the dependence on fossil fuels.

1.1. Anion exchange membrane in H_2 fuel cell

A fuel cell is an energy conversion device that directly converts the chemical energy of fuel into electrical energy through an electrochemical process. Compared to the multi-step process found in conventional combustion-based heat engines that

involve converting chemical energy to thermal, mechanical, and finally, electrical energy, the fuel cell's unique one-step process makes it a leading candidate for the energy conversion systems of the future. For instance, fuel cells offer an effective and eco-friendly means of converting energy, and they are well-suited for use with sustainable resources and contemporary energy carriers such as hydrogen. In addition, fuel cells operate quietly without noise or vibrations due to their stationary nature, and their modular design makes them simple to construct and adaptable for use in various applications.

Fuel cells have come a long way since Sir William Grove's gas battery experiment in the early 1800s.[1] A fuel cell is typically described as a device composed of three major components: a fuel electrode (anode), an oxidant electrode (cathode), and an electrolyte sandwiched between them. In electrochemistry, oxidation is defined as the process in which electrons are liberated and the electrode where oxidation takes place is referred to as the anode. Reduction is defined as the process in which electrons are consumed and the electrode where reduction takes place is referred to as the cathode. In an AEMFC, oxygen (O_2) is conveyed from a gas-flow stream to the cathode, where it undergoes a reduction to generate hydroxide ions as described in the oxygen reduction reaction (ORR) shown in Equation 1-1. The hydroxide ions (OH^-) migrate through the AEM from the cathode to the anode where they react with hydrogen (H_2) to generate electrons and water as described in the hydrogen oxidation reaction (HOR) as shown in Equation 1-2.

Equation 1-1 $$\frac{1}{2}O_2 + H_2O + 2e^- \rightarrow 2OH^-$$ (Cathode)

Equation 1-2 $$H_2 + 2OH^- \rightarrow 2H_2O + 2e^-$$ (Anode)

Because the ions and electrons produced at one electrode are consumed at the other electrode to maintain charge balance and complete the circuit. It is important to efficiently transport the ions and electrons from the electrode where they are generated to the electrode where they are consumed. The transport of electrons can be achieved through an electrically conductive pathway. However, ions exhibit significantly larger sizes and masses compared to electrons. As a result, ion transport through the electrolyte generates higher resistance, which ultimately compromises the performance of fuel cells. An effective strategy to mitigate this issue involves the utilization of anion exchange membranes. By minimizing the thickness of the membrane, the distance

between electrodes can be reduced, thereby optimizing fuel cell performance. The present study aims to systematically investigate the conductive properties of different anion exchange membrane materials.

1.1.1. Characterize anion exchange membrane using in-situ fuel cell performance

The generation of electricity through a fuel cell involves three distinct processes, namely electrochemical reaction, charge transport, and reactant delivery and product removal. These processes can be characterized by activation losses, ohmic losses, and concentration losses, as represented in the polarization curve, as shown in Figure 1-2.

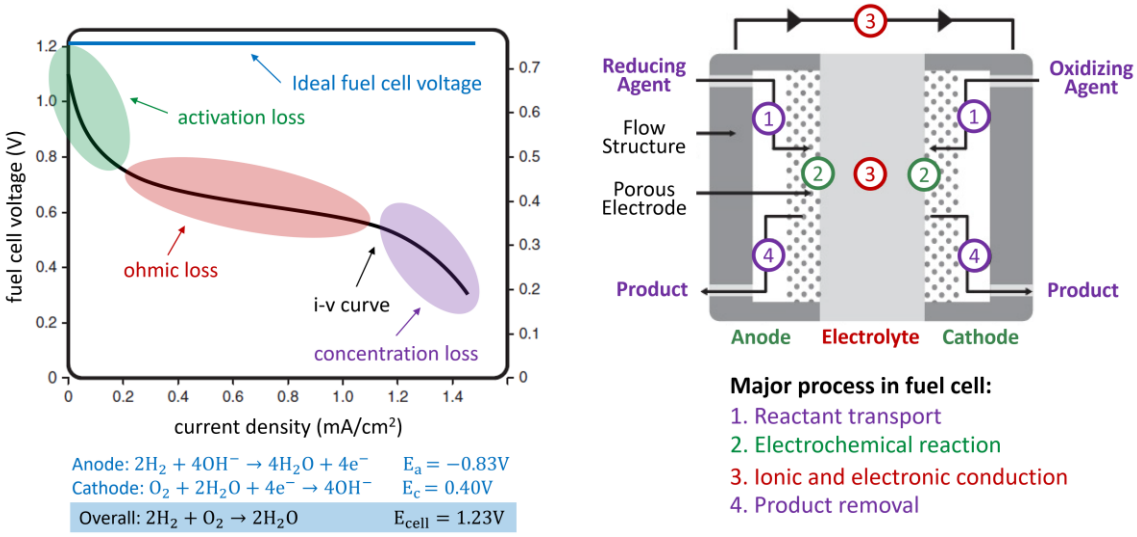

Figure 1-2. Schematic representation of the influence of three major losses on the shape of an H_2 fuel cell polarization curve. Adapted from ref[16]

The electrochemical reaction in a fuel cell involves the hydrogen oxidation reaction (HOR) at the anode and the oxygen reduction reaction (ORR) at the cathode. The electrochemical reaction rate determines the current generated by the fuel cell. Due to the alkaline environment, anion exchange membrane fuel cells offer the advantage of using non-platinum group metal catalysts. Improved catalyst and electrode design shown in Figure 1-3 can enhance the electrochemical rates. Both the cathode and anode reaction rate losses contribute to activation losses in the polarization curve.[16]

Charge transport refers to the transport of ions and electrons in a fuel cell. In an anion exchange membrane fuel cell, electrons (e^-) are generated through an oxidation process at the anode and consumed through a reduction process at the cathode. Meanwhile, hydroxide ions (OH^-) are produced at the cathode and consumed at the anode. Ions are more massive and larger than electrons; hence, ion transport is more challenging than electron transport. A membrane electrolyte with high ionic conductivity and electronic insulation is necessary for efficient charge transport. The search for materials with high ionic conductivity is vital. The resistance to charge transport contributes to ohmic losses in the polarization curve.[16]

Reactant delivery involves the continuous supply of fuel (e.g., H_2) and oxidant (e.g., O_2) to the fuel cell, particularly at a high current. Failure to supply the reactant adequately can starve the cell. Product removal involves removing the products (e.g., water) from the fuel cell. Failure to remove them can lead to their buildup, eventually strangling the cell and preventing further reactant reaction. Flow field plates, as depicted in Figure 1-3, contain many fine channels that distribute the gas flow over the fuel cell's surface. The process of reactant transport and product removal is known as mass transport, which contributes to concentration losses in the polarization curve.[16]

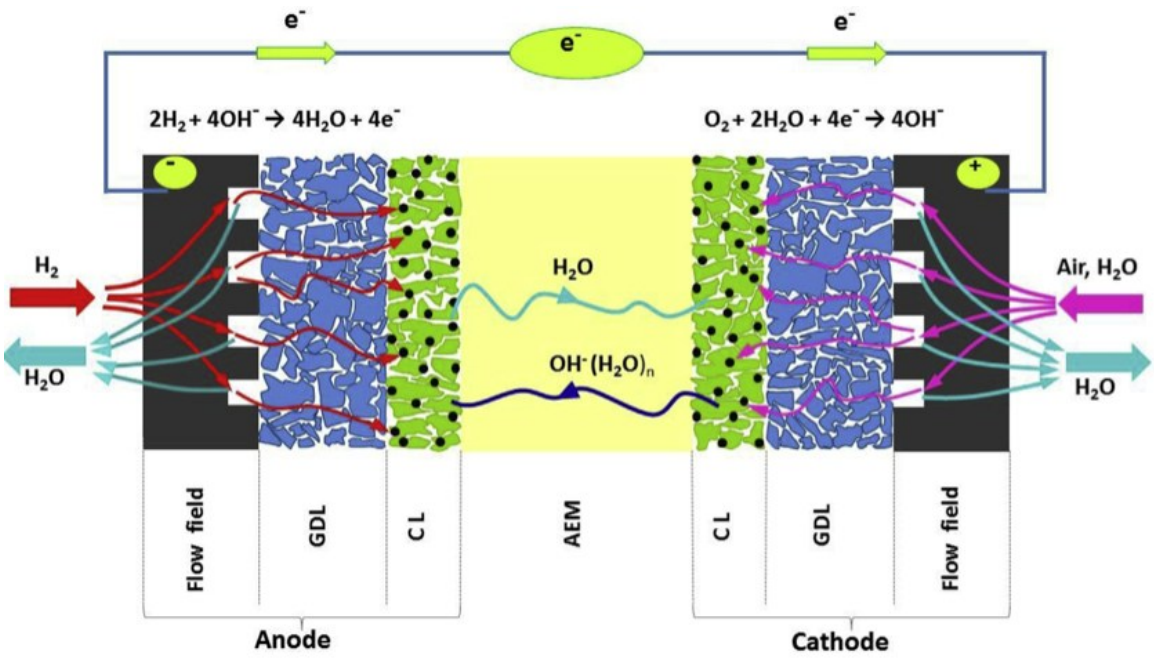

Figure 1-3. Schematic of the electrode reactions and ions, electrons and water transport in an anion exchange membrane fuel cell operated with H_2 in the anode and O_2 in the cathode. Adapted from ref[8]

1.1.2. Characterizing anion exchange membrane using ex-situ conductivity cell

Due to the series connection of all the layers illustrated in Figure 1-3, it is challenging to experimentally differentiate the contribution of ohmic losses from various components, such as electrical interconnections, anode and cathode electrodes, anode and cathode catalyst layers, and contact resistance at each interface between layers. Because the membrane electrolyte resistance is the primary factor contributing to the ohmic losses observed in the polarization curve, it is important to isolate the membrane electrolyte from the rest of the fuel cell and study its properties.

Charge transport is facilitated by driving forces applied on the charge carriers (e.g. OH-) such as electrical driving forces (potential), chemical potential driving forces (concentration), and mechanical driving forces (pressure) as summarized in Table 1-1 molar flux (J) quantifies the rate at which charges move through a material and is influenced by the coupling coefficient between the driving force and flux. For conduction transport, conductivity (σ) measures the material's ability to permit charge flow in response to an electric potential gradient ($\frac{dV}{dx}$). For diffusion transport aka migration, diffusivity (D) characterizes the material's ability to permit charge flow in response to a concentration gradient ($\frac{dc}{dx}$). For convection transport, viscosity (μ) measures the material's resistance to charge flow in response to a pressure gradient ($\frac{dP}{dx}$).[16]

Table 1-1. Summary of charge transport process. Adapted from ref.[16]

Transport process	Driving force	Coupling coefficient	Flux $\left(\frac{mol}{cm^2 \times s}\right)$
conduction	Electrical potential gradient $\left(\frac{dV}{dx}\right)$	Conductivity (σ)	$J = \frac{\sigma}{\lvert z_i \rvert F}\frac{dV}{dx}$
diffusion (aka migration)	Concentration gradient $\left(\frac{dc}{dx}\right)$	Diffusivity (D)	$J = -D\frac{dc}{dx}$
convection	Pressure gradient $\left(\frac{dP}{dx}\right)$	Viscosity (μ)	$J = \frac{Gc}{\mu}\frac{dP}{dx}$

In an anion exchange membrane fuel cell, the ion conductor (membrane electrolyte) exists in a solid state, meaning there is no pressure gradient. The reaction at the cathode generates hydroxide ions (OH^-) through oxygen reduction reaction (ORR), and the anode consumes them through hydrogen oxidation reaction (HOR).

This accumulation and depletion of hydroxide ions create a potential and concentration gradient that drives the transport of hydroxide ions from the cathode to the anode through the membrane electrolyte. The background concentration of ionic charge carriers in the anion exchange membrane is generally high enough to eliminate significant concentration gradients. Therefore, ex-situ measurement of the conductivity of an anion exchange membrane (σ_{AEM}) is the most critical parameter to compare the different membranes synthesized across different laboratories.

1.2. Anion exchange membranes in water electrolysis

Nowadays, hydrogen is mainly produced by steam-reforming natural gas as the methane source, where high-temperature steam (700°C-1000°C) reacts with methane in the presence of a metal-based catalyst to produce hydrogen.[17,18] However, hydrogen produced by steam reforming contains a high concentration of carbonaceous species (e.g. CO). Anion exchange membrane water electrolysis produces high-purity hydrogen (≈100%) via an electrochemically water-splitting reaction as shown in Equation 1-3 and Equation 1-4[19].

Equation 1-3 $2\mathrm{H_2O} + 2\mathrm{e^-} \rightarrow 2\mathrm{H_2} + 2\mathrm{OH^-}$ (Cathode)

Equation 1-4 $2\mathrm{OH^-} \rightarrow \mathrm{H_2O} + \frac{1}{2}\mathrm{O_2} + 2\mathrm{e^-}$ (Anode)

Water is considered to be one of the most stable substances in thermodynamics, and separating its elements into hydrogen and oxygen molecules requires a significant amount of energy input.[20] To obtain hydrogen gas and oxygen gas from water, it is necessary to overcome the equilibrium cell voltage, which represents the potential difference between the anode and cathode in the open cell. The minimum cell voltage required for decomposition of water is know as the equilibrium cell voltage ($\mathrm{E_{rev}}$) is. At standard temperature and pressure (STP), the equilibrium cell voltage is 1.23 V as described by Equation 1-5 and the change in Gibbs free energy ($\Delta\mathrm{G}$) of the reaction is + 237.2 kJ mol^{-1} as described by Equation 1-6.[21] As indicated by the positive the Gibbs free energy, the process of water splitting is non-spontaneous. Therefore, the actual cell voltage of an operating electrolysis is significantly higher than the theoretically predicted reversible cell voltage by thermodynamics. To facilitate the dissociation of water, an external DC power source is applied to each electrode to

modify its Fermi level and create a bracketing effect around the energy levels of the involved redox couples.[22]

Equation 1-5 $$E_{rev} = E_{cathode} - E_{anode}$$

Equation 1-6 $$\Delta G = -nFE$$

Conventional alkaline water electrolysis (AWE) setup involves a liquid alkaline electrolyte containing approximately 20-30% KOH and two metallic electrodes which are submerged in the solution. A diaphragm is placed between the two electrodes (as shown in Figure 1-4) to prevent the product gases from mixing and ensure efficient and safe operation. However, the diaphragm has some operational limits. First, the diaphragm does not entirely prevent cross-diffusion of the gases. When oxygen crosses into the cathode chamber, it reduces the electrolyzer's efficiency since it reacts with hydrogen, leading to the formation of water. This issue is particularly acute at low loads (<40%) where the production rate of oxygen decreases, resulting in an unwanted and hazardous increase in the concentration of hydrogen (lower explosion limit >4 mol% H_2).[23] Second, the formation of gas bubbles tends to migrate upwards along the electrode surface due to gravity. At elevated current densities, these bubbles can accumulate and create a contiguous layer of non-conductive gas across the entire electrode surface, leading to a screening effect which increases in energy consumption and promotes gas transport across the diaphragm.[24]

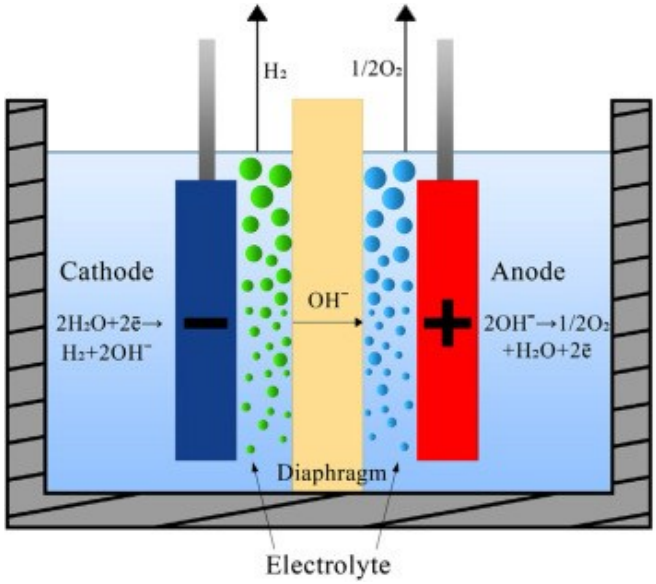

Figure 1-4. Schematic of the operating principle of an conventional alkaline water electrolysis cell. Adapted from ref[25]

Anion exchange membrane water electrolysis (AEMWE) cell uses an anion exchange membrane as the electrolyte (as shown in Figure 1-5). The use of solid polymer electrolyte provides many advantages such as high hydroxide conductivity, low gas cross over, compact system design and high operation pressure. Since gas evolution occurs on the "back side" of the electrodes, opposite to the membrane, the screening effect is less significant in anion exchange membrane electrolysis.[26] In addition, the compact system design enables high operational pressures are achievable. The high-pressure operation reduces the amount of energy required for further compressing and storing the hydrogen, while also minimizing the volume of the gaseous phase at the electrodes, leading to improved product gas removal. The high operational pressure also reduces the expansion and dehydration of the membrane, which preserves the integrity of the catalytic layer.[27]

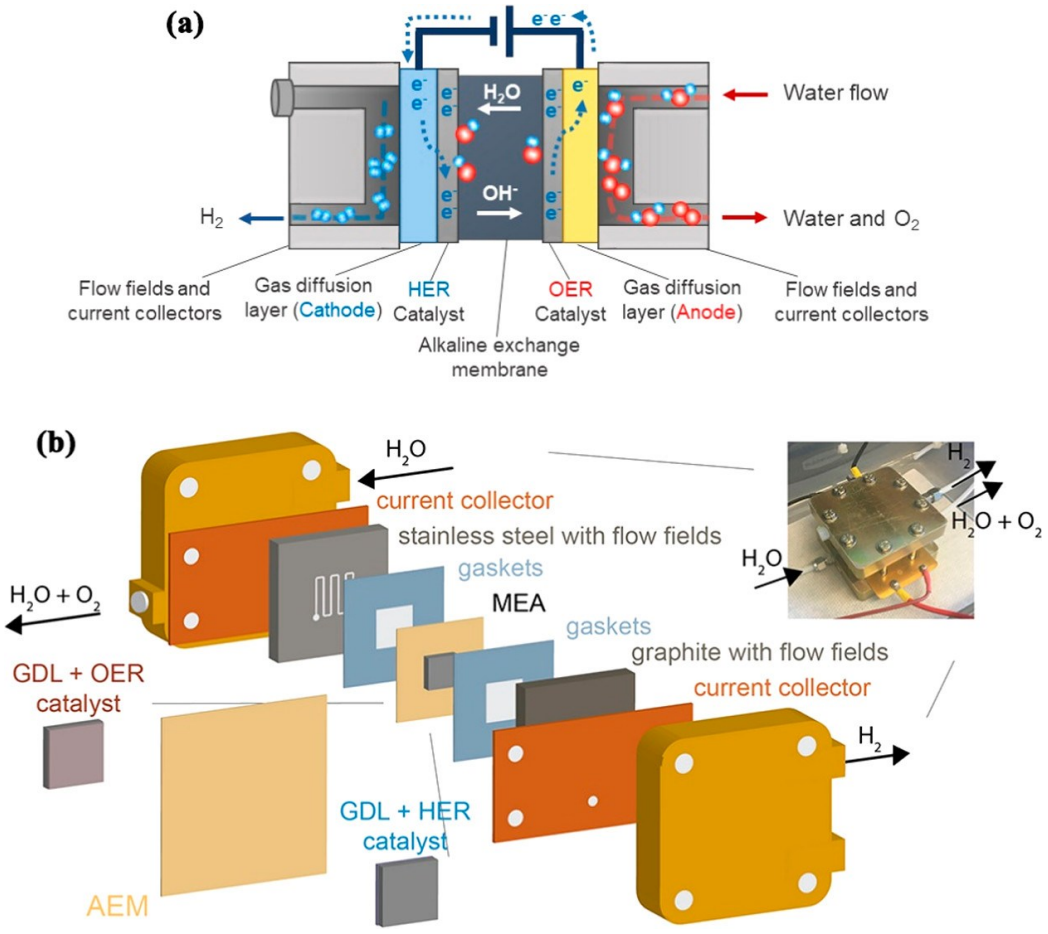

Figure 1-5. **(a) Schematic of the operating principle of an anion exchange membrane water electrolysis cell. (b) Schematic cross section of an anion exchange membrane water electrolysis system. Adapted from ref [28]**

1.2.1. Anion exchange membrane conductivity under various hydration state

When compared to fuel cell operation, the anion exchange membrane in water electrolysis is exposed to the liquid phase of water and is fully hydrated, rather than being humidified by the gas and equilibrated with water vapour (as shown in Figure 1-8). Consequently, it is crucial to evaluate the performance of the membrane under various hydration conditions.[29–31]

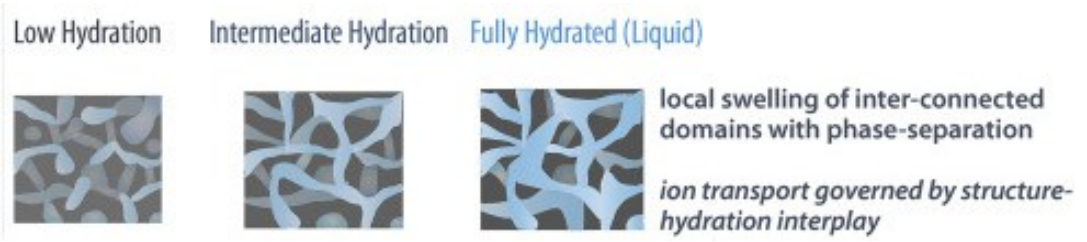

Figure 1-6. Schematic of anion exchange membrane at various hydration level. Adapted from ref[31]

1.3. Anion exchange membranes in CO_2 electrolysis

CO_2 electrolysis is an electrochemical process that involves the reduction of the C−O bonds in CO_2, resulting in the formation of a wide range of products. The products generated depends on the number of electrons transferred and the coupling CO_2 molecules. The products generated include C_1 compounds such as carbon monoxide and formic acid, C_2 compounds such as acetic acid, ethylene, and ethanol, and C_3 compounds such as n-propanol (as shown in Figure 1-7).[32]

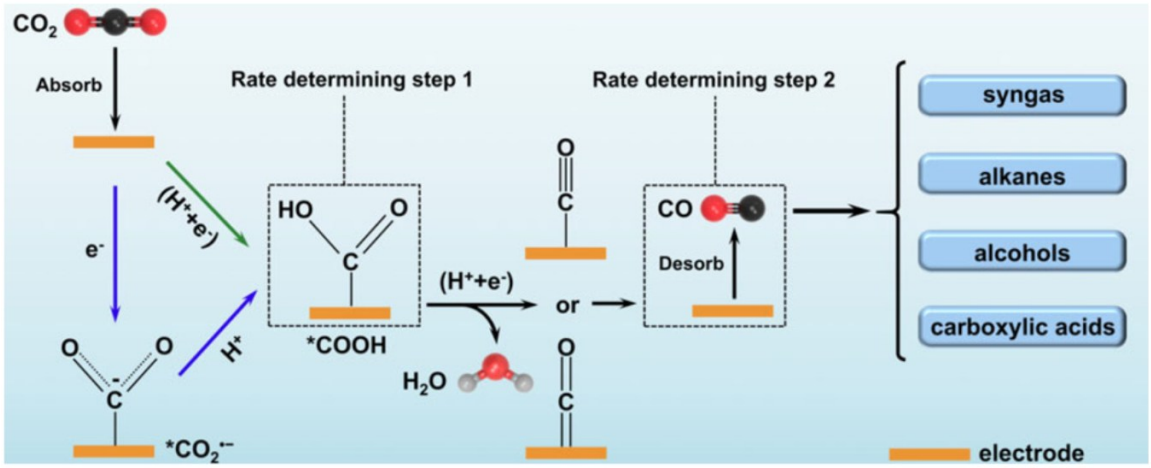

Figure 1-7. Possible reaction pathways for the electrocatalytic reduction of CO_2. Adapted from ref[32]

At cathode, the CO_2 molecules move towards the boundary between the Gas Diffusion Electrode (GDE) and the catalyst layer. At this interface, the CO_2 is reduced into a specific product and OH^- is released through CO_2 reduction reaction (CO_2RR) as shown in Equation 1-7.

Equation 1-7 $$xCO_2 + (2x + y - z)H_2O + (4x + y - 2z)e^- \rightarrow C_xH_yO_z + (4x + y - 2z)OH^-$$

Hydroxide reacts with CO_2 to form bicarbonate and carbonate through carbonation reactions as described in Equation 1-8 and Equation 1-9. Therefore, the charge carrier which could be OH^-, HCO_3^-, CO_3^{2-} or a mixture of them, then transport from cathode to anode through the anion exchange membrane.[33,34]

Equation 1-8 $$CO_2 + OH^- \rightarrow HCO_3^-$$

Equation 1-9 $$HCO_3^- + OH^- \rightarrow CO_3^{2-} + H_2O$$

At the anode, the anions are then converted to O_2 and CO_2 according to Equation 1-10 and Equation 1-11. By observing a ratio of CO_2/O_2, one could imply whether OH^- has participated the charge carrying role: less than 2:1, it implies both CO_3^{2-} and OH^- are transported; otherwise only CO_3^{2-} is transported.[34]

Equation 1-10 $$2OH^- \rightarrow O_2 + 2H^+ + 4e^-$$

Equation 1-11 $$2CO_3^{2-} \rightarrow 2CO_2 + O_2 + 4e^-$$

Numerous configurations of electrolyzer have been utilized, with the majority employing Kenis-type designs, which integrate the gas diffusion electrode (GDE),

catalyst and ion-exchange membrane into a single unit known as the membrane electrode assembly.[35] The liquid-phase electrolyzer is the most frequently utilized flow cell as shown in Figure 1-8-a It comprises of three separate channels that are fed with CO_2 gas, catholyte, and anolyte, respectively. The gas diffusion electrode, which contains the catalyst, is in contact with the electrolyte and continuously receives gas-phase CO_2 from the rear. An ion-exchange membrane is utilized to separate the anolyte and catholyte. This membrane plays a crucial role in preventing the CO_2 reduction reaction products and O_2 from crossing over, where they could potentially be oxidized or reduced back into CO_2 and H_2O.[36] In comparison with liquid-phase electrolyzers, gas-phase electrolyzers (as shown in Figure 1-8-b) have lower ohmic losses and can be pressurized easily due to the smaller electrolyte pumps and flow fields. Moreover, the elimination of electrolyte reduces the possibility of electrolyte impurities depositing on catalysts and the generation of bicarbonate/carbonate. However, if liquid products are produced, they will accumulate in the GDE and hinder gas diffusion through the electrode.

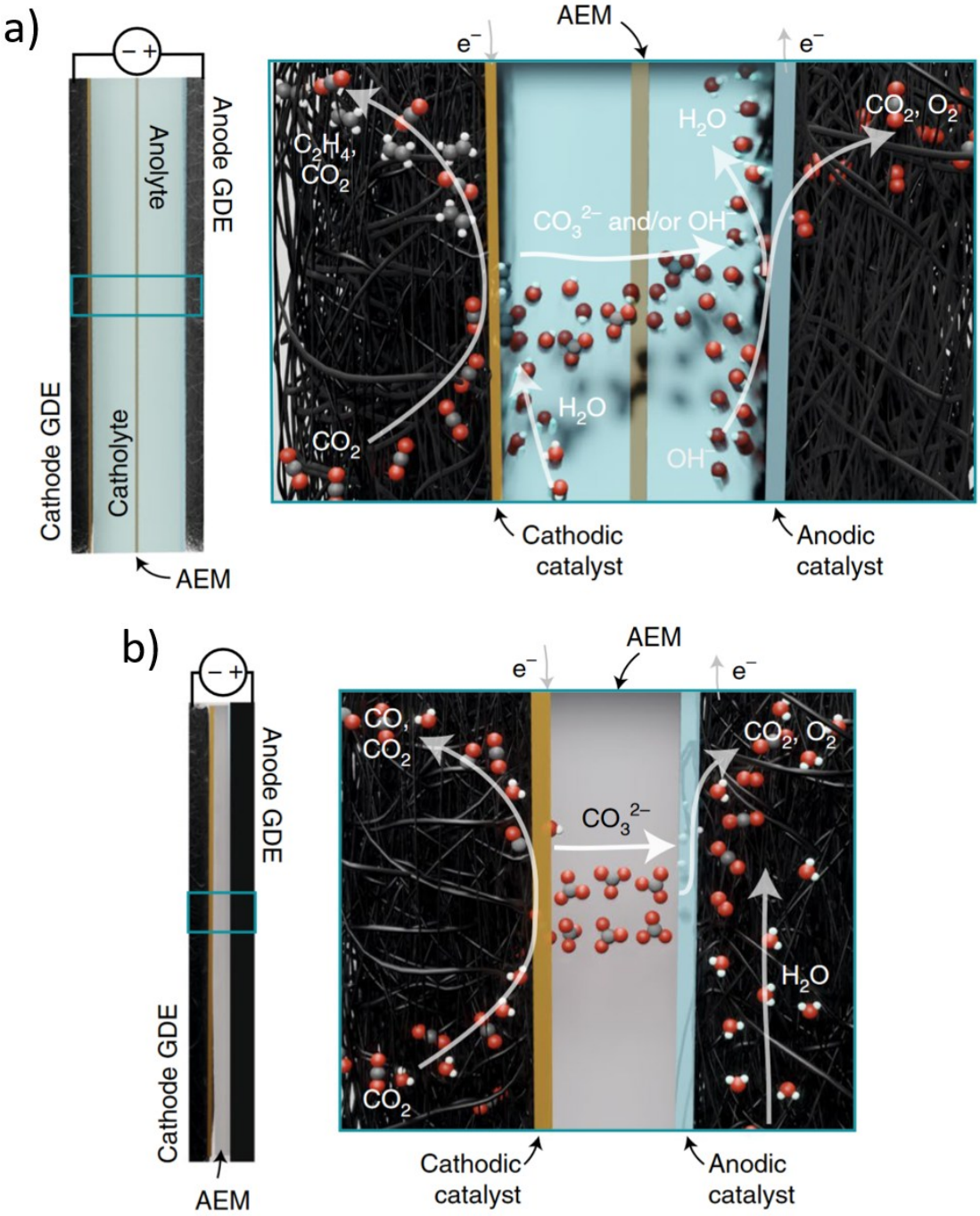

Figure 1-8. **(a). Schematic of an liquid-phase electrolyzer for ethylene formation with an AEM (b). Schematic of a gas-phase electrolyzer for CO production with an AEM. Adapted from ref[37]**

1.3.1. Anion exchange membrane conductivity in various counter-ion forms

To understand the effect of CO_2 on the AEM characteristics, it is important to clarify the relationship between the membrane conductivity and the conductivity of each ion. The membrane conductivity can be described as the sum of individual ions' conductivity, as given by Equation 1-12 where z_i is the ionic charge of the ion i, F is the Faraday constant, C_i is concentration of each ion i, and μ_i is the mobility of each ion i. Since z_i and F are constants, the conductivity mainly depends on the concentration of the anion and its mobility. Since OH^- ions possess a mobility 4 times higher than HCO_3^- and CO_3^{2-} ions, the membrane conductivity is expected to decrease if OH^- is converted to HCO_3^- and CO_3^{2-} as a result of the carbonation process. This is particularly important in anion exchange membrane CO_2 electrolysis. Therefore, the anion exchange membrane conductivity is studied and compared in different counter ion forms.

Equation 1-12 $$\sigma_{AEM} = \sum \sigma_i = \sum z_i \, F \, C_i \, \mu_i$$

1.4. Thesis Overview

This study focuses on characterizing the physicochemical properties of an anion exchange membrane for applications in H2 fuel cells, water electrolysis, and CO2 reduction.

Chapter 1 introduces the background knowledge of anion exchange membranes and the operating principles of electrochemical cells. Chapter 2 describes the experimental techniques used to characterize the physicochemical properties of the membrane. Chapter 3 focuses on studying the effect of reinforcement substrate on the membrane's properties, particularly its Cl^- conductivity. Chapter 4 introduces a method of using a pH indicator-doped membrane to visualize the ion flushing process during water electrolysis. Chapter 5 quantitatively measures the UV-vis absorbance change of the pH indicator-doped membrane and investigates the differences of absorption spectra of the indicator in aqueous solution and in the membrane. Chapter 6 summarizes the projects in the thesis and points out the direction of future work.

Chapter 2. Materials and Techniques

2.1. Cationic polymer electrolyte

2.1.1. Materials

Polymer electrolytes conduct anions because they contain cationic functional groups. These cationic functional groups can be covalently bound to the backbone through extended alkyl or aromatic side chains with varying lengths or directly bound to the backbone via CH_2 bridges[38–43]. Alternatively, the cationic functional groups can be part of the backbone itself[44–48] (e.g., polybenzimidazolium). In this study, the primary interest is on the heterocyclic system of poly(benzimidazolium) systems where the positive charges are part of the polymer backbones[49–52]. The poly(benzimidazolium) offers good stability as the integrity of the polymer backbone is directly related to the stability of the benzimidazolium group and there are only a few possible degradation routes for poly(benzimidazolium) [47,53,54]. The polymer electrolyte used in this study includes the poly[2,2′-(2,2″,4,4″,6,6″-hexamethyl-p-terphenyl-3,3″-diyl)-1,1′,3,3′-tetramethyl-(5,5′-bibenzimidazolium)] (**HMT-PMBI**), poly(2-(2,6-dimethylphenyl)-1,3-dialkyl-4,5-diphenyl-1H-imidazolium) (**PAImR$_1$R$_2$**), and poly(2,2′-(2,3,5,6-tetramethyl)-1,4-phenylene)bis-(1,3-dialkyl-4,5-diphenyl-1H-imidazolium) (**TMP-PMPI- R$_1$R$_2$**).

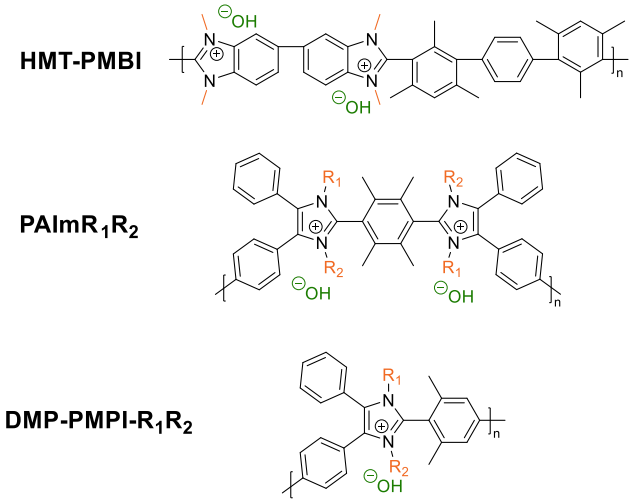

Figure 2-1. Comparison of the chemical structure of the different cationic polymers used in this study: HMT-PMBI, PAImR$_1$R$_2$ and DMP-PMPI-R$_1$R$_2$ in its OH$^-$ form.

The chemical structure of HMT-PMBI is shown in Figure 2-2, which can be controllably methylated from 50% to 100%. For a 50% dm derivative, the polymer would be non-conductive as there are no cationic functional groups. As the degree of methylation (% dm) increases, it is expected that the polymer would contain more positively charged functional groups. However, it has been observed that when the degree of methylation exceeds 92%, the polymer becomes soluble in water[6,55]. This solubility in water renders the polymer unsuitable for utilization in electrochemical systems where water participates in the electrochemical reaction. The 89% dm HMT-PMBI exhibits a good balance of high conductivity and low water uptake and therefore is chosen for this study.

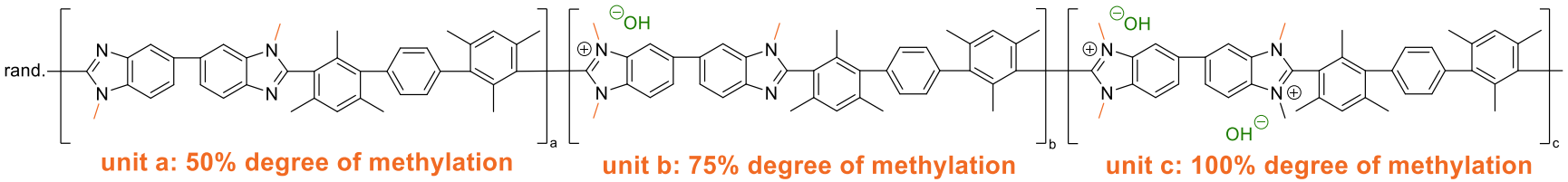

Figure 2-2. Chemical structure of HMT-PMBI in its OH^- form, where dm represents the degree of methylation (of the N atoms): unit a represents 50% dm, unit b represents 75% dm and unit c represents 100% dm.

The chemical structure of PAImR$_1$R$_2$ is shown in Figure 2-5, where the imidazoles can be alkylated using different alkyl side chains such as methyl, ethyl, propyl, or butyl groups.

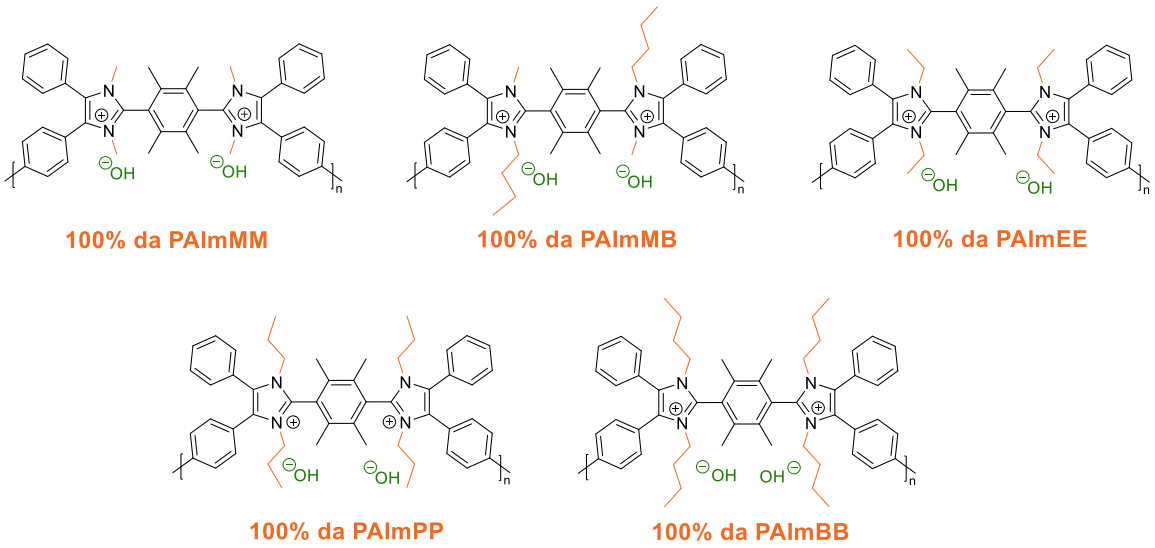

Figure 2-3. Chemical structure of PAImR$_1$R$_2$ in its OH$^-$ form, where da represents the degree of alkylation (of the N atoms) and R$_1$R$_2$ represents the alkyl chains: M=methyl, E=ethyl, P=propyl, B=butyl

DMP-PMPI-R$_1$R$_2$ exhibits structural isomers in which two repeating units are arranged in head-to-head, head-to-tail, and tail-to-tail configurations as shown in Figure 2-4.

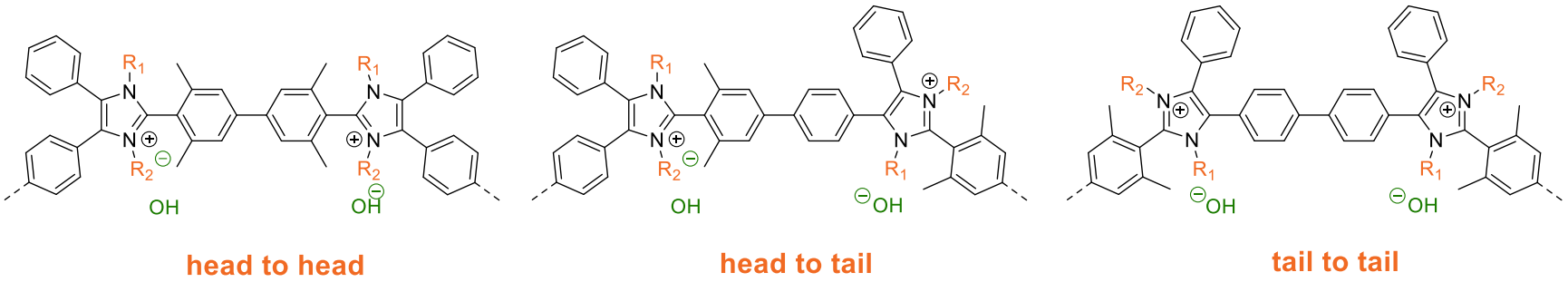

Figure 2-4. Structural isomers of DMP-PMPI-R_1R_2 in its OH^- form showing the head to head, head to tail and tail to tail configurations of two repeating units.

In an electrochemical system, the polymer electrolyte can be used in two forms as shown in Figure 2-5: as a thin membrane which was referred to as the anion exchange membrane, or as an additive in the catalyst layer which was referred to as the anion exchange ionomer[56]. The anion exchange membrane can be produced by casting a polymer electrolyte solution onto a substrate, followed by gradual evaporation of the solvent in a ventilated oven at elevated temperatures. Subsequently, the membranes are peeled off from the substrate. The anion exchange ionomers are added to the catalyst ink, which can be either deposited on both sides of the membrane to form the catalyst-coated membranes (CCMs) or deposited on both sides of the gas diffusion electrode (GDL) to form the catalyst-coated substrates (CCSs). The addition of polymer electrolyte in the catalyst layer allows the anions to transport from the porous gas diffusion electrode to the anion exchange membrane electrolyte This, in turn, promotes the electrochemical reaction occurred at the triple-phase boundaries (TPBs), which are formed at the interfaces between the gas-phase pores, the electrically conductive electrode, and the ion-conductive electrolyte.

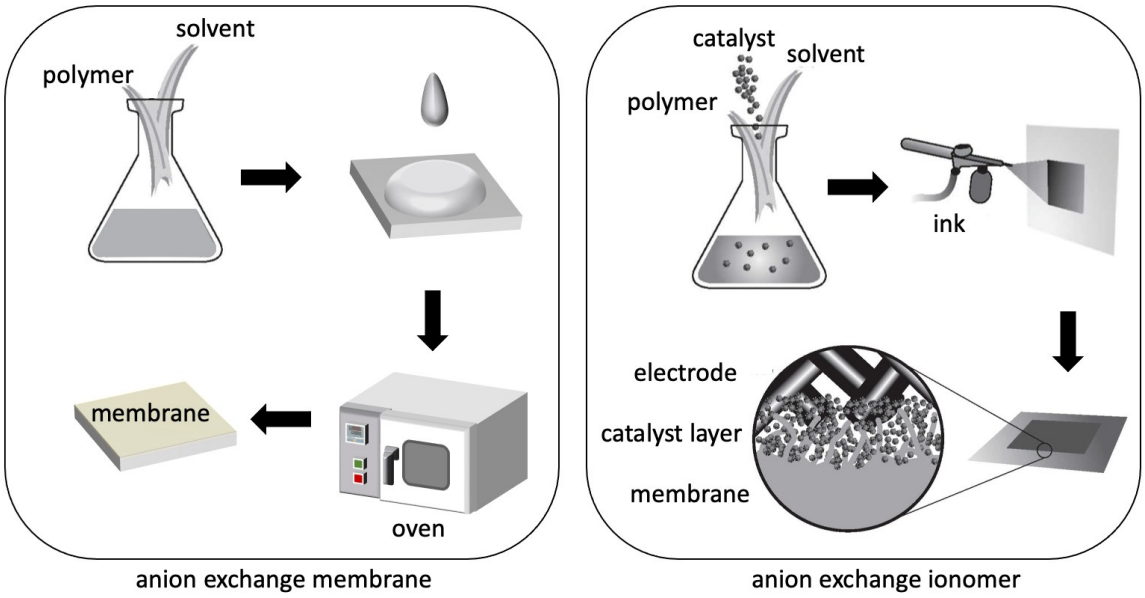

Figure 2-5. Schematic representation of the use of the polymer electrolytes in an electrochemical system as the anion exchange membrane or as the anion exchange ionomer. Adapted from ref[16]

2.1.2. Experimental procedure of casting the cationic polymer electrolyte to an anion exchange membrane

Membranes were cast from at 7.5 wt% DMSO solutions, which were prepared by dissolving 0.750 g of polymer in 10.00 g of DMSO by constant stirring overnight at room temperature. The polymer solutions were then vacuum filtered through a glass fiber filter paper before spreading onto a glass plate. The thickness of the polymer solutions was controlled using a casting table equipped with a casting blade from RK PrintCoat Instrument Ltd. The height of the casting blade was adjusted based on the desired thickness of the resulting membrane. Typically, a membrane of 25 μm thickness was achieved by setting the casting blade to 650 μm height to level a 7.5 wt% polymer solution. To ensure all the solvent were removed, the leveled polymer solutions were heated at 86 ± 1 °C for at least 16 hours in a dust-free oven. The membranes were peeled off by immersing the glass plate in a large bucket filled with deionized water. The membranes were dried under vacuum at room temperature overnight to remove the excess water and stored in the dry form before use.

2.1.3. Experimental procedure of adding cationic polymer to the catalyst ink as anion exchange ionomer

For anion exchange membrane water electrolysis:

Preparation of catalyst inks containing anion exchange ionomers:

The ionomer solution was prepared by dissolving the desired amount of ionomer in a solvent mixture consisting of ethanol and water (10:1 ratio). The catalyst slurry was prepared by adding the desired amount of catalyst in a solvent mixture consisting of isopropanol and water (1:1 ratio) and sonicated in an ice bath for at least 15 mins. After that, the ionomer solution was added dropwise to the catalyst slurry, followed by another round of sonication in an ice bath for 10 mins. The catalyst inks had a total solid content of 2% by weight, which included both the catalyst and the ionomer. For cathode ink, the commercial Pt/C (60% on high surface area carbon, Alfa Aesar) was used as the catalyst, and the ionomer made up 25% of the total solid content. Whereas for anode ink, the Ir black (99.8%, Alfa Aesar) was used as the catalyst, and the ionomer constituted 7% of the total solid content.[52]

Spray catalyst inks:

To prepare the catalyst ink for spray coating, an additional sonication step was performed using a probe ultrasonicator (Branson Digital Sonifier model 102c) in an ice bath. The ultrasonicator was set to an amplitude of 40%, and the sonication process was carried out for a duration of 5 minutes. The anode catalyst ink was deposited onto commercially available titanium porous electrode (Bekaert) by spray coating to form a catalyst coated substrate (CCS). Similarly, the cathode coated substrate was fabricated by spraying the cathode catalyst ink onto the carbon paper (Fuel Cell Store).

For anion exchange membrane fuel cells:

Preparation of catalyst inks containing anion exchange ionomers:

For the catalyst coated membrane, the cathode catalyst Pt/C (46.5 wt%, TKK) and anode catalyst PtRu/C (32.7wt% Pt and 16.9 wt% Ru, TKK) were utilized. Both the cathode and anode inks were formulated by dispersing 1 wt% solids in a 3/1 (v/v) mixture of methanol and water. To achieve the desired catalyst/ionomer (w/w) ratio, the inks were supplemented with an appropriate amount of ionomer solution. Specifically, a 3 wt% Aemion$^{+®}$ or Aemion$^{®}$ ionomer solutions were added to the inks. This resulted in a catalyst/ionomer ratio of 80%/20% (w/w) for the cathode catalyst ink and 85%/15% (w/w) for the anode ink. The prepared inks underwent a dispersion process utilizing ultrasonication in an ice-filled Branson 1510 sonication bath for a duration of 60 minutes prior to spray coating.

For the direct membrane deposition (DMD), 5 wt% of Aemion$^{+®}$ was dispersed in a 9/1 (w/w) solution of methanol and water mixture at 40°C for 4 hours via constant stirring with a magnetic stir bar. The cathode catalyst, Pt/C (50% Pt on carbon black, Umicore Elyst Pt50 0550), and the anode catalyst, Pt/Ru/C (40 wt% Pt/20 wt% Ru, Thermosher), were selected. Aemion$^{+®}$ served as the ionomer for both cathode and anode catalyst inks, with a solid content of 2 wt% in a in a 3/1 (w/w) ratio mixture of methanol and water. The cathode ink exhibited a catalyst/ionomer weight ratio of 80%/20%, while the anode ink had a ratio of 85%/15%. To achieve a homogeneous dispersion, the inks were ultrasonicated in an ice bath using an ultrasonic horn (Hielscher UIS250V) for a duration of 1.5 hours. For the direct deposition of the solid polymer electrolyte layers, the ionomer dispersion solutions were then diluted until the ionomer content reached 1.5 wt% by adding methanol.

Spray catalyst inks:

The catalyst coated membranes (CCMs) were fabricated by spray coating the catalyst inks directly onto the Anion Exchange Membranes (AEMs) using a SonoTek "ExactaCoat" system with an AccuMist nozzle. The spray system operated at a frequency of 120 kHz (2 W) and had a nozzle diameter ranging from 2 to 6 mm, with a path speed of 75 mm/s. The shaping air pressure was set to 0.8, and the ink flow rate was maintained at 0.30 mL/min. The AEMs were securely held onto a vacuum table at a temperature of 80°C, and a PTFE template was used to ensure a sprayed active area of 5 cm^2. The catalyst loading on both the cathode and anode sides was confirmed to be 0.5 mg Pt/cm^2 by a analytical balance.

For the preparation of the Membrane-Electrode-Assemblies (MEAs) via the Direct Membrane Deposition (DMD) process, the ionomer ink was directly sprayed onto the previously coated Gas Diffusion Electrodes (GDEs), following the method described by Veh et al[57]. The resulting MEAs had a total membrane thickness of 5 mm. The catalyst loading on the cathode side was 0.2 mg Pt/cm^2, while for the anode, it was adjusted to 0.2 mg Pt/cm^2 and 0.1 mg Ru/cm^2. The catalyst loadings were verified using a mass balance.

2.2. Membrane conductivity

2.2.1. Resistance and conductivity

Resistance was measured in ohms (Ω) and represented the potential loss experienced when a charge moved through a conductor. Conductance, quantified in siemens (S), served as the inverse of resistance. To standardize resistance and eliminate the influence of geometric factors, resistivity (ρ) was employed, with measurements conducted in ohm-meters (Ωm). Conversely, conductivity (σ), being the reciprocal of resistivity, found application in materials designed to facilitate the conduction of charged species, while resistivity was suitable for insulating materials.[58] Metals demonstrated proficiency in electron conduction, whereas electrolytes displayed exceptional ionic conductivity.[58]

2.2.2. Ions and conductivity

Each type (i) of anions in the anions exchange membrane carrying charge $z_i F$ of per mole, where z_i is the charge number of that ion (e.g. -1 for OH^-) and F is the Faraday constant ($F = 9.648\ C/mol$). The electrostatic force experienced by an ion is directly proportional to the charge of the object and the strength of the electric field, and therefore can be calculated using Equation 2-1, where F_{dr} represents the electrostatic force drives the anions to migrate under the applied electric field, z_i represents the charge number of the ion (i), F represents the Faraday's constant which is the electric charge per mole of elementary charge, and E represents the electric field strength.[59]

Equation 2-1 $$F_{dr} = z_i \times F \times E$$

The rate of an ion (i) moves through a membrane can quantified using molar flux ($J, \text{unit:} \frac{mol}{cm^2 \times s}$), which measures the number of moles of ions flows through the membrane per unit are and per unit time.[59] For a membrane with concentration ($c_i, \text{unit} \frac{mol}{cm^3}$) of ion (i) moves at a velocity of ($v_i, \text{unit} \frac{cm}{s}$), the molar flux can be calculated using Equation 2-2.

Equation 2-2 $$J_i = c_i \times v_i$$

The migration velocity of the ion (i) in a membrane (v_i) is proportional to the inverse of the drag coefficient ($\frac{1}{\theta}$) and the electric driving force (F_{dr}) as shown in Equation 2-3.[59]

Equation 2-3 $$v_i = \frac{1}{\theta} \times F_{dr}$$

Combining Equation 2-1 and Equation 2-3, the mobility (μ_i) of the ion (i) defined as the migration velocity at unit field strength ($1 \frac{V}{m}$) and can be calculated as shown in Equation 2-4.[59]

Equation 2-4 $$\mu_i = \frac{v_i}{E} = \frac{1}{\theta} \times z_i \times F$$

The current density (j_i) caused by the flow of ion (i) can be calculated from its molar flux (J_i) as shown in Equation 2-5.[59]

Equation 2-5 $$j_i = J_i \times z_i \times F = z_i \times F \times c_i \times \mu_i \times E$$

The resistance (R) of a material is defined as the ratio of voltage (V) and current (I) as shown in Equation 2-6.[59]

Equation 2-6 $$R = \frac{V}{I}$$

The resistance per unit area is defined as resistivity (ρ) of the material, and therefore can be calculated using Equation 2-7.[59]

Equation 2-7 $$\rho = \frac{E}{j}$$

The conductivity (σ) of a material is defined as the reciprocal of its resistivity as shown in Equation 2-8.[59]

Equation 2-8 $$\sigma = \frac{1}{\rho}$$

Therefore, the conductivity of the anion exchange membrane can be measured by current-voltage measurement as shown in Equation 2-9.[59]

Equation 2-9 $$\sigma_{AEM} = \sum \sigma_i = \sum \frac{j_i}{E} = \sum \frac{J_i \times z_i \times F}{E} = \sum \frac{c_i \times v_i \times z_i \times F}{E} = \sum c_i \times \mu_i \times z_i \times F$$

2.2.3. Experimental procedure

The anion conductivity was obtained from the resistivity measurement of the anion exchange membrane either using alternating current (AC) technique or direct current (DC) technique in either through-plane ($\perp$) and in plane ($\parallel$) directions.[60] The conductivity of an anion exchange membrane (σ_{AEM}) was calculated using Equation 2-10, where d is the distance between the electrodes, A is the cross-sectional area through which current passes, R is the membrane resistance in Ω measured using various electrochemical techniques as mentioned in page 28.[60] The membrane conductivity can be obtained in both the through-plane ($\perp$) and in plane ($\parallel$) directions as shown in Figure 2-6.[60]

Equation 2-10 $$\sigma_{AEM} = \frac{d}{R \times A}$$

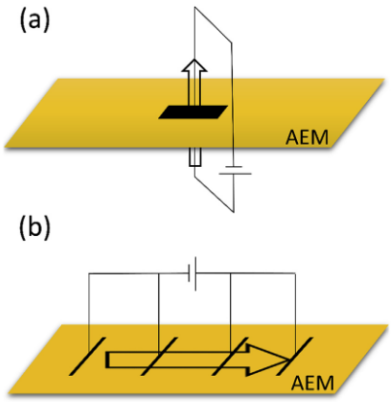

Figure 2-6. Schematic representation of (a) through-plane (TP) and (b) in-plane (IP) directions of an anion exchange membrane (AEM). Adapted from ref[60]

There are three configuration of conductivity cells used in this study to measure the ex-situ conductivity of a membrane as shown in Figure 2-7, Figure 2-8 and Figure 2-9.

The in-plane conductivity cell shown in Figure 2-7 required a membrane size of 5 x 15 mm and were connected to Solartron 1260 impedance analyzer. The impedence measurements were performed by applying a 10 mV sinusoidal AC potential over a frequency range of 10 MHz – 100 Hz. This cell utilized a two-probe cell configuration, where the current-generating electrodes also serve as the voltage-measuring probes. The frequency range was selected because previously reported that the membrane ionic resistance can be resolved from interfacial impedance only when the frequency is ≥ 100 Hz.[61]

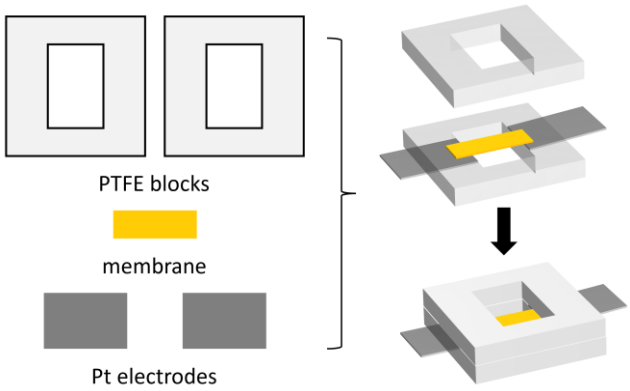

Figure 2-7. Schematic representation of the 2 electrodes setup for in-plane conductivity measurement using electrochemical impedance spectroscopy.

The in-plane conductivity cell shown in Figure 2-8 required a membrane size of 10 x 30 mm and was connected to Solartron Analytical 1287 electrochemical interface. The conductivity measurements were performed by applying a $\pm$ 100 mV DC potential scan at 10 mV/s scan rate. This cell utilized a four-probe cell configuration, where the two outer platinum gauze serves as the current collecting electrodes and the two inner platinum wires serves as the voltage sensing electrodes. During the resistance measurement, the potentiostat was set to apply the desired voltage between the two inner electrodes, and the resulting current was measured using the two outer electrodes. The distance between the two inner electrodes was fixed at 4.25 mm, which was used for the conductivity calculation.

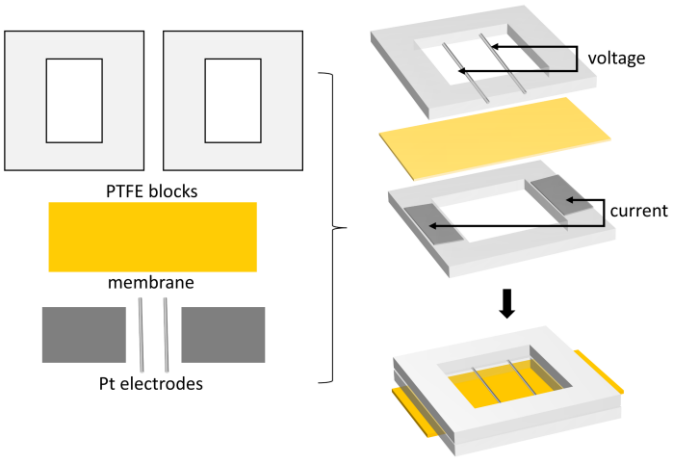

Figure 2-8. Schematic representation of the 4 electrodes setup for in-plane conductivity measurement using potentiodynamic technique.

The through-plane conductivity cell shown in Figure 2-9 required a membrane size of 10 x 30 mm and two 5 x 18 mm carbon paper as the gas diffusion electrodes. 1~2 drops of conductive carbon paint (SPI Supplies, colloidal graphite) were applied to the electrode using a disposable pipette. A precut piece of carbon paper was placed on top of the electrode before the carbon paint dried off. Once the carbon paint has dried and the carbon paper gas diffusion electrode has adhered to the Pt electrode, the cell was inverted to apply the gas diffusion electrode on the other side of the Pt electrode. The coarse macro-porous side of the carbon paper was placed against the rectangular Pt electrode so that the smooth Pt-coated side of the carbon paper contacted the membrane. After each measurement, the membrane and carbon papers were removed from the cell, and the remaining carbon paint on the rectangular Pt electrodes were cleaned thoroughly with lint-free tissues and methanol. Electrodes were insured to fully dried before next measurement.

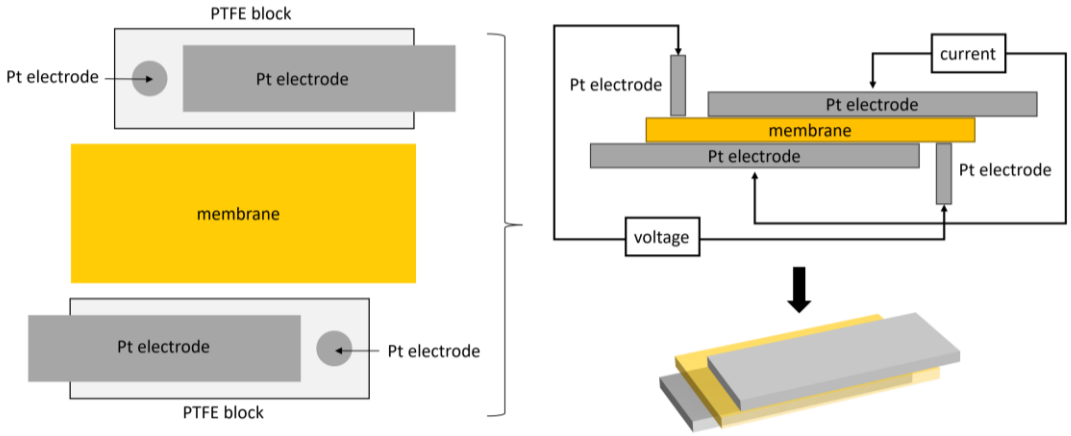

Figure 2-9. Schematic representation of the 4 electrodes setup for through-plane conductivity measurement using electrochemical impedance spectroscopy.

2.3. Electrochemical characterization techniques

In an electrochemical experiment, voltage (V), current (i), and time (t) are the three fundamental variables. The investigation of electrochemical behavior involves keeping certain variables constant while observing how other variables change with variations in the controlled variables.[62]

2.3.1. Potentiostatic technique

The voltage of a system is controlled, and the resulting current response is measured. The potentiostatic technique used in this study was steady-state technique, where the control voltage remained constant over time.

2.3.2. Galvanostatic technique

The current of a system is controlled, and the resulting voltage response is measured. The galvanostatic technique used in this study was also steady-state technique, where the control voltage remained constant over time.

2.3.3. Potentiodynamic and cyclic voltammetry techniques

Potentiodynamic and cyclic voltammetry technique is a time-variant (dynamic) technique, where the voltage applied to a system is swept linearly with time back and forth across a voltage window of interest. The resulting current response is measured as a function of time but is plotted as a function of the cyclic voltage sweep.

2.3.4. Electrochemical Impedance spectroscopy (EIS) technique

Impedance, in contrast to resistance which could be determined through static electrochemical measurements, deals with time- or frequency-dependent phenomena. The impedance, denoted as Z, was expressed as the ratio between a time-dependent voltage (V) and a time-dependent current (A).[16] Impedance measurements were typically conducted by applying a small sinusoidal voltage perturbation and monitoring the resulting current response of the system.[16] The current response could exhibit a phase shift (ϕ) compared to the voltage perturbation. Figure 2-10 presented a graphical representation illustrating the relationship between a sinusoidal voltage perturbation and a phase-shifted current response.[16] As illustrated in Figure 2-10, by sampling a sufficiently small portion of a cell's i-V curve, the amplitude of this signal was typically small enough to restrict the analysis to a pseudolinear segment of the cell's i-V curve.[16]

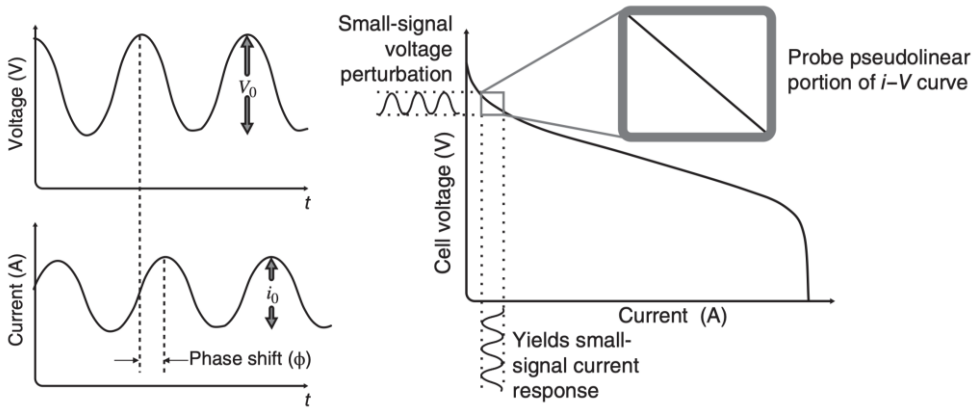

Figure 2-10. Illustration of sinusoidal voltage perturbation and resulting current response, showcasing phase shift and pseudolinear analysis region. The current response exhibits the same period as the voltage perturbation but may be subject to a phase shift, represented by ϕ. Adapted from ref[16]

The impedance is defined as the ratio of the voltage to the current at a given frequency and is expressed as a complex quantity consisting of a real part (Equation 2-12), an imaginary part (Equation 2-13), where Z_0 is the impedance magnitude, and ϕ is the phase shift (Equation 2-14) as shown in Equation 2-11.[16]

Equation 2-11 $$\mathrm{Z} = |\mathrm{Z_0}| \times \cos\phi + \mathrm{j} \times |\mathrm{Z_0}| \times \sin\phi$$

Equation 2-12 $$\mathrm{Z_{real}} = |\mathrm{Z_0}| \times \cos\phi$$

Equation 2-13 $$\mathrm{Z_{imag}} = |\mathrm{Z_0}| \times \sin\phi$$

Equation 2-14 $$\phi = \tan^{-1}\left(\frac{\mathrm{Z_{real}}}{\mathrm{Z_{imag}}}\right)$$

The impedance data were graphically represented by plotting the real and imaginary components of impedance ($\mathrm{Z_{real}}$ on the x-axis and $-\mathrm{Z_{imag}}$ on the y-axis). These graphical depictions of impedance data were known as Nyquist plots.[16]

Nyquist plot for ohmic resistance

In the case of a simple resistor, the ohmic conduction process is represented by an equivalent circuit consisting of only a resistor. In this scenario, the imaginary component of resistance is zero, ϕ is zero, and the impedance remains constant regardless of frequency, as illustrated in Figure 2-11.[16]

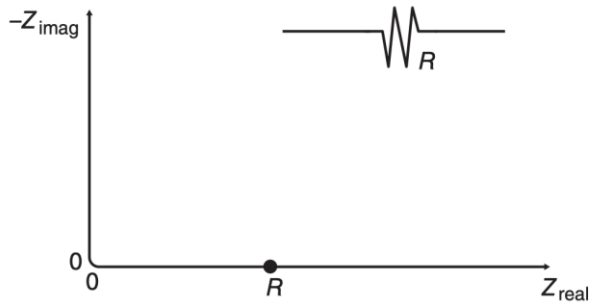

Figure 2-11. Nyquist plot of a resistor. The impedance of a resistor is a single point of value R on the real impedance axis (x-axis) and is independent of frequency. Adapted from ref[16]

Nyquist plot for electrochemical reaction interface

During an electrochemical reaction, a substantial charge separation occurs at the interface, resulting in the accumulation of electrons in the electrode and ions in the electrolyte. This charge separation causes the interface to exhibit capacitive behavior.[16] To model the impedance response of the reaction interface, it can be represented as a parallel combination of a resistor (R_f) and a capacitor (C_{dl}), as illustrated in Figure 2-12.[16] The Faradaic resistance (R_f) characterizes the electrochemical reaction kinetics, while the double-layer capacitance (C_{dl}) represents the capacitive nature of the interface. The high-frequency intercept of the semicircle represents zero impedance, indicating the absence of resistance at high frequencies. The low-frequency intercept corresponds to the faradaic resistance (R_f). The diameter of the semicircle, which is equivalent to R_f, provides valuable insights into the reaction kinetics of the electrochemical interface. A small semicircle indicates facile reaction kinetics, while a larger semicircle signifies sluggish reaction kinetics.[16]

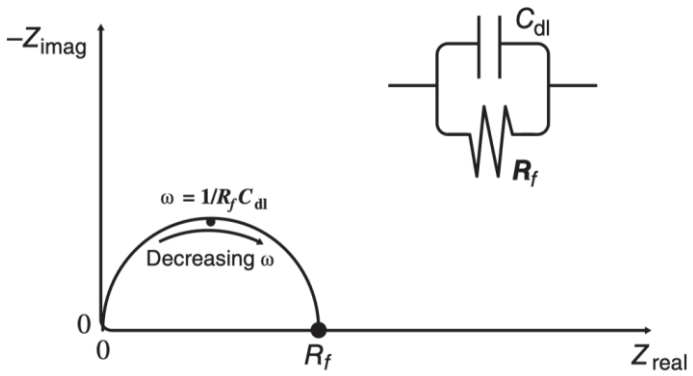

Figure 2-12. Nyquist plot of a parallel combination of a resistor and capacitor which demonstrated the impedance response of an electrochemical reaction interface. The capacitor (C_{dl}) describes the charge separation between ions and electrons across the interface. The resistor (R_f) describes the kinetic resistance of the electrochemical reaction process. Adapted from ref[16]

2.4. Nuclear Magnetic Resonance (NMR) Spectroscopy

Nuclear magnetic resonance (NMR) spectroscopy is an essential technique used in modern organic chemistry to determine the structure of molecules. It capitalizes on the nuclear spin properties exhibited by both hydrogen (^{1}H) and carbon-13 (^{13}C) atomic nuclei. By placing these atomic nuclei, acting as small bar magnets, within a strong magnetic field, an NMR spectrometer aligns them accordingly. When a radiofrequency pulse is applied with an energy level corresponding to the specific chemical environment of the nuclei, they can absorb this energy. This absorption causes the nuclei to transition from a lower energy state, aligned with the magnetic field, to a higher energy state, aligned against the magnetic field. Subsequently, as the nuclei relax back to the lower energy state, they emit this absorbed energy, which can be detected by the NMR spectrometer.

2.4.1. Calculate the degree of methylation

The ^{1}H NMR spectra were adjusted for the baseline using the "Full Auto (Polynomial Fit)" feature available in MestReNova 6.0.4 software. To determine the extent of methylation, the integration area ranging from 4.300 to 3.780 ppm was set to 12.00 for the 1H NMR spectra of I^- form of HMT-PMBI in DMSO-d_6 solvent. This region corresponds to the N-methyl groups of the positively charged benzimidazolium groups.

Subsequently, the area between 3.780 and 3.500 ppm was integrated, yielding a value of "x", which represents the N-methyl peaks of the uncharged benzimidazole groups. The dm% (degree of methylation) was then calculated using Equation 2-15, as presented below:

Equation 2-15 $$\mathrm{dm\%} = 50\%\left(\frac{1}{1+\frac{x}{6}}\right) + 50\%$$

2.4.2. Calculated theoretical ion exchange capacity ($IEC_{theoretical}$)

Because the ionic conductivity of the electrolyte was determined by the amount of positively charged functional groups in the polymer backbone, the structural relationship between the conductive cationic functional groups and the non-conductive polymer backbone was determined.

The ion exchange capacity (IEC, mmol/g) measures the amount of charged groups in the membrane and can be calculated using the number of functional groups (molar equivalents, eq.) per unit mass of dry membrane (g).[63] The theoretical IEC (IEC_{th}) of the membrane in their X^- form can determined by NMR spectroscopic analysis using Equation 2-16, where the dm represents the degree of methylation, M_{dm} represents the mass of the HMT-PMBI of certain dm%. M_{dm} can be calculated using the mass of the 100% dm HMT-PMBI repeating unit (for OH^- counter-ion: M_{R100}=636.82 g/repeating unit) and the molecular weight of the 50% dm HMT-PMBI repeating unit (for OH^- counter-ion: M_{R500}= 572.74 g/repeating unit). As shown in the chemical structure (Figure 2-2), there are 2 counter ions (X^-) in one 100%dm repeating unit; therefore, the equivalent counter ions (X^-) can be calculated using the amount of the 100%dm repeating unit in the membrane which is 2(dm-0.5).

Equation 2-16 $$\mathrm{IEC_{th}}\left(\frac{\mathrm{mmol}}{\mathrm{g}}\right) = \frac{\mathrm{eq.n_{X^-}}}{\mathrm{M_{dm}}} = \frac{\frac{1000\ \mathrm{mmol}}{1\ \mathrm{mol}} \times \frac{2[2(\mathrm{dm}-0.5)]\mathrm{eq.\ X^-}}{1\ \mathrm{repeating\ unit}}}{\mathrm{M_{R100}}[2(\mathrm{dm}-0.50)]+\mathrm{M_{R50}}[1-2(\mathrm{dm}-0.50)]}$$

2.4.3. Experimental ion exchange capacity ($IEC_{experimental}$)

The IEC determined by NMR analysis is only theoretical. It depends on the dissociation constant of the functional groups, the apparent ion exchange capacity, which is the number of functional groups in the polymer structure accessible to ion exchange and may not be the total amount determined by NMR. Therefore, the

experimental ion exchange capacity (IEC_{ex}) was measured experimentally by evaluating the amount of exchanged Cl^- ions using titrimetric analysis described in literature[63–66]. Prior to IEC analysis, membrane samples were converted to Cl^- form by immersing in 1 M KCl solutions twice for 24 hours and washing several times with DI water for 48 hours. To ensure complete exchange of Cl^- to NO_3^- ions, membrane samples were immersed twice in 15 g of 1 M KNO_3 solution for 24 hours. The Cl^- concentration of the combined 2 exchanged solutions were determined using a Cl^- ion-selective electrode (Cl^- ISE 6.0502.120, Metrohm AG®). The membranes were converted back into Cl^- form by soaking twice in 1 M KCl for 24 hours, washing multiple times with DI water for 48 hours and dried under vacuum at 80°C for 24 hours. The dry weight of the membrane in its Cl^- form (m_{dry}) was measured after cooling to room temperature under vacuum. The IEC_{exp} was calculated using the Cl- concentration ([Cl^-] in ppm), the mass of the exchange solution ($m_{solution}$) and molar mass of chloride ion (M_{Cl}) using Equation 2-17.

Equation 2-17 $$\mathrm{IEC_{ex}}\left(\frac{\mathrm{mmol}}{\mathrm{g}}\right) = \frac{[\mathrm{Cl^-}] \times \mathrm{m_{solution}}}{1000 \times \mathrm{M_{cl}} \times \mathrm{m_{dry}}}$$

2.5. Water sorption properties

The water content of the membranes was studied by measuring the mass and dimensional changes of their fully hydrated and dry states. Small pieces (2 x 3 cm) samples were cut for the water content measurements. The hydrated state was achieved by immersing the membranes in ultra-pure water for at least 24 hours. The thickness (t_{wet}), hydrated area (A_{wet}) and hydrated mass (m_{wet}) were measured on the fully hydrated membranes after removing any surface-bound water with Kimwipe®. To achieve the fully dried state, membrane samples were then sandwiched between filter papers and dried under vacuum oven at 80°C for at least 16 hours. The dry thickness (t_{dry}), dry area (A_{dry}) and dry mass (m_{dry}) were measured on the oven dried membranes.

2.5.1. Water uptake and volumetric swelling

The water uptake (WU, %) was calculated using the mass change between the fully hydrated and dry states using Equation 2-18. The volumetric swelling in three dimensions (Sx,y,z, %) and volumetric swelling (VS, %) were calculated using the dimensional changes of the fully hydrated and dry states using Equation 2-19 and

Equation 2-20 where the $S_{(x,y,z)}$ represents the x,y-directions (length and width) and z-direction (thickness) of the membrane in either fully hydrated $_{(wet)}$ or dry $_{(dry)}$ states.

Equation 2-18 $$WU(\%) = \frac{m_{wet} - m_{dry}}{m_{dry}} \times 100\%$$

Equation 2-19 $$S_{x,y,z}(\%) = \frac{S_{(x,y,z)wet} - S_{(x,y,z)dry}}{S_{(x,y,z)dry}} \times 100\%$$

Equation 2-20 $$VS(\%) = \frac{t_{wet} \times A_{wet} - t_{dry} \times A_{dry}}{t_{dry} \times A_{dry}} \times 100\%$$

2.5.2. Hydration number

The hydration number (λ), which represents the number of water molecules per ion-exchange site (mol H_2O/mol N^+) was determined using water uptake (WU), apparent ion exchange capacity (IEC_{exp}) and molar mass of water (M_{H2O}) via.

Equation 2-21 $$\lambda = \frac{WU}{M_{H2O} \times IEC_{ex}} \times 1000$$

2.5.3. Anion concentration

The anion concentration ($[X^-]$) was calculated using the apparent ion exchange capacity (IEC_{ex}), the dry mass of the membrane (m_{dry}), the hydrated thickness (t_{wet}) and area (A_{wet}) using Equation 2-22.

Equation 2-22 $$[X^-] = \frac{IEC_{ex,X^-} \times m_{dry}}{t_{wet} \times A_{wet}}$$

2.6. Optical analysis of the anion exchange membrane containing pH indicators

The UV-vis absorption spectroscopy was conducted using a Shimadzu UV-3600 Plus spectrophotometer in the range of 200 nm to 800 nm. The scan speed varied between 100 and 400 nm/min. The bandwidth of the light source in the UV-vis region was chosen to be 5 nm. The baseline correction procedure was executed prior to each measurement.

Because the color of an indicator may be different when the polarity of the solvent changed (solvatochromism effect), the UV-vis absorbance spectra of the acid

fuchsin cocast HMT-PMBI membrane should be compared to the spectra of acid fuchsin indicator to confirm the positively charged functional groups does not alter the polarity inside the membrane. The UV-vis absorbance spectra of the acid fuchsin indicator was measured in buffer solutions of KOH, K_2CO_3, $KHCO_3$ ranging from pH 10 to 14. The UV-vis absorbance spectra of the HMT-PMBI was measured in its Cl^-, HCO_3^-, CO_3^{2-} and OH^- forms, which were achieved by soaking the membranes in 2 M KCl, $KHCO_3$, K_2CO_3 or KOH solutions twice for 24 hours. The fully hydrated UV-vis absorbance spectra of the membranes were measured while immersing the membrane in the corresponding aqueous salt solutions against the baseline correction with DI water. The partially hydrated UV-vis absorbance spectra of the membranes were measured immediately after removing any solution on the surface of the membrane with a lint-free wipes against the baseline correction of ambient air.

2.7. Anion exchange membrane in different counter-ion form

AEMs cannot be fully exchanged to the desired single ion form after only 1 x immersion in a solution containing the target ion, even if a concentrated solution containing excess target ion is used: the use of only 1 x immersion will leave a small amount of the original ions in the material (ion exchange involves partition equilibria). AEMs must be ion exchanged by immersion in multiple (at least 3) consecutive fresh replacements of the solution containing an excess of the desired ion. Traces of the original (or other contaminants) ions can have implications regarding the properties being measured.[67]

Chapter 3. Study of polyimidazolium-based AEM with and without the incorporation of polyolefin reinforcement substrate

This chapter have been reproduced with permission from the peer-reviewed article published as Wei, Q.; Cao, X.; Veh, P.; Konovalova, A.; Mardle, P.; Overton, P.; Cassegrain, S.; Vierrath, S.; Breitwieser, M.; Holdcroft, S. On the Stability of Anion Exchange Membrane Fuel Cells Incorporating Polyimidazolium Ionene (Aemion+®) Membranes and Ionomers. *Sustainable Energy Fuels* **2022**, *6* (15), 3551–3564. https://doi.org/10.1039/D2SE00690A from Sustainable Energy Fuels.

This work was financially supported by the Natural Science and Engineering Research Council of Canada (NSERC) (Grant CRDPJ529968), and, through this grant, support of Ionomr Innovations Inc.; the German-Canadian project FlexCoat/NRCIRAP 2 + 2 Programme (Grant 01DM19008A); and the VectorStiung within the project AlkaCell.

Individual contributions were: Q. W., X. C., and P. V. all contributed equally to this work. Conceptualization: Q. W., A. K., P. M., S. H. Methodology: Q. W., X. C., P. V., A. K., P. M., P. O., S. C. Writing: Q. W., P. V., A. K., P. M., M. B., S. H. Supervision: S. H., M. B. Funding acquisition: S. H., S. V.

3.1. Introduction

The increased focus on clean electrochemical energy conversion technologies has seen a notable rise globally, primarily driven by the negative environmental impacts linked to the burning of fossil fuels. Hydrogen fuel cells have gained prominence in the sustainable and clean energy industries as they effectively convert the chemical energy from hydrogen and oxygen reactions into electrical energy.[68] The commercialization of proton exchange membrane fuel cells (PEMFCs) has been made possible through dedicated efforts to achieve efficient energy conversion at high current densities. However, the utilization of platinum-based catalysts in PEMFCs comes with significant capital and manufacturing costs. Additionally, the use of perfluorosulfonic acid (PFSA)-based membranes in PEMFCs may pose potential environmental drawbacks. Recent advancements have unveiled anion exchange membrane fuel cells (AEMFCs) as a promising substitute, as they demonstrate comparable power performance to PEMFCs.[9,69,70]

The early development of anion exchange membranes (AEMs) primarily focused on improving the conductivity of the solid polymer electrolyte to achieve a similar values as Nafion (>100 mS cm^{-1}).[71,72] This was achieved by increasing the ion exchange capacity (IEC) of the polymer electrolytes, which also led to increased dimensional swelling and reduced mechanical integrity.[73–75] Recently researchers have shifted their focus towards understanding how polymer design impacts the separation between hydrophilic and hydrophobic phases, aiming to enhance conductivity by increasing the percolation of hydrophilic domains.[76] To mitigate swelling, cross-linking of the solid polymer electrolyte has been explored, but this approach often compromises conductivity, water uptake, mechanical properties (such as elongation at break), and solubility.[76,77] One solution to enhance mechanical stability is to incorporate a reinforcement material, and thus allowing for thinner membranes. For example, Kienitz et al. fabricated an stable ultra-thin (5 μm) GORE-SELECT® proton exchange membrane by utilizing expanded poly-tetrafluoroethylene (ePTFE) as the reinforcement material.[78,79] Similar PTFE materials have been adopted as the supporting materials to prepare reinforced anion exchange membranes,[80,81] the use of fluorinated reinforcement materials reintroduces environmental concerns associated with perfluoroalkyl substances. To address this issue, researchers have investigated the use

of inert reinforcement materials. For instance, Park et al. employed cross-linked tetramethylammonium poly(sulfone) with an inert poly(phenylsulfone) to increase the ion exchange capacity (IEC) of the anion exchange membrane (AEM) while mitigating dimensional swelling.[82]

Over the past few years, the Holdcroft lab has made a concerted effort to design a series of C_2-sterically protected polybenzimidazoliums and polyimidazoliums materials for anion exchange membranes.[47,83,84] These compounds have been proven to exhibit high conductivity while exceptional resistant to harsh chemical environments and possess outstanding durability, both chemically and mechanically.[53,55] With the success of the commercialized Aemion® membrane based on the hexamethy-p-terphenyl poly(benzimidazolium) (HMT-PMBI) structure, the more stable polyimidazolium-based has recently been commercialized as Aemion^{+}® by Ionomr Innovations Inc. In this study, we are comparing the conductivity, water uptake and swelling properties of the Aemion^{+}® with and without incorporation of polyolefin reinforcement substrate.

3.2. Materials and methods

3.2.1. Materials

Commercialized AEMs used in this study include: monolithic AEMION® membranes (AF1-HNN8-25 and AF1-HNN8-50), monolithic AEMION^{+}® (AH2-INN8-10 and AH2-INN8-50) and polyolefin reinforced AEMION^{+}® (AF2-HLE8-10 and AF2-HLE8-40) as listed in Table 3-1. The commercialized AEMs are used as received from Ionomr Innovations Inc.

Table 3-1. Physical properties of commercialized anion exchange membrane used in this study

AEM	Base polymer	Reinforcement	Thickness (μm)	IEC (mmol g^{-1})
AF1-HNN8-25	Poly(benzimidazolium)	Monolithic	25[a]	2.30±0.02[b]
AF1-HNN8-50	Poly(benzimidazolium)	Monolithic	50 [a]	2.30±0.02[b]
AF2-INN8-10	Poly(imidazolium)	Monolithic	10 [a]	2.94±0.07[c]
AF2-INN8-50	Poly(imidazolium)	Monolithic	50 [a]	2.94±0.07[c]
AF2-HLE8-10	Poly(imidazolium)	Polyolefin substrate	10 [a]	1.90±0.22 [c]
AF2-HLE8-40	Poly(imidazolium)	Polyolefin substrate	40 [a]	1.90±0.22 [c]

[a] Thickness of dry AEM sample obtained from manufacturer specification: Ionomr Innovations Inc., Canada
[b] Previously reported by Gangrade et al.[85]
[c] Previously reported by Wei et al.[49]

Potassium chloride (KCl, 99.0%), potassium nitrate (KNO_3, 99.0%), potassium hydroxide (KOH, 87.5%) from Fisher Scientific were used as received to prepare salt solutions. Dimethyl sulfoxide (DMSO-d_6, 99.9%) from Cambridge Isotope Laboratories Inc. was used to prepare the NMR samples. All water (H_2O) used in this study was deionized to 18 MΩ with a Milli-Q water purification system (SYNSVHFWW, Synergy® UV Water Purification System).

3.2.2. Methods

Membrane pre-treatment

In previous studies, it was observed that HMT-PMBI exhibited varying conductivity and water absorption properties depending on the type of anion present. In order to ensure consistency and avoid any discrepancies caused by different anion forms, all membranes were converted into the chloride (Cl^-) form prior to analysis. This was accomplished by immersing the commercially available membrane at least 6 times in a 3 M KCl solution for a duration of 12 hours each time. Subsequently, the membrane was washed multiple times with deionized (DI) water over a period of 3 days to remove excess salt solutions.

Ion-exchange capacity

Ion exchange capacity (IEC) is defined as the number of charge carriers per mass of dry polymer. The IEC of all commercial membranes were measured in their Cl^-

form using the ion exchange method.[77] The principle of IEC measurement was to exchange the samples from the Cl^- form to NO_3^- and measure the Cl^- concentration in the exchange solution using a Cl^--selective electrode. First, 20 mg of three samples from each type of commercialized membrane were soaked in 20 mL of 3 M NaCl solution for 3 days with at least 6 repeated refreshments of solutions to exchange to its Cl^- form, followed by 3 days of the same procedure with DI water to wash off excess salt solution. The membrane samples were dried in a vacuum oven at 80°C for at least 16 hours before measuring their dry mass. After cooling to room temperature, the membrane samples were carefully removed from the oven and quickly measured their mass in an analytical balance and recorded as m_{dry}. To determine the ion exchange capacity of each membrane sample, the Cl^- formed dry membranes were exchanged to NO_3^- form by immersing in 1 M KNO_3 solutions for 3 days. During this process, the Cl^- in the membrane sample migrates to the exchanged solution and is replaced by NO_3^- due to concentration gradient. The Cl^- concentration in the exchanged solution was measured using the Cl^- ion selective electrode (Metrohm USA Inc., USA) and recorded as $[\mathrm{Cl}^-]$. The ion exchange capacity was calculated using the Cl^- concentration ($[\mathrm{Cl}^-]$) and the mass ($\mathrm{m_{solution}}$) of the KNO_3 solution containing exchanged Cl^- ions, the molar mass of Cl^- ion ($\mathrm{M_{Cl^-}}$) and the mass of the dry membrane sample in its Cl^- form ($\mathrm{m_{dry}}$) as shown in Equation 3-1.

Equation 3-1 $$\mathrm{IEC}_{(\mathrm{Cl}^-)} = \frac{[\mathrm{Cl}^-] \times \mathrm{m_{solution}}}{\mathrm{M_{Cl^-}} \times \mathrm{m_{dry}}}$$

Water uptake

The commercialized membrane samples were exchanged to its Cl^- form prior to the water uptake measurement. The Cl^- formed membrane samples were soaked in deionized water for at least 24 hours to allow the membranes absorb water and reach a fully hydrated state. After removing the surface water with a paper towel, the wet mass ($\mathrm{m_{wet}}$) was determined on an analytical balance. This procedure was repeated at least three times to obtain a reliable value. The membrane samples were then dried at 80 °C for at least 12 hours under vacuum. After cooling the dried membrane samples to room temperature under vacuum, the dry mass ($\mathrm{m_{dry}}$) was obtained using an analytical balance. This process is repeated until a constant dry mass was reached meaning no more water residue was trapped in the sample. The water uptake (WU) was calculated

using the average value of the wet mass ($\mathrm{m_{wet}}$) and the average value of the dry mass ($\mathrm{m_{dry}}$) as shown in Equation 3-2.

Equation 3-2 $$\mathrm{WU_{(Cl^-)}} = \frac{\mathrm{m_{H_2O}\ (mass\ of\ water)}}{\mathrm{m_{dry}\ (mass\ of\ dry\ polymer)}} = \frac{\mathrm{m_{wet} - m_{dry}}}{\mathrm{m_{dry}}}$$

Dimensional Swelling

The wet dimensions of the membrane samples for each polymer were obtained by soaking in DI water for a minimum of 24 hours at room temperature (~ 22°C). The image of the wet membrane samples was scanned using a Canon Canoscan 8400F scanner at a resolution of 1600 dpi. The wet width ($width_{wet}$) and wet length ($length_{wet}$) of the membrane samples were obtained by analyzing the scanned image of the wet membrane samples using ImageJ.[86] The above procedure was repeated to obtain the dry width ($width_{dry}$) and dry length ($length_{dry}$) after drying the membrane samples at 80°C for at least 12 hours under vacuum. The wet and dry thickness ($thickness_{wet}$ and $tichkness_{dry}$ respectively) were measured by taking 5 discrete points on each membrane samples using a Mitutoyo Quickmike Series 293 micrometer. The area swelling and thickness swelling were calculated using Equation 3-3 and Equation 3-4.

Equation 3-3 $$\mathrm{S_{(area,Cl^-)}} = \frac{\mathrm{width_{wet} \times length_{wet} - width_{dry} \times length_{dry}}}{\mathrm{width_{dry} \times length_{dry}}}$$

Equation 3-4 $$\mathrm{S_{(x,Cl^-)}} = \frac{\mathrm{length_{wet} - length_{dry}}}{\mathrm{length_{dry}}}$$

Dynamic Vapour Sorption

Dynamic Vapour Sorption (DVS) measurements were made using a DVS Adventure humidity chamber and Ultrabalance (Surface Measurement Systems Ltd., UK). Samples were held at constant temperature (60°C, 70°C and 80°C) and the Relative Humidity (RH%) was decreased stepwise in the 60-0.0% RH range. The humidity was controlled by a source of DI water delivered under nitrogen gas flow at a volumetric flow rate of 200 standard cubic centimetres per minute (sccm). The hydration number (λ) is defined as the number of water molecules per ion pair, which is calculated as the ratio of moles of water (n_{H_2O}) per moles of ion pair ($n_{ion\ pair}$) as

shown in, where m_{dry} is the dry mass of membrane sample, IEC is ion exchange capacity, M_{H_2O} is the molar mass of water, and WU is the water uptake.

Equation 3-5 $$\lambda = \frac{n_{H_2O}}{n_{ion\ pair}} = \frac{WU}{IEC \times M_{H_2O}}$$

Ex-situ Conductivity

The ionic conductivity of the AEMs in their Cl^- form was measured in both the in-plane and through-plane directions using SI 1260 electrochemical impedance spectroscopy (Solartron Analytical Inc.). A 100 mV alternating potential was applied over a frequency range of 100-10 MHz.

The experimental setup for measuring the anion exchange membrane conductivity in in-plane direction is shown in Figure 3-1. The AEM samples are held between two Pt electrodes of known distance (approximately 0.5 cm) within a PTFE frame. The two Pt electrodes are adhered to the bottom PTFE block, and the top PTFE block is clamped to the bottom PTFE block. The in-plane conductivity was calculated using Equation 3-6, where l represents the distance between the two Pt electrodes (approximately 0.5 cm), w and t represents the width and thickness of the membrane respectively, and $R_{\parallel}$ represents the in-plane impedance of the membrane measured from electrochemical impedance spectroscopy.

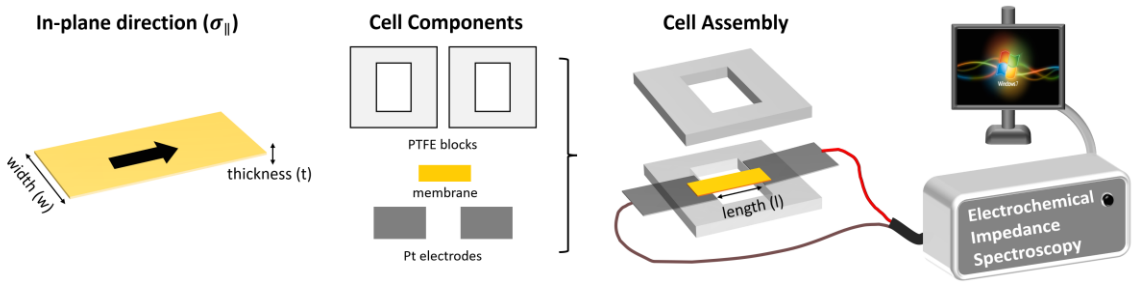

Figure 3-1. In-plane membrane conductivity measurement experimental setup.

Equation 3-6 $$\sigma_{\parallel} = \frac{l}{w \times t \times R_{\parallel}}$$

The experimental setup for membrane conductivity in through-plane direction is shown in Figure 3-2. The AEMs are sandwiched between two Pt electrodes which measure the current at a pressure > 300 psi. Two additional Pt electrodes on the PTFE frame measure the voltage across the membrane. The through-plane conductivity was

calculated using Equation 3-7, where t represents the thickness of the membrane, A represents the overlapping area of the two Pt electrodes measures the current (approximately 0.5 cm^2), and $R_{\perp}$ represents the through-plane impedance of the membrane measured from electrochemical impedance spectroscopy.

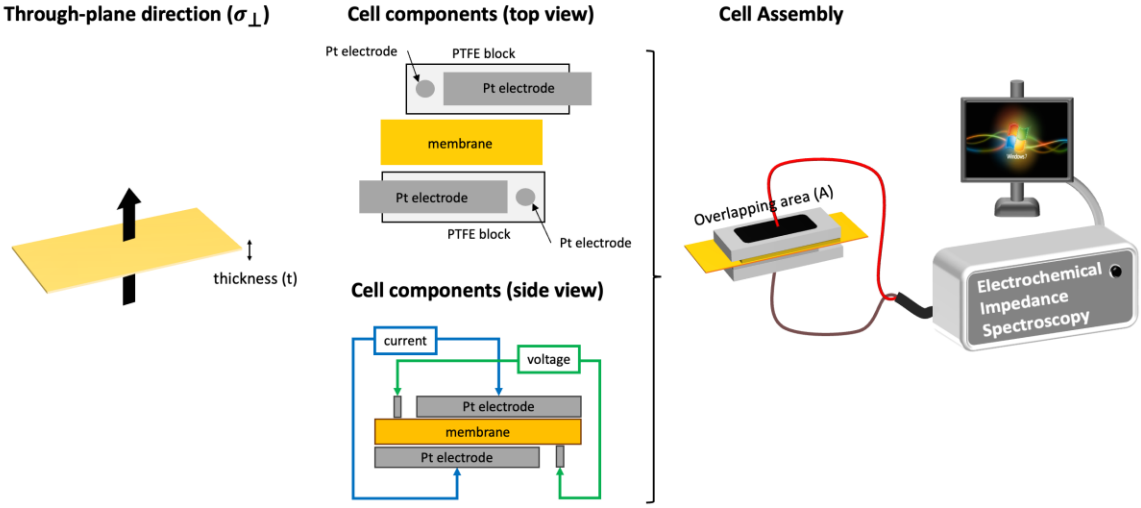

Figure 3-2. Through-plane membrane conductivity measurement experimental setup.

Equation 3-7 $$\sigma_{\perp} = \frac{t}{A \times R_{\perp}}$$

Through-plane measurements were conducted in a membrane testing system (MTS 740, Scribner Associates Inc.) whereas the in-plane measurements were conducted in an environmental chamber (SH-241, ESPEC North America Inc.), both of which used to control the temperature and relative humidity to representative values for in-situ anion exchange membrane fuel cell system. All measurements were taken upon AEM dehydration (e.g. high RH to low RH). Resistances were obtained by fitting the spectra to an equivalent circuit. From the resistances in Ω, membrane conductivity values were calculated using for in-plane direction and for through-plane direction, where l represents the length between the electrodes on the in-plane conductivity cell, A represents the overlapping area between two electrodes on the through-plane conductivity cell, and the w and t represents the width and thickness of the membrane sample.

3.3. Results and discussion

3.3.1. Optimizing parameters for through-plane conductivity measurement

Cell configuration and sample size

Typically, the measurement of through-plane conductivity was acquired in two ways: in-situ testing using a single cell or ex-situ testing using a bare membrane. In the case of in-situ single cell testing, the process involves consistently catalyzing the membrane, assembling the cell, and finally conducting the test within a single cell. However, the resistance obtained from this type of test includes many factors other than the membrane's contribution, such as the electronic resistance of: the flow field, the gas diffusion media, as well as contact resistance.[87] As a result, the approach of obtaining through-plane conductivity from a bare membrane was selected for this study.

Through-plane conductivity measurements are restricted to a two-electrode configuration because the difficulty of inserting two independent voltage sensing electrodes in a thin membrane. A true four-electrode configuration requires electrodes that are located in the membrane that do not influence the potential field.[88]

A schematic representation of the two conductivity cells is listed in Figure 3-3. Soboleva's cell uses PTFE (polytetrafluoroethylene) block and two 0.1 mm thick Pt sheets as the electrodes and sandwich the membrane in between. The two electrodes are directly on top of each other, which gives the effective area of 1 cm^2 (1 cm × 1 cm square). Membrane samples were cut into 1 cm^2, which is the same size as of the electrode overlapping area. Measurement was performed by placing the entire setup in deionized water for measuring the through-plane conductivity of a membrane in its fully hydrated state at room temperature (22°C). Similarly, Cooper's cell uses a PEEK (polyether ether ketone) substrate and two Pt source electrode (thickness of Pt sheet not reported) to construct the cell. However, carbon paint (SPI supplies, colloidal graphite) was used to adhere two Gas Diffusion Electrode (GDE) to the Pt source electrode. The GDE was installed that the macro-porous side of the GDE facing Pt source electrode and the smooth Pt-coated side facing membrane. In addition, the two electrodes are offset to each other, which gives the effective area of 0.5 cm^2. The GDE were cut into a 1.8 cm × 0.5 cm size, and membranes were cut into 3 cm × 1 cm size,

which is larger than the electrode overlapping area.[89] In Cooper's design, the purpose of the GDE is to facilitate water vapor entry and exit the membrane as the measurement was conducted at various hydration states (various RH%) in contrast to Soboleva's design where measurements were conducted in the fully hydrated state (immersed in water). Therefore, the membrane samples were cut to a size larger than the overlapping electrode to help the membrane equilibrate under various RH%, as the extra area of the membrane will be exposed to the humidified environment instead being clamped between electrodes. Measurement was performed at wide range of temperature (30°C to 180°C) and relative humidity (0% to 95%).

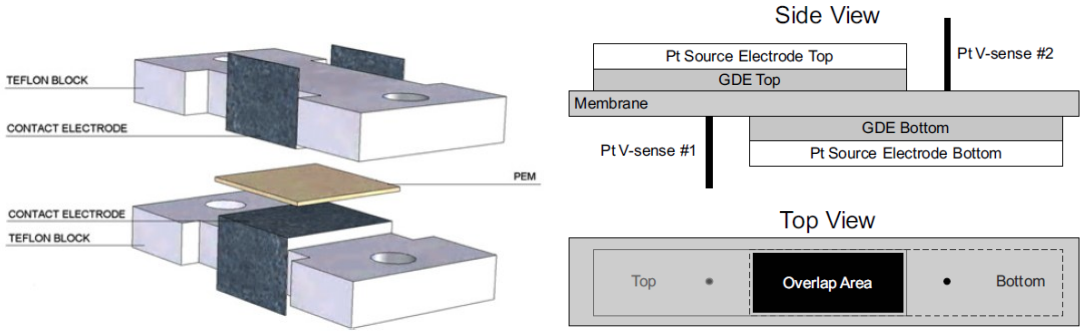

Figure 3-3. Through-plane conductivity cell: left: Soboleva's design, right: Cooper's design. Adapted from references[89,90]

Compression pressure

Soboleva et al[1] reported that increased clamping pressure helps eliminate the contact resistance and a compression of ≥ 1200 psi is desired for good contact. The compression pressure was estimated using Pressurex® film (pressure range 350 psi to 1400 psi, film type "low")[90]. However, Cooper[2] did not report any change in resistance or conductivity due to compression, and all measurements were performed at 310 ± 2.5 psi. The compression pressure was controlled using a calibrated force spring and displacement indicator dial as shown in Figure 3-4.

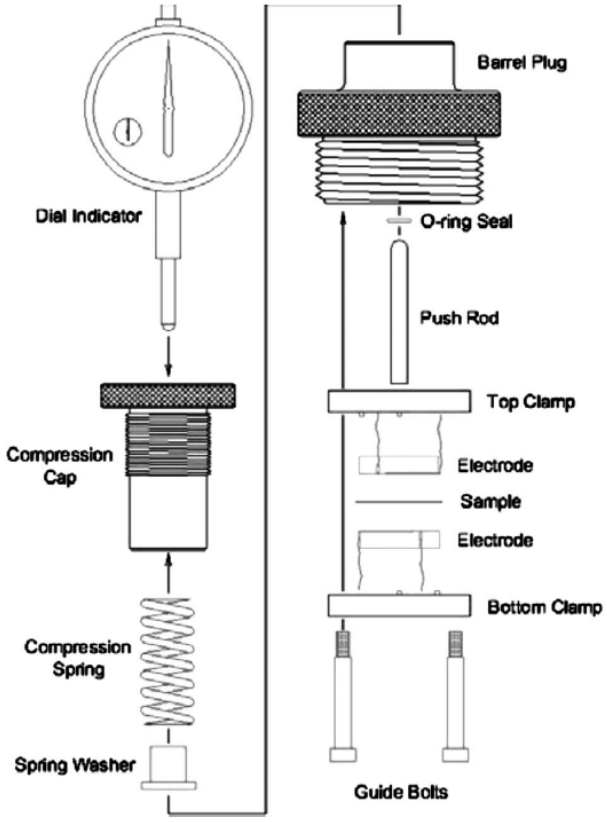

Figure 3-4. Compression control system of Cooper's cell. Adapted from ref[89]

The displacement dial indicates the travel of the movable electrode in inches, and the applying compression can be calculated using Equation 3-8, where the spring constant is 185 pound-force per inch and the compression is 0.2325 inch^2. Cooper mentioned that calculations indicate the change of the membrane thickness is negligible compared to the overall spring compression[89].

Equation 3-8 $$\text{Compression}(\text{psi} = \frac{\text{lbf}}{\text{inch}^2}) = \frac{\text{displacement (inch)} \times 185 \text{lbf/inch}}{0.2325 \text{ in}^2}$$

The clamping compression pressure adjusted using the dial indicator in Cooper's cell was checked with the Fujifilm® pressure paper (pressure range of 0.5MPa to 2.5MPa, film type "super low pressure (LLW)". The equivalent pressure range of the Fujifilm pressure® paper in psi is 72.5 psi to 362.6 psi. As shown in Figure 3-5, four compression loadings are compared: 0.100 inch (79.6 psi), 0.200 inch (159.1 psi), 0.300 inch (238.7psi) 0.400 inch (318.3psi) and the maximum 0.478 inch (374 psi). Based on the depth in color of the redness of the compression film, a pressure of at least 159 psi was required to maintain sufficient contact between the electrodes. Due to

limitation of the instrument, the maximum displacement of the dial is approximately 0.478 inch (corresponding to 374 psi), therefore the compression for Cooper's cell was set to its maximum.

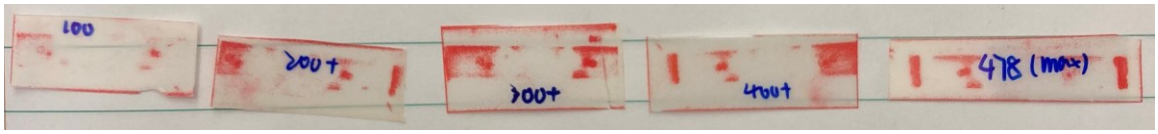

Figure 3-5. Validating the compression dial indicator with Fujifilm® pressure paper.

EIS parameters (AC amplitude and frequency range)

The AC amplitude of must be optimized such that it is small enough to satisfy the linearity assumption and large enough to separate the measured response from noise. In Soboleva's paper[90], the frequency response analyzer used is a 100 mV_{ac} amplitude and frequency range of 10^7 - 100 Hz. In contrast, Cooper[88] reported measuring the impedance at lower amplitude (0 $mV_{dc,}$ 10 mV_{ac}) and lower frequency range of (2×10^6 - 1 Hz). Due to the instrument limitation of the impedance analyzer used in the lab (Solartron Analytical 1260), the selected frequency must be within 32×10^6 - 1×10^{-5}Hz range.

As shown in Figure 3-6, the impedance spectrum obtained from 10Hz to 1Hz extends to quadrant IV which represented the inductive behavior. Therefore, the frequency range of 10^7-100 Hz were selected for further impedance measurements to isolate capacitive behaviour.

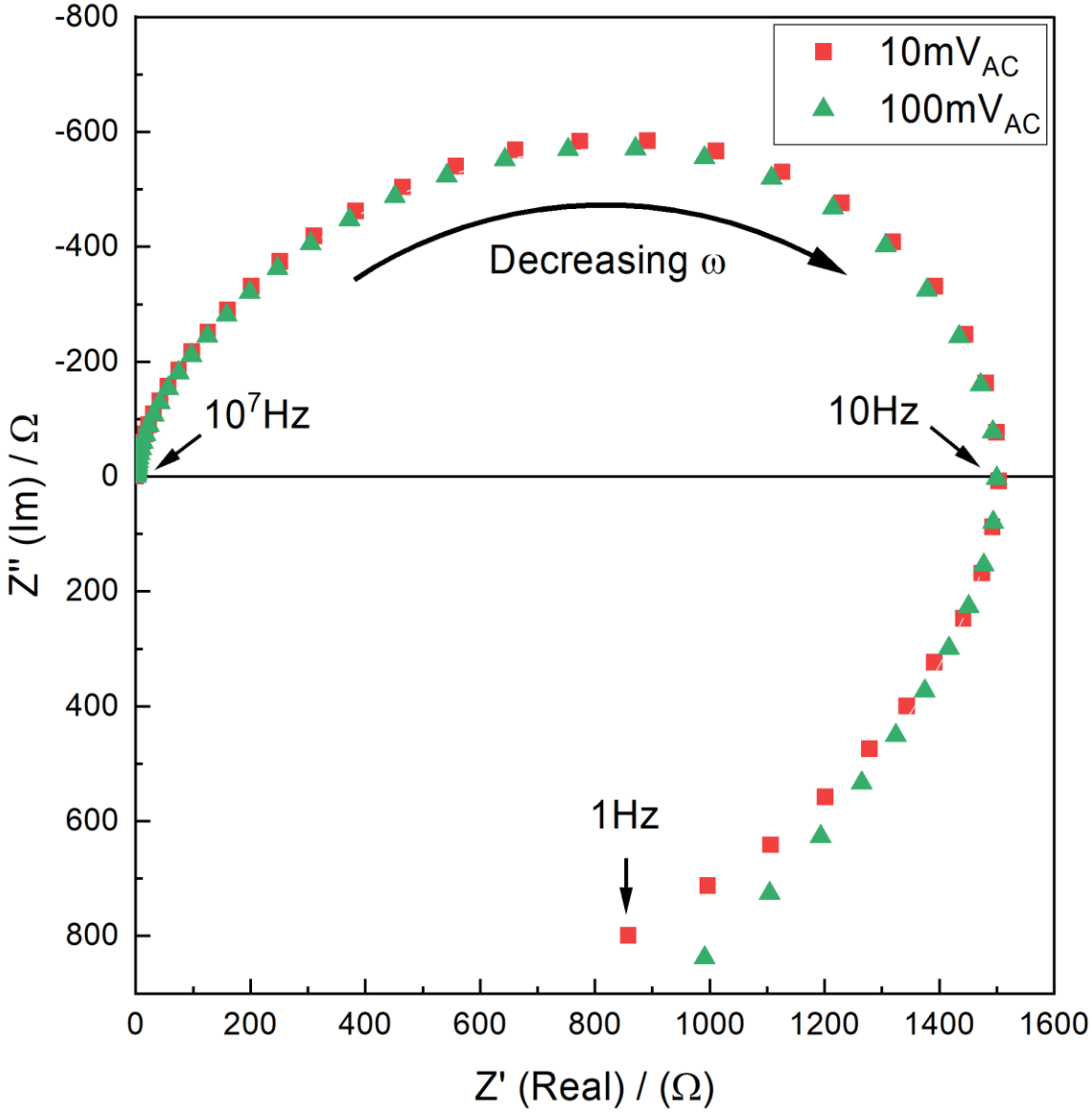

Figure 3-6. Impedance spectrum obtained on a through-plane conductivity cell (Cooper's design[88]) using a commercial membrane Nafion 115 with various AC amplitude (10mV$_{ac}$ and 100mV$_{ac}$) and frequency range (10^7-1Hz).

Because the membrane resistance was extracted from the high-frequency region of the impedance spectrum, the 100 mV$_{ac}$ amplitude was selected as it displays less noise as shown in the zoomed in high frequency impedance spectrum (Figure 3-7). The fitting was improved by 0.9% error for using 100 mV$_{ac}$ compared to using 10 mV$_{ac}$ as shown in Table 1-1. The conductivity of the commercialized Nafion 211 membrane at 30°C at 90% RH using 100 mV$_{ac}$ was found to be 41.8 mS/cm compared to 47.9 mS/cm using 10 mV$_{ac}$.

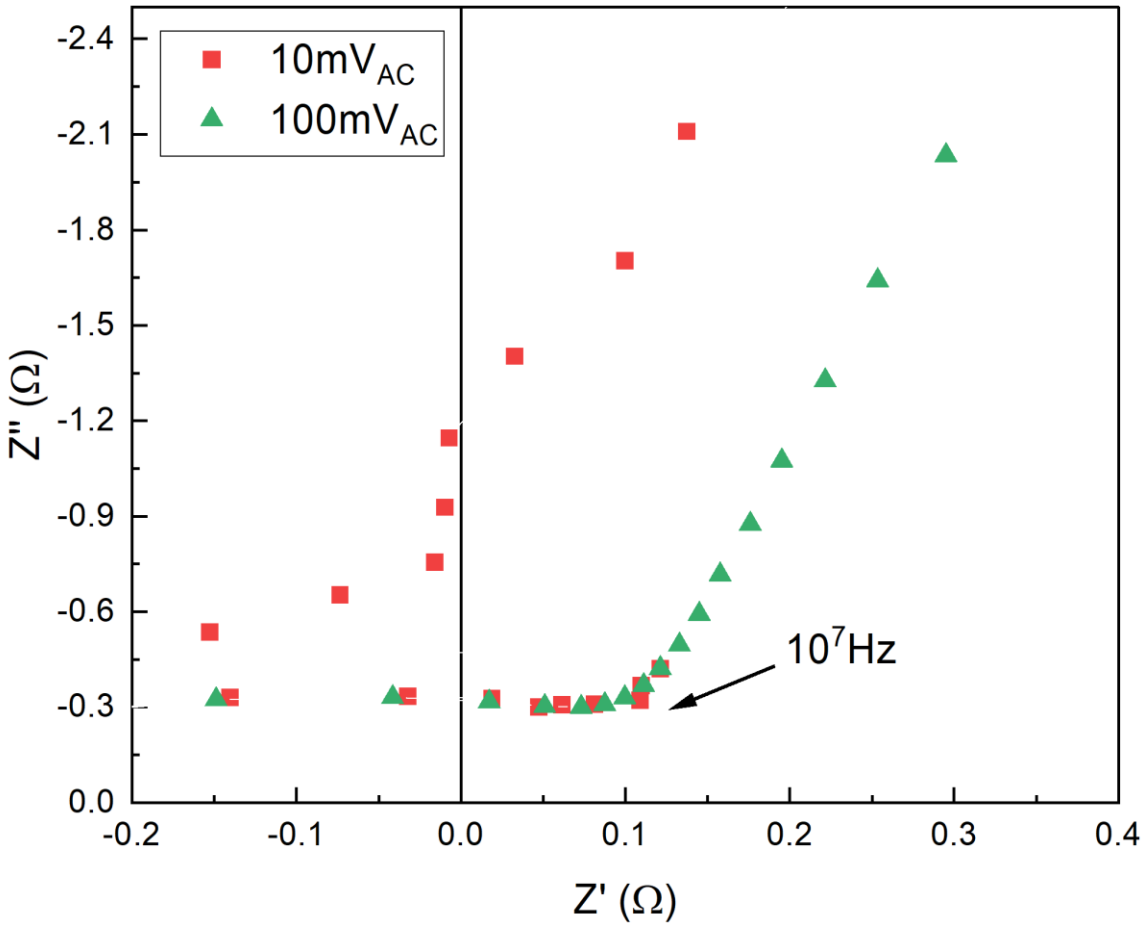

Figure 3-7. **High-frequency region of the impedance spectrum obtained on a through-plane conductivity cell (Cooper's design[88]) using a commercial membrane Nafion 115 with AC amplitudes: 10mV$_{ac}$ and 100mV$_{ac}$.**

Table 3-2. **Comparison of the through-plane conductivity obtained using two AC amplitudes (10 mV$_{ac}$ and 100 mV$_{ac}$) of Nafion 211 membrane at 30°C and 90%RH using Cooper's design for the conductivity cell.**

AC amplitude	Resistance (Ω)[a]	Fitting Error (%)	Through-plane conductivity (mS/cm)
10 mV$_{ac}$	0.11	3.97	47.93
100 mV$_{ac}$	0.12	3.02	41.85

a Resistance obtained from high-frequency intercept using equivalent circuit modeling method

Equivalent circuit model

The resistance of the membrane was extracted from impedance spectrum via equivalent circuit modeling. A through-plane conductivity cell contains a membrane electrode assembly by sandwiching a film of a proton conducting polymer between two

Pt electrodes. An idealized circuit for such a system can be represented by the equivalent electric circuit shown in Figure 3-8. Each membrane/electrode interface was modeled by a parallel combination of a capacitance (C_{int_1} and C_{int_2}) and a resistance (R_{int_1} and R_{int_2}), which represents the capacitance of the double layers and the resistance of each interface. The impedance of the polymer electrolyte film was modeled by a capacitance (C_m) in parallel with a resistance (R_m).

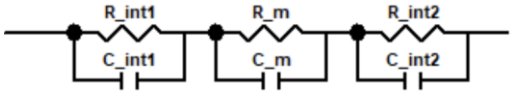

Figure 3-8. Idealized equivalent circuits for the polymer membrane sandwiched between two electrodes: R_{int_1} C_{int_1} R_{int_2} and C_{int_2} represents the paralleled combination of the resistance and capacitance at the two membrane-electrode interfaces, R_m and C_m represents the resistance and capacitance of the polymer membrane.

Due to the irregularities of a real solid electrode surface, Soboleva recommended to use a constant phase element (CPE) to model the interfacial impedance at both electrode/membrane interfaces[90]. Because the faradaic charge cannot cross the interface, the membrane/electrode interface is merely capacitive, the equivalent circuit model used to analyze the impedance spectrum has been simplified as shown in Figure 3-9, where R_m was extracted as the resistance of the polymer film.

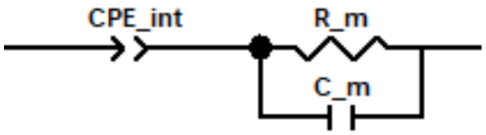

Figure 3-9. Simplified equivalent circuits for the polymer membrane sandwiched between two electrodes: CPE_{int} represents the combined interfacial impedance at both membrane-electrode interfaces, R_m and C_m represents the resistance and capacitance of the polymer membrane. Reproduced from ref[90].

The equivalent circuit (Figure 3-9) for the simplified equivalent circuit proposed in ref [90] was simulated using Zview software with parameters taken from Soboleva's work[90]: R_m of 0.97 Ω which models the membrane resistance (typical range of 0.1-10 Ω), CPE-T of 3.79 x 10^{-6} F which models the double layer capacitance at the membrane/electrode interface, CPE-P of 0.933 Ω which models the roughness of the membrane-electrode contact interface (close to 1 for a very smooth surface) and C_m of

7.00 x 10^{-9} F which represents the capacitance of the membrane. Due to instrument limitation of the impedance analyzer, the observed impedance spectrum based on the equivalent circuit proposed in ref [90] should be only the inclined spur of the semicircle.

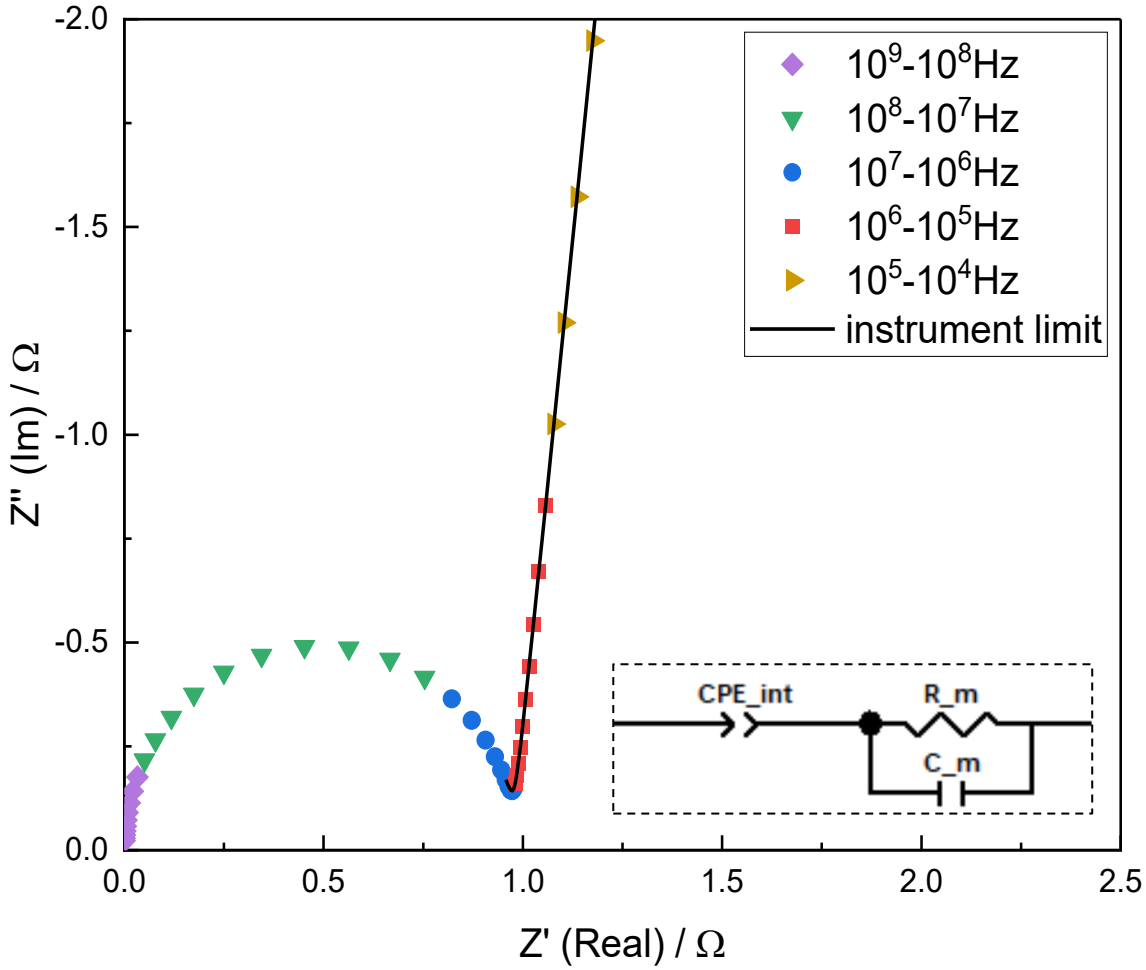

Figure 3-10. Simulated Nyquist plots using the equivalent circuit shown in Figure 3-9 at frequency range from 10^9 Hz to 10^4 Hz. Parameters were taken from Soboleva's work: CPE_{int}-T = 3.79 x 10^{-6} F, CPE_{int}-P = 0.933 Ω, R_m = 0.97 Ω and C_m = 7.00 x 10^{-9} F.

In Cooper's paper, a different equivalent circuit (Voigt circuit) was used to fit the experimental impedance spectra as shown in Figure 3-11, which consists of a resistor in series with two parallel resistor-constant phase elements (R||CPE).[88] The impedance of the polymer membrane was extracted from R_m. The membrane-electrode interfaces were modeled by the parallel resistor-constant phase element as R_{int_1}. R_{int_2} CPE_{int_1}. And CPE_{int_2}.

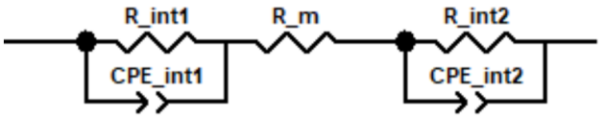

Figure 3-11. Voigt equivalent circuits for the polymer membrane sandwiched between two electrodes: CPE_{int_1} CPE_{int_2} R_{int_1} and R_{int_2} represents the combined interfacial impedance at both membrane-electrode interfaces, R_m and C_m represents the resistance and capacitance of the polymer membrane. Reproduced from ref[88].

The equivalent circuit (Figure 3-12) for the voigt equivalent circuit proposed in ref [88] was simulated using Zview software with parameters: R_m of 0.97 Ω which models the membrane resistance (typical range of 0.1 - 10 Ω), R_{int1} of 1.907 Ω, CPE_{int1}-T of 1.89 × 10^{-5} F, CPE_{int1}-P of 0.834 Ω for one of the membrane-electrode interface, R_{int2} of 0.822 Ω, CPE_{int2}-T of 5.28 x 10^{-5}, CPE_{int2}-P of 0.94 Ω for the other membrane-electrode interface. The highest frequency of the impedance analyzer used in this study is 32 × 10^6 Hz, therefore the observed impedance spectrum should be a semicircle.

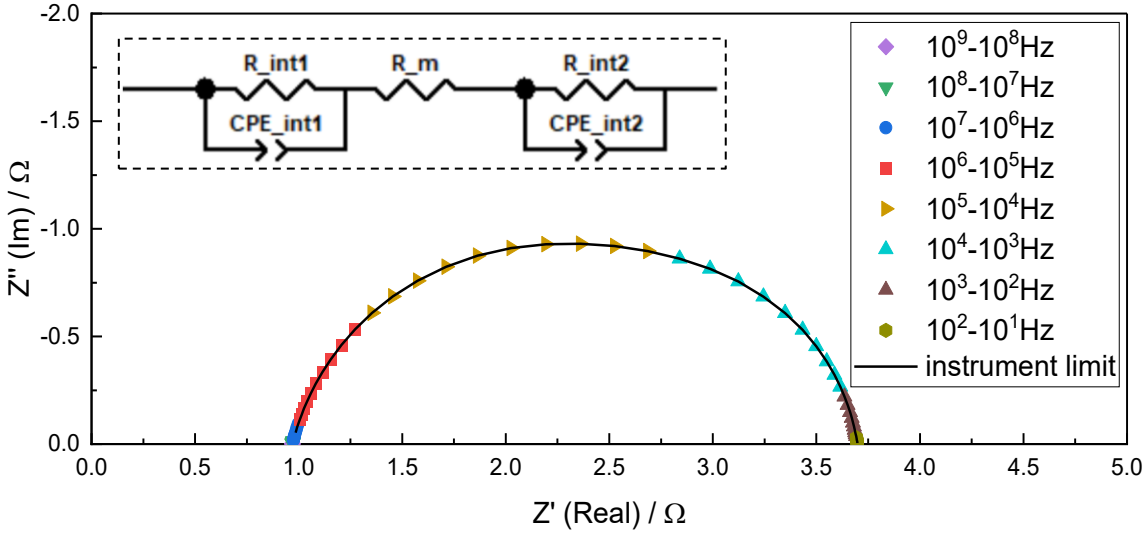

Figure 3-12. Simulated Nyquist plots using the equivalent circuit shown in Figure 3-11 at frequency range from 10^9Hz to 10^1 Hz. Parameters: CPE_{int1}-T = 1.89 x 10^{-5} F, CPE_{int1}-P = 0.834 Ω, R_{int1} = 1.907 Ω, CPE_{int2}-T = 5.28x10^{-5} F, CPE_{int1}-P = 0.94 Ω R_{int2} = 0.822 Ω and R_m = 0.97 Ω.

Cooper mentioned the option of adding an inductor (L) in series can be used to account for high frequency artifacts.[88] As shown in Figure 3-13, the membrane resistance extracted from the high frequency resistance by adding an inductor in series decreased from 1.288 Ω to 1.255 Ω, and fitting error improved from 1.28% to1.03%,

yields conductivity increased from 19.72 ± 0.25 mS/cm to 20.24 ± 0.20 mS/cm. However, significant simulating time was observed to fitting the impedance spectra using the equivalent circuit (inductor added) as the fitting program needs to fit 6 variables instead of 5 variables. The extended fitting time could be reduced by pre-fitting the impedance spectra using the equivalent circuit (no inductor added) and using the fitted parameter to fit the impedance spectra.

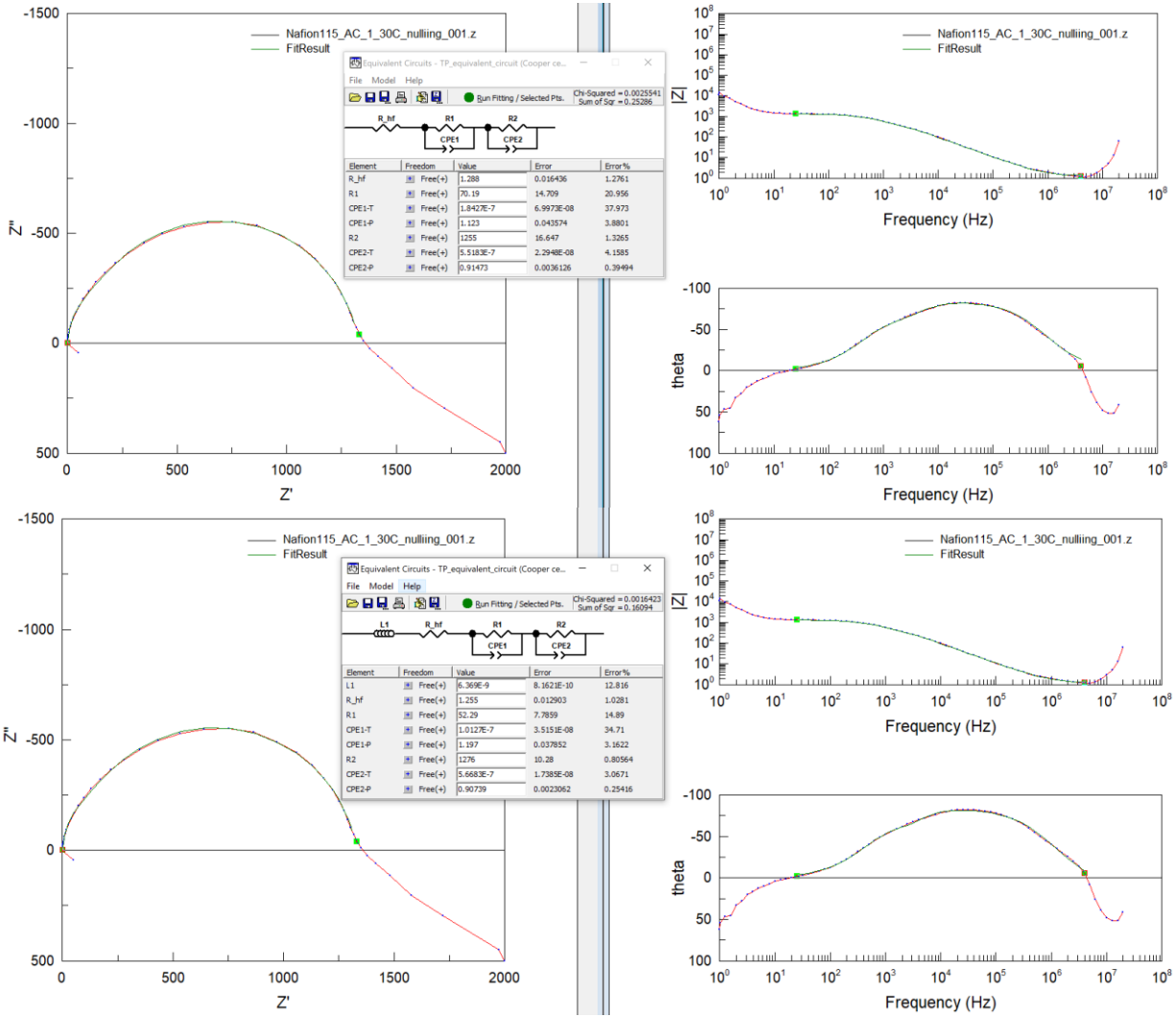

Figure 3-13. Fitting experimental impedance spectra with Voigt model equivalent circuit with and without adding an inductance to account for high frequency artifacts.

3.3.2. Validate protocol with literature using a commercialized proton exchange membrane

In order to validate the protocol of extracting the membrane resistance from a through-plane conductivity measurement, the experimental values were compared with literature using a well-commercialized membrane of various thickness. Nafion 115 is a thick proton exchange membrane, which possesses a thickness of 127 μm and proton conductivity of 54 mS/cm at 22°C in its fully hydrated state. Nafion 211 is a thin proton exchange membrane, which possess a thickness of 25 μm and proton conductivity of 180 mS/cm at 80°C in its fully hydrated state.[90] The Nafion membrane samples were pretreated prior to conductivity measurement. To remove residual organic molecules, the membrane samples were boiling in deionized water for 1 hour, followed by an additional 1 hour boiling in dilute H_2O_2. Subsequently, the membranes were boiled in 1 M H_2SO_4 solution for 1 hour to remove any possible inorganic contaminant. Finally, the membrane samples were thoroughly rinsed in deionized water until achieving a neutral pH.

The through plane proton conductivity of the commercial Nafion 115 (thickness 127 μm) membrane in its fully hydrated state at room temperature was reported to be 54 mS/cm in the literature using Soboleva's cell. [90] The through-plane proton conductivity of the same membrane was measured at room temperature for various relative humidities (20% RH – 95% RH). The relative humidity was controlled by a constant flow of a mixture of dry and wet 99.999% purity nitrogen gas at a flow rate of 500 standard cubic centimetres per minute (sccm). The maximum relative humidity was limited to 95% RH due to the build in environmental chamber (MTS 740 membrane test station, Scribner). This work chose to study the membrane conductivity change at various relative humidity values is because the polymer electrolyte was exposed to water vapour instead of liquid water for electrochemical applications (e.g., anion exchange membrane fuel cell). At room temperature, the through-plane conductivity was found to be 53 mS/cm for Nafion 115 at 95% RH, which matches within 2% of the literature value of 54 mS/cm for the same membrane at fully hydrated state. The through plane conductivity was conducted by desorption (70% RH to 20% RH) followed by adsorption (20% to 95%RH). As shown in Figure 3-14, the through plane conductivity of Nafion 115 during desorption was observed to be higher than absorption at the same RH%. The observed hysteresis in proton conductivity aligns with the water

uptake hysteresis reported in literature, which is likely due to the water conducting domains of Nafion aligning parallel to the surface and preventing water loss during dehydration.[91,92]

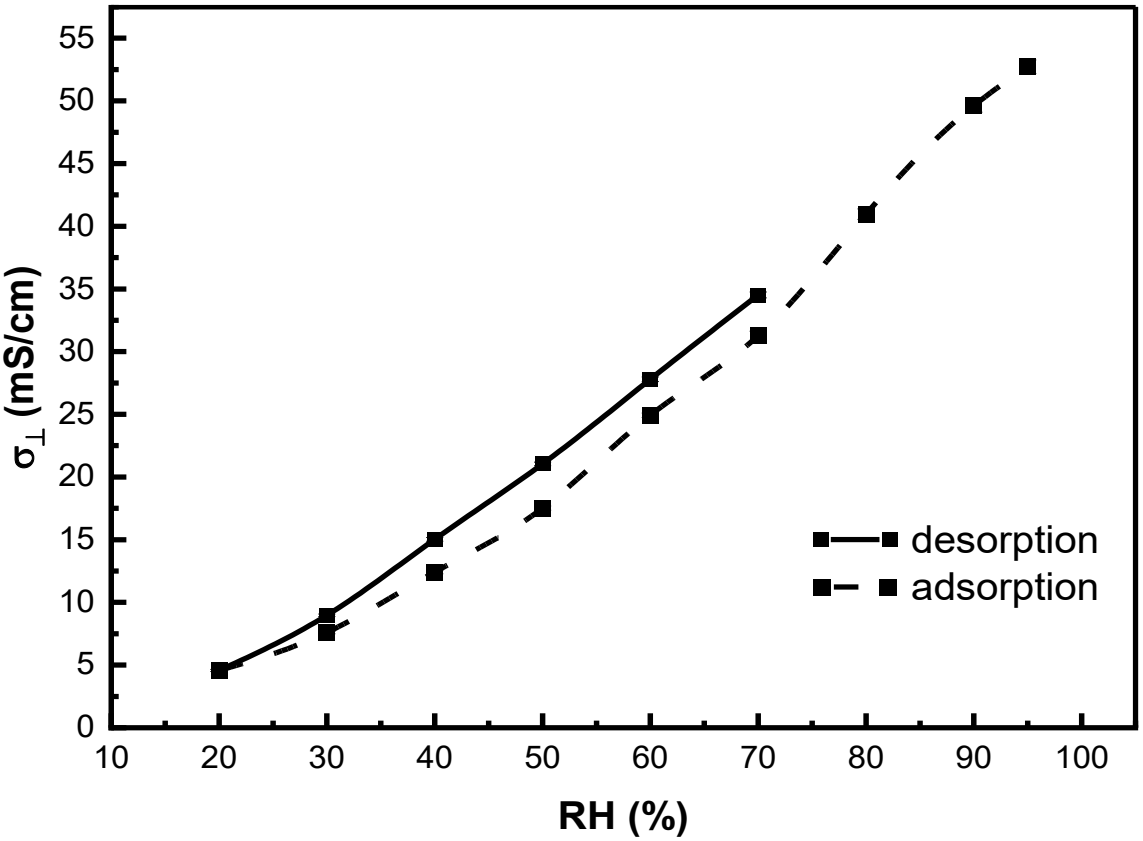

Figure 3-14. Through-plane proton (H^+) conductivity of Nafion 115 (127 µm thick) at room temperature (25°C) at equilibrium with water vapour during desorption (70% RH to 20%RH) and absorption (20% RH to 95% RH) obtained using Cooper's conductivity cell[88].

In addition, a thinner commercial membrane (Nafion 211, thickness 25.4 µm) was measured at elevated temperature (80°C) to validate the protocol for ultra-thin membranes and various temperatures applications. The through-plane proton conductivity of Nafion 211 increases along with relative humidity (%RH) as shown in Figure 3-15. Similar trends were observed for Nafion 115 membrane as shown in Figure 3-14. The increased conductivity at higher hydration level can be explained based on the proton transport mechanism in the PFSA membranes: protons were transported via vehicular mechanism, where ions moves via the movement of water through the free volume in a polymer membrane, and via the Grotthuss (proton hopping) mechanism, where ions move via breaking and forming O-H bonds in the

water molecules.[91] The hysteresis between desorption and adsorption for the thinner membrane Nafion 211 (25.4 μm) at elevated temperature (80°C) were larger at high hydration levels (above 60% RH) and smaller at low hydration levels (below 40% RH).

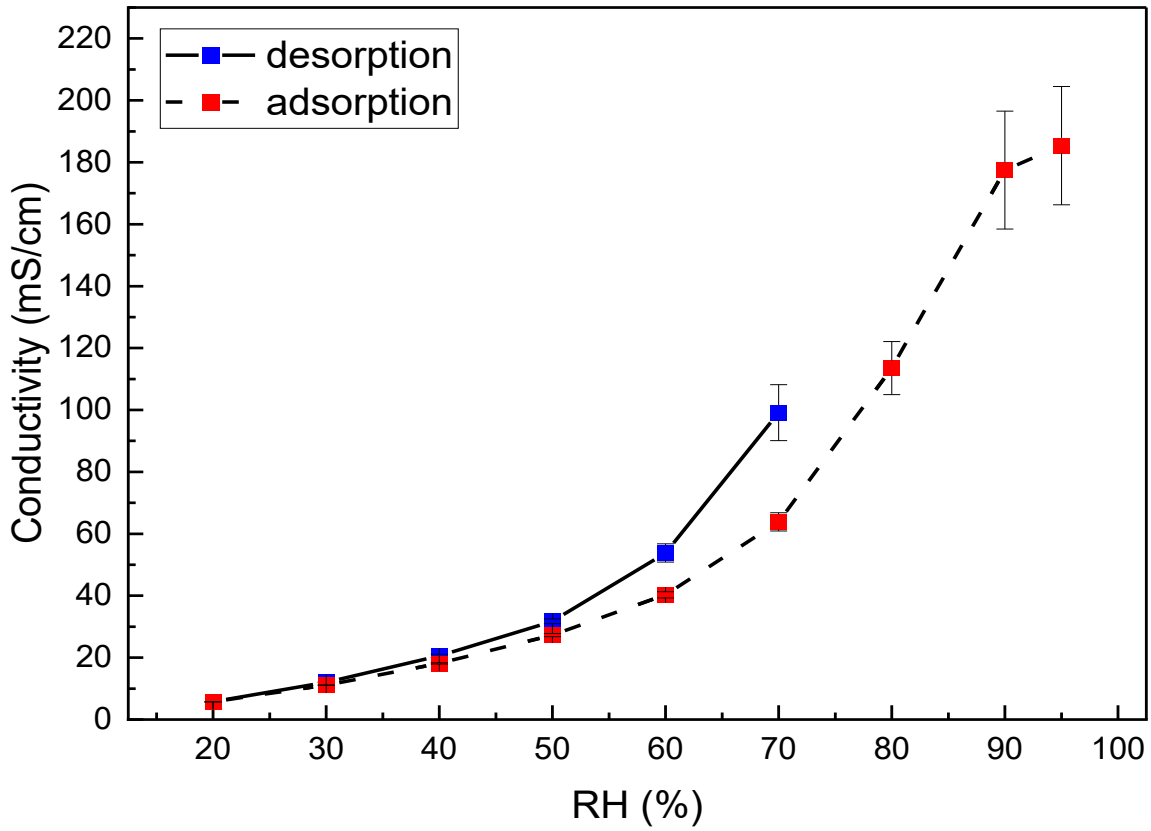

Figure 3-15. Through-plane proton (H^+) conductivity of Nafion 211 (25.4 μm thick) at elevated temperature (80°C) at equilibrium with water vapour during desorption (70% RH to 20%RH) and absorption (20% RH to 95% RH) obtained using Cooper's conductivity cell[88].

3.3.3. Optimizing parameters for in-plane conductivity measurement

Xie et al compared the two-probe and four-probe cell configuration to obtain the membrane resistance using an impedance analyzer, where the four-probe cell were strongly influenced by the probe geometry than the two-probe cells.[90] Therefore, Xie et al[90] concluded that the two-probe cell provide simple and well-defined impedance speactra from which the membrane conductivity can be extracted reproducibly.

In this study, the impedance spectra were obtained using the two-robe cell published by Xie et al[90] with 100 mV_{ac} for frequency range of 10^6 Hz to 100 Hz. The resistance of the membrane was extracted using the equivalent circuit shown Figure

3-16, where R_0 was extracted as the resistance for the membrane, the parallel R_1 and CPE_1 indicated the contact resistance and capacitance at the membrane-electrode interface.

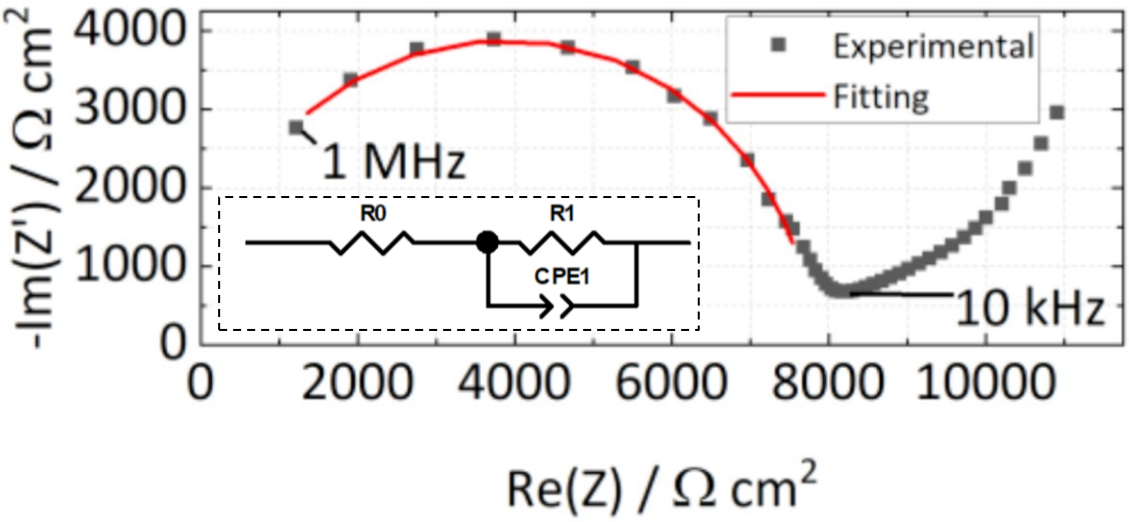

Figure 3-16. Example of fitting the EIS spectra for ex-situ conductivity measurements. Fitting was conducted with the equivalent circuit where R_1 is taken as the resistance for ionic conduction within the membrane. Reproduced from ref[49]

3.3.4. Selected impedance spectra for in-plane and through-plane conductivity measurement using the optimized protocols

Sample impedance spectra for in-plane conductivity measurement

The impedance spectra for in-plane conductivity measurement shows a semi-circle with a tail around 45 degrees as shown in Figure 3-17. The diameter of the semi-circle decreased with increasing RH% at a selected temperature, which indicated an increased conductivity at higher hydration level.

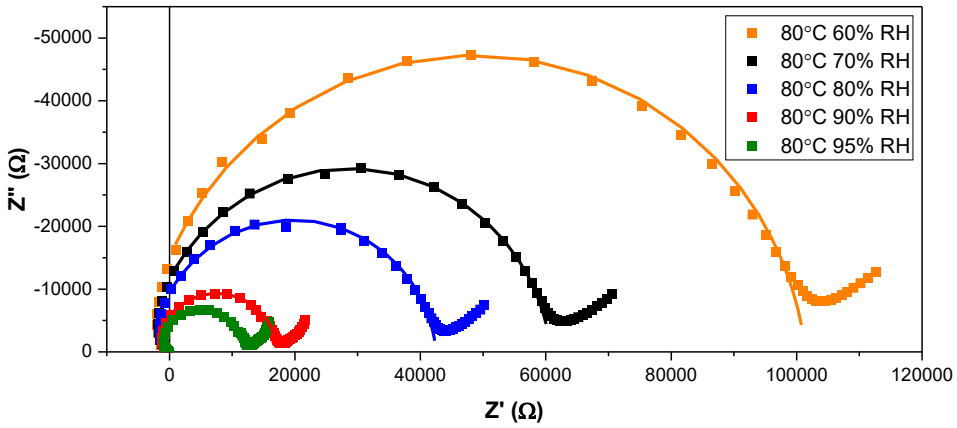

Figure 3-17. Experimental (■) and fitted (—) impedance spectra for AF2-HLE8-40X membrane in its Cl^- form and in plane direction at 80°C 60%-95%RH. Data obtained using customized PTFE-Pt conductivity cell.

Sample impedance spectra for through-plane conductivity measurement

The impedance spectra for in-plane conductivity measurement shows a semi-circle extended to quadrant IV as shown in Figure 3-18. The resistance of the membrane was extrapolated from the high-frequency intercept as shown in the zoomed impedance spectra Figure 3-19. The high frequency intercept decreased with increasing RH% at a selected temperature, which indicated an increased conductivity at higher hydration level.

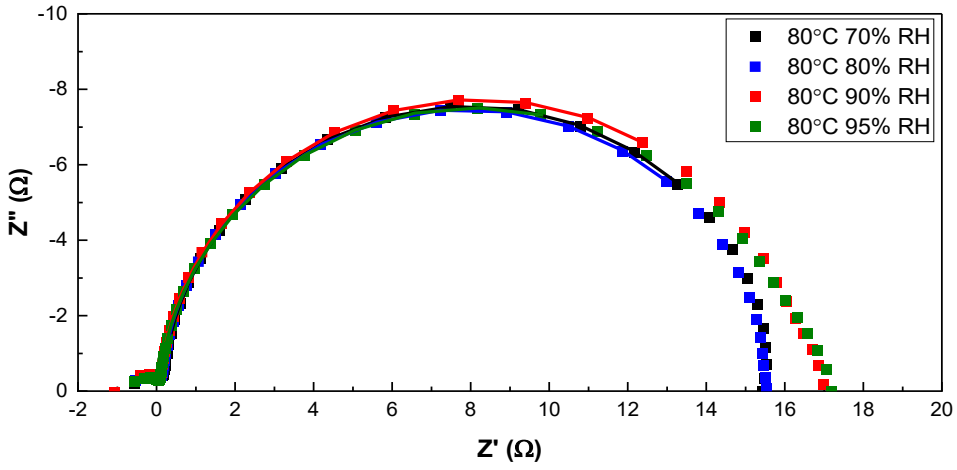

Figure 3-18. Experimental (■) and fitted (—) impedance spectra for AF2-HLE8-10X membrane in its Cl^- form and through plane direction at 80°C 70%-95%RH. Data obtained using MTS 740 system, clamp pressure 461 in.

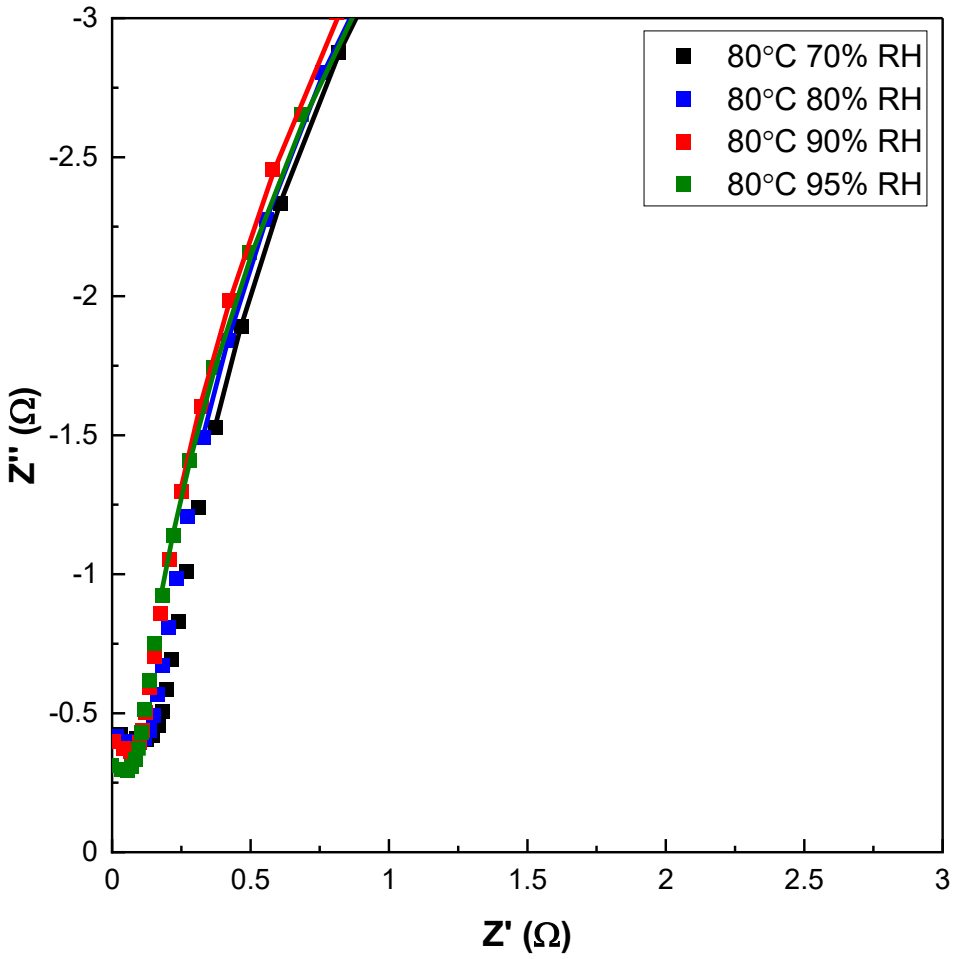

Figure 3-19. Experimental (■) and fitted (—) impedance spectra for AF2-HLE8-10X membrane in its Cl^- form and through plane direction at 80°C 70%-95%RH. Data obtained using MTS 740 system, clamp pressure 461 in. Zoom in to show high frequency intercept.

3.3.5. Analysis of the Cl^- conductivity for imidazolium based commercial anion exchange membrane of various thickness with or without reinforcement composite for a wide range of temperature and relative humidity

The anion exchange membrane in an anion exchange membrane fuel cell facilitates OH^- ion transport between electrodes, be resistant to electron transport through the electrolyte and be a barrier to fuel gases (H_2 and O_2) crossover. However, measuring the conductivity of an AEM in its OH^- is problematic because the OH^- rapidly neutralized into HCO_3^- and CO_3^{2-} by reaction of atmospheric CO_2 (present ~ 400 ppt in air).[93] Therefore, hydroxide conductivity measurement requires rigorous control of experimental conditions. In this study, the Cl^- ion conductivity was compared because it

is stable in air, enabling comparison of the conductivity values between different membrane materials without exclusion of atmospheric CO_2.

First, the Cl^- conductivity of two monolithic membranes was compared to illustrate the effect of IEC on the membrane conductivity. The 50 µm monolithic Aemion+® (AF2-HNN8-50, Figure 3-21) shows approximately 10% higher conductivity than the 50 µm monolithic Aemion® (AF1-HNN8-50, Figure 3-20) for both through-plane direction and in-direction at all tested conditions (60°C, 70°C and 80°C and 60 % - 95 %RH). The increased conductivity of the Aemion+® is likely due to the higher IEC of the Poly(imidazolium) base polymer. A higher IEC represents the polymer possess more positively charged functional groups, thus the polymer can hold more anions due to charge balance as shown in the schematic representation in Figure 3-20.

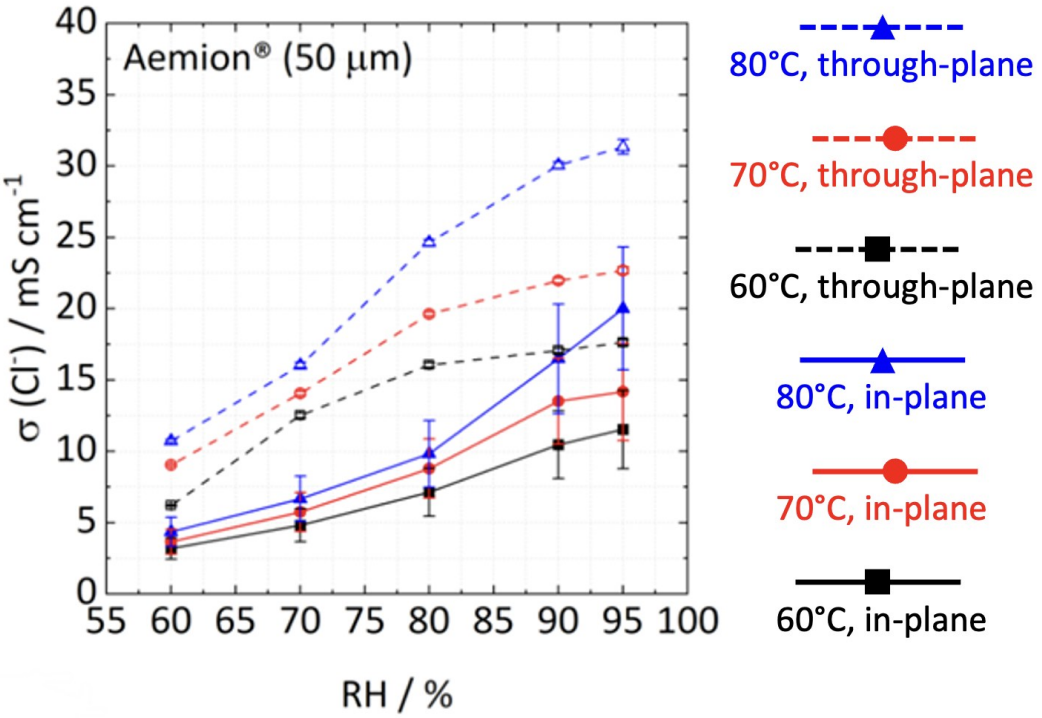

Figure 3-20. The Cl^- conductivity of AF1-HNN8-50 (monolithic 50 µm Aemion®) in both in-plane and through-plane directions at 60°C, 70°C and 80°C and 60 % - 95 %RH. Adapted from Ref[49]

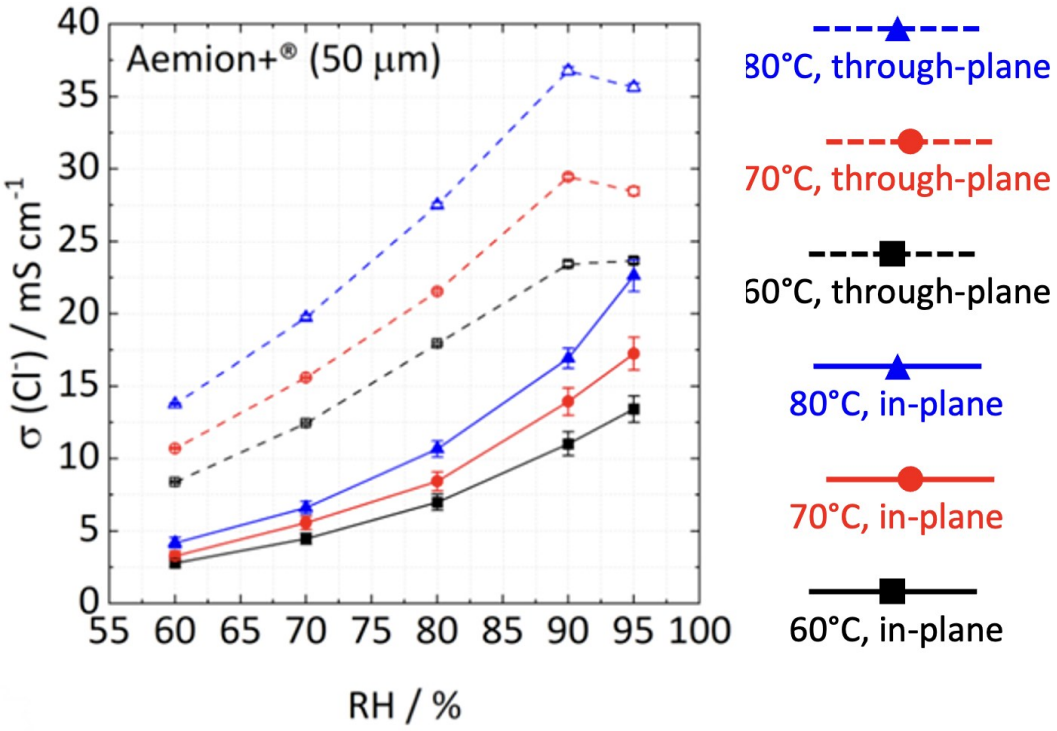

Figure 3-21. **The Cl^- conductivity of AF2-INN8-50 (monolithic 50 µm Aemion+®) in both in-plane and through-plane directions at 60°C, 70°C and 80°C and 60 % - 95 %RH. Adapted from Ref[49]**

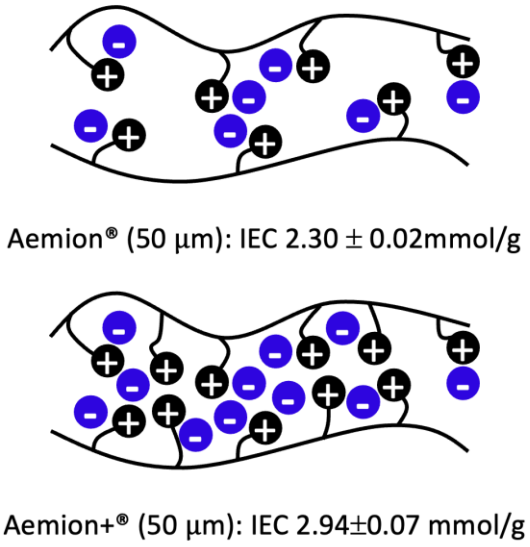

Figure 3-22. **Schematic representation of the effect of ion exchange capacity on membrane conductivity. AF1-INN8-50 (Aemion®) membrane is a monolithic, 50 µm, poly(benzimidazolium) based polymer possess a IEC of 2.30 mmmol/g. AF2-INN8-50 (Aemion+®) membrane is a monolithic, 50 µm, poly(imidazolium) based polymer possess a IEC of 2.94 mmmol/g**

Next, the Cl^- conductivity of two membranes with the same base polymer was compared to illustrate the effect of addition of reinforcement substrate on the membrane conductivity. The 40 µm reinforced Aemion+® (AF2-HLE8-40, Figure 3-23) shows similar Cl^- conductivity values compared to the 50 µm monolithic Aemion+® (AF2-HNN8-50, Figure 3-21) for in-plane direction at all tested conditions (60°C, 70°C and 80°C and 60 % - 95 %RH). However, the through-plane Cl^- conductivity of the 40 µm reinforced Aemion+® (AF2-HLE8-40,Figure 3-23) shows only 10% of the 50 µm monolithic Aemion+® (AF2-HNN8-50, Figure 3-21). This difference of the Cl^- conductivity in through-plane direction can be explained by more complex ionic pathway for the membrane with a 70-80% porous polyolefin reinforcement substrate. As shown in Figure 3-24, the anion transported through the ion-conducting channels of the

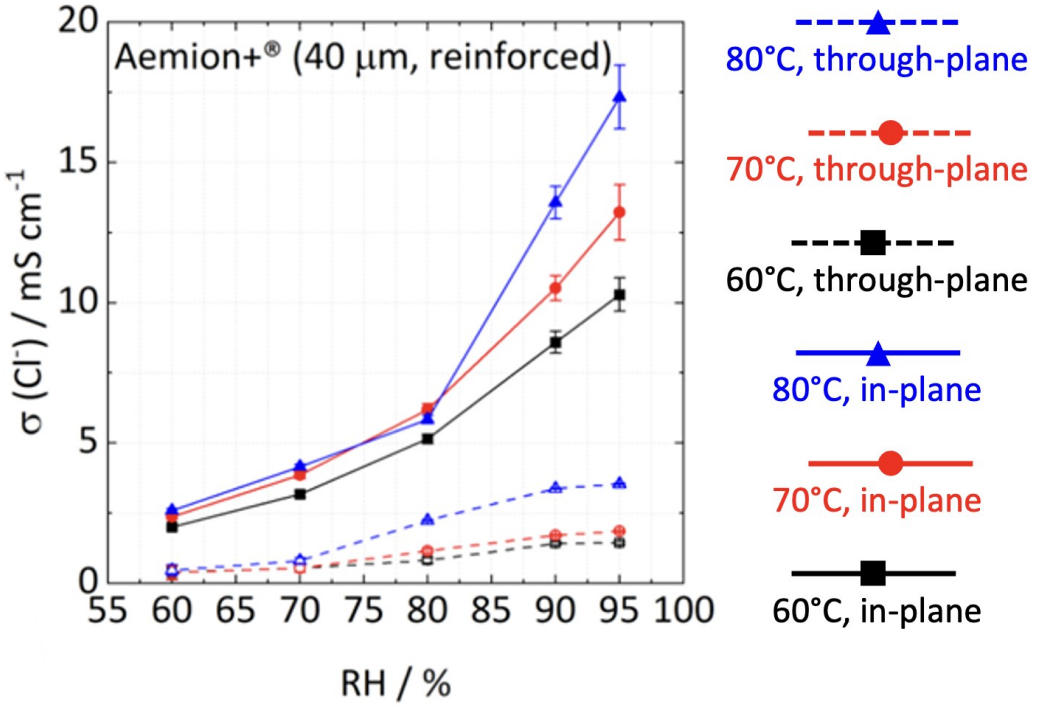

Figure 3-23. The Cl^- conductivity of AF2-HLE8-40 (reindorced 40 µm Aemion+®) in both in-plane and through-plane directions at 60°C, 70°C and 80°C and 60 % - 95 %RH. Adapted from Ref[49]

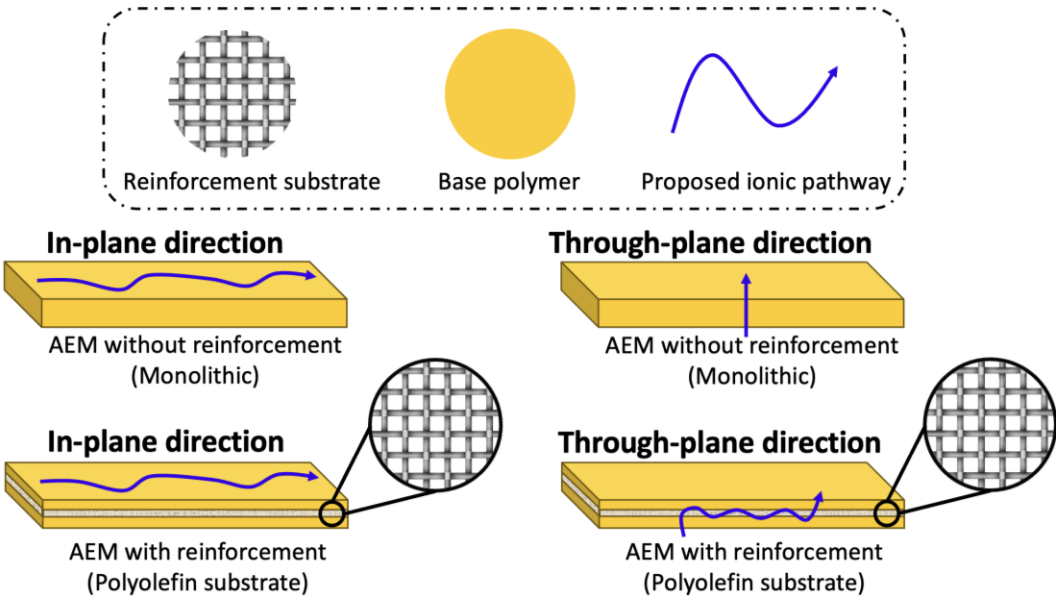

Figure 3-24. Schematic representation of the effect of reinforcement substrate on membrane conductivity for both in-plane and through plane direction

Lastly, a 10 μm ultra-thin reinforced Aemion+® (AF2-HLE8-10, Figure 3-25) was compared to the 40 μm ultra-thin reinforced Aemion+® (AF2-HLE8-40, Figure 3-23). The Cl^- conductivity of the 10 μm and 40 μm reinforced Aemion+® for both in-plane and through-plane conductivity are the same, because the conductivity of a membrane is the experimentally measured conductance normalized by the dimension of the membrane.

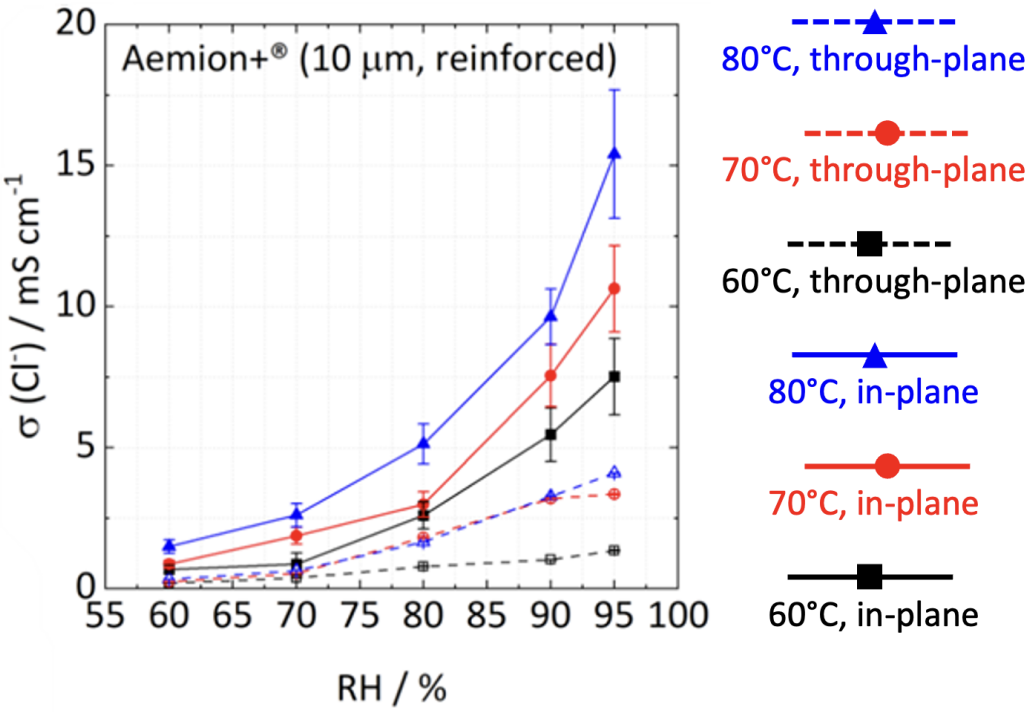

Figure 3-25. The Cl^- conductivity of AF2-HLE8-10 (reindorced 10 µm Aemion+®) in both in-plane and through-plane directions at 60°C, 70°C and 80°C and 60 % - 95 %RH. Adapted from Ref[49]

In summary, the through-plane and in-plane conductivity of the four membranes (AF1-INN8-50, AF2-INN8-50, AF2-HLE8-40, AF2-HLE8-10) are summarized in Figure 3-26. The anisotropic property of a membrane material describes the membrane property along various axies and is reported as the ratio (TP/IP) of through-plane conductivity and in-plane conductivity. The anisotropic ratio of all four membranes (AF1-INN8-50, AF2-INN8-50, AF2-HLE8-40, AF2-HLE8-10) are summarized in Figure 3-27.

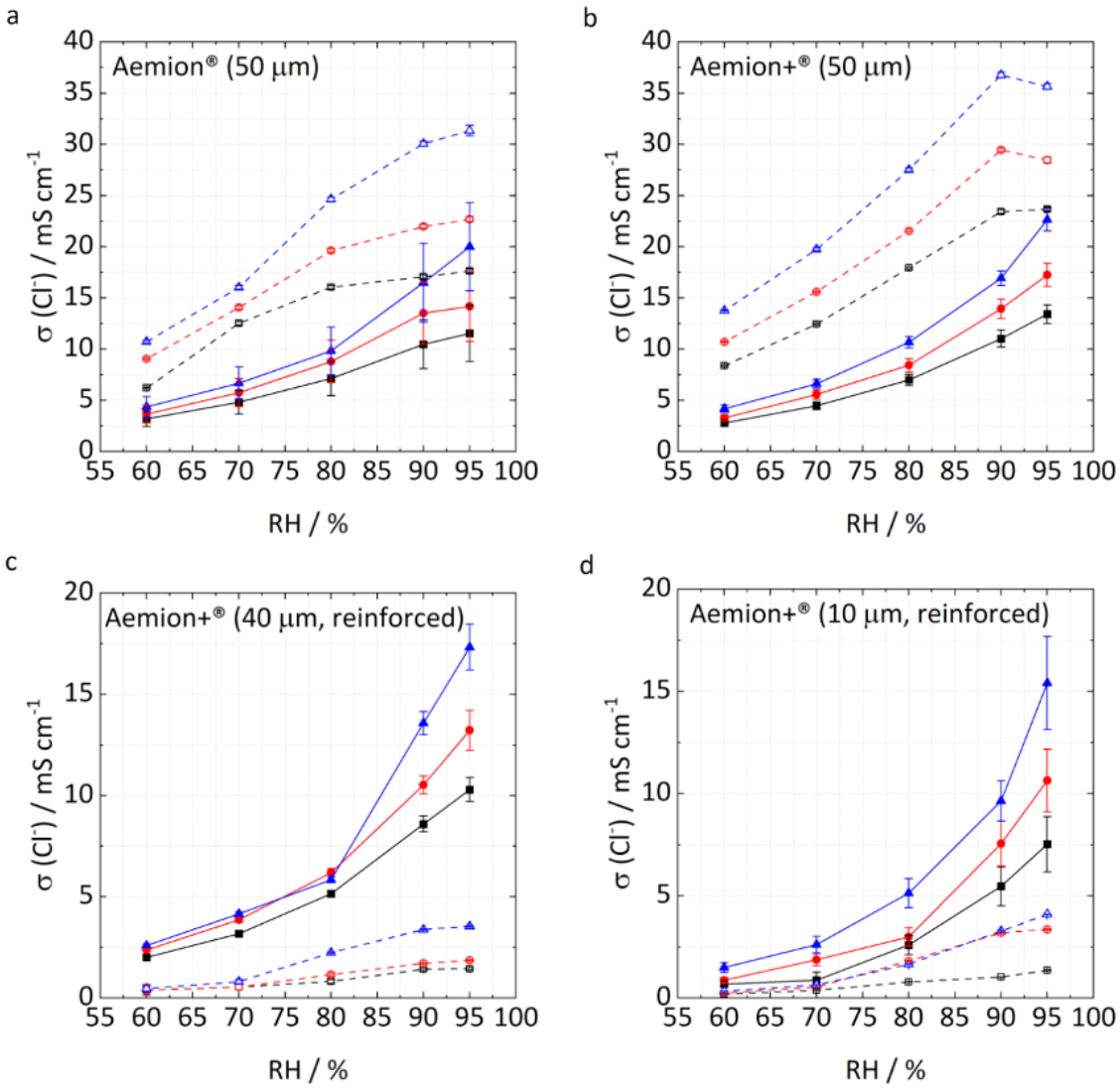

Figure 3-26. In-plane (solid) and through-plane (dashed) Cl^- conductivity for all AEMs tested at 60°C (black), 70°C (red) and 80°C (blue). Adapted from Ref[49]

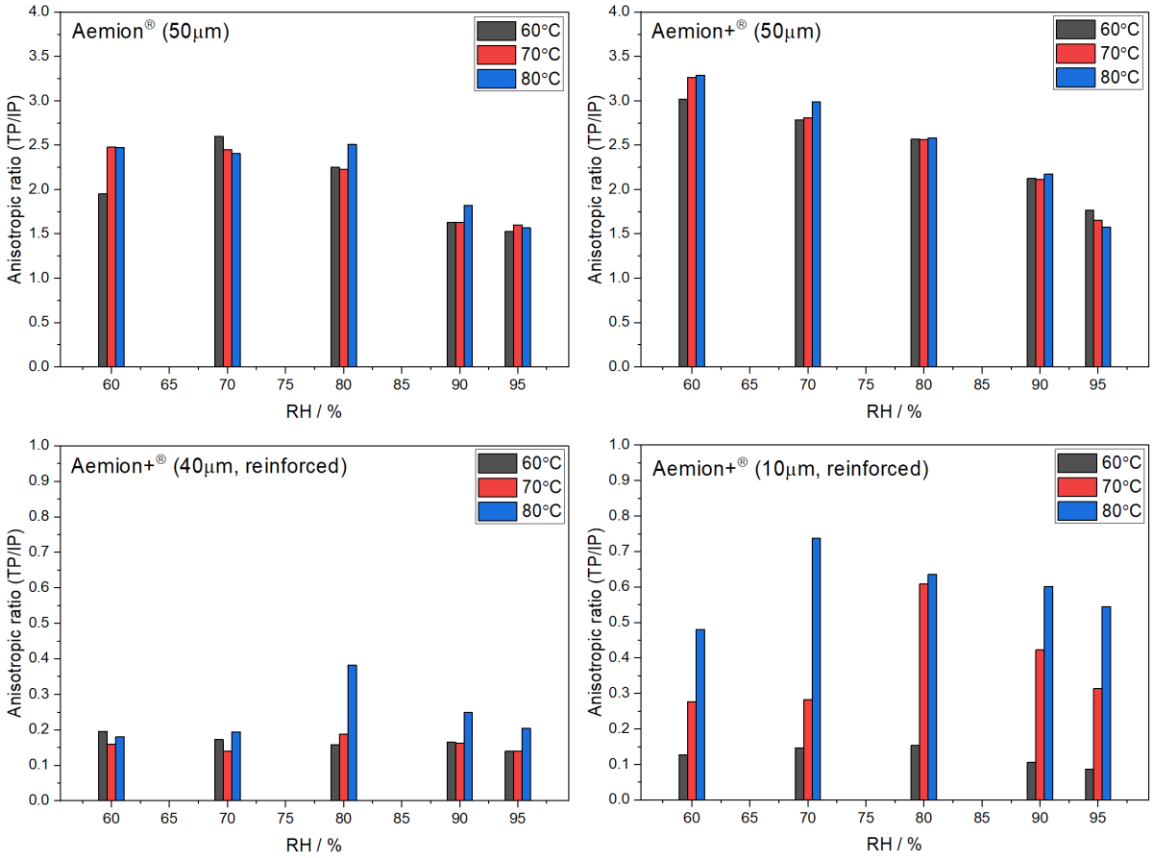

Figure 3-27. Anisotropic ratio of the through-plane conductivity versus in-plane conductivity for all AEMs in its Cl^- form tested at 60°C (black), 70°C (red) and 80°C (blue).

Comparison of Cl^- conductivity for membranes with and without reinforcement composite

As shown in Figure 3-26, the conductivity of the monolithic membranes (Figure 3-26 a and b) displays higher through-plane conductivities (dash line) than their in-plane conductivities (solid line). Ziv et al also reported through-plane conductivity values higher than their in-plane conductivity values for imidazolium based monolithic membranes.[60] However, opposite trend was observed for the membranes with reinforcement composite (Figure 3-26 c and d), where the in-plane conductivities(solid line) was found to be higher than the through-plane conductivities (dash-line). This could be explained that the addition of reinforcement composite hindered the ion transport in the through-plane direction, particularly for the reinforcement membranes with a non-ion conducting composite.

Comparison of Cl^- conductivity for membranes with reinforcement composite at various thickness

Similar conductivity values were observed for the 10 μm membrane with reinforcement composite and the 40 μm membrane with reinforcement composite in the in-plane direction (dash line in Figure 3-26 c and d); however, the 40 μm membrane shows higher in-plane conductivity than the 10 μm membrane at each temperature and relative humidity. The improved in-plane conductivity on a thicker membrane could be explained as a thicker polymer domain on the surface of the membrane provides a better ionic pathway.

3.3.6. Comparison of water uptake and hydration number for selected anion exchange membranes in their Cl^- form

As shown in Figure 3-26, all four membranes (AF1-INN8-50, AF2-INN8-50, AF2-HLE8-40, AF2-HLE8-10) shows increased conductivity for both in-plane and through-plane direction as the relative humidity (RH%) increases. As shown in Figure 3-28, the increased conductivity at high RH% is explained the ion conducting channels are filled with water and expand when the membrane absorbs water.[58]

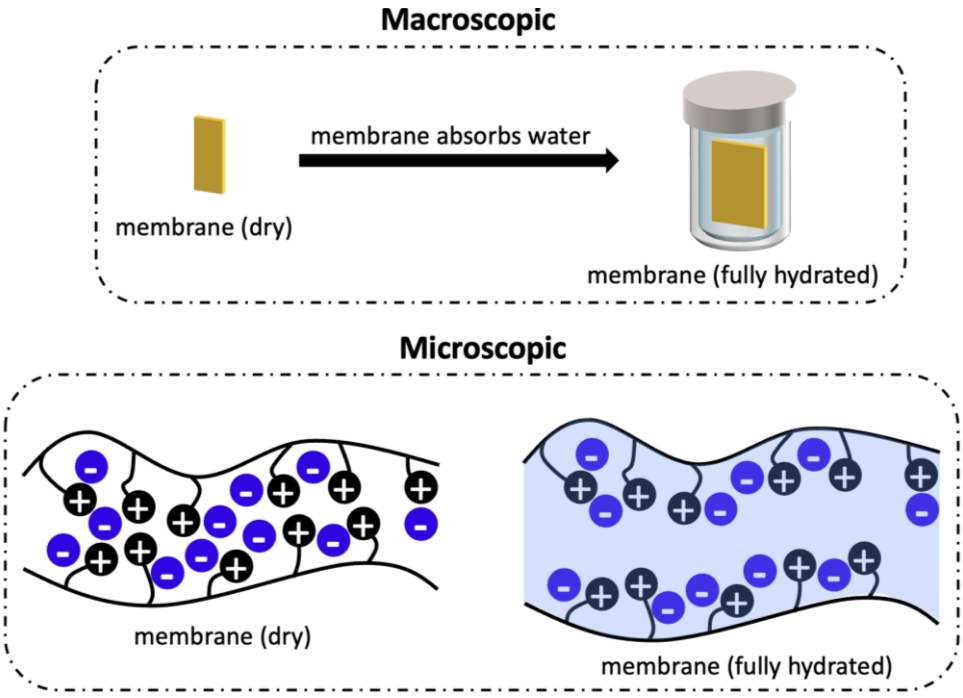

Figure 3-28. Schematic representation of the effect of the hydration level on the membrnae conductivity. Adapted from ref[49]

The hydration number (λ) is introduced to explain the relationship between the water content and the conductivity of the membrane. The hydration number (λ) is calculated as the ratio of the number of water molecules to the number of charged (cationic) sites of the polymer. [58] The water uptake (WU) and hydration number (λ) of monolithic Aemion® and Aemion+® increases when temperature is increased as shown in Figure 3-29, which is consistent with those reported for polyarylimidazolium AEMs.[50] However, the water uptake (WU) and hydration number (λ) of the reinforced Aemion+® did not increase as much when the temperature was decreased, which can be explained as the water uptake (g H_2O/g polymer) is limited by the mass fraction of polyolefin reinforcement. Reinforced Aemion+® containing hydrophobic polyolefin has decreased water uptake (WU =0.53 g H_2O/g polymer) in comparison to monolithic Aemion+® (0.73 g H_2O/g polymer) when soaked with water. The same is true when humidity is limited in the gas phase as with the DVS in Figure 3-29. However, reinforcement has a minimal cost to the hydration of ions ($\lambda \sim$ WU/IEC) in Aemion+®, for which no significant difference is calculated at limited humidity, and a difference of only $\lambda = 2$ is estimated when the membranes are soaked in water.

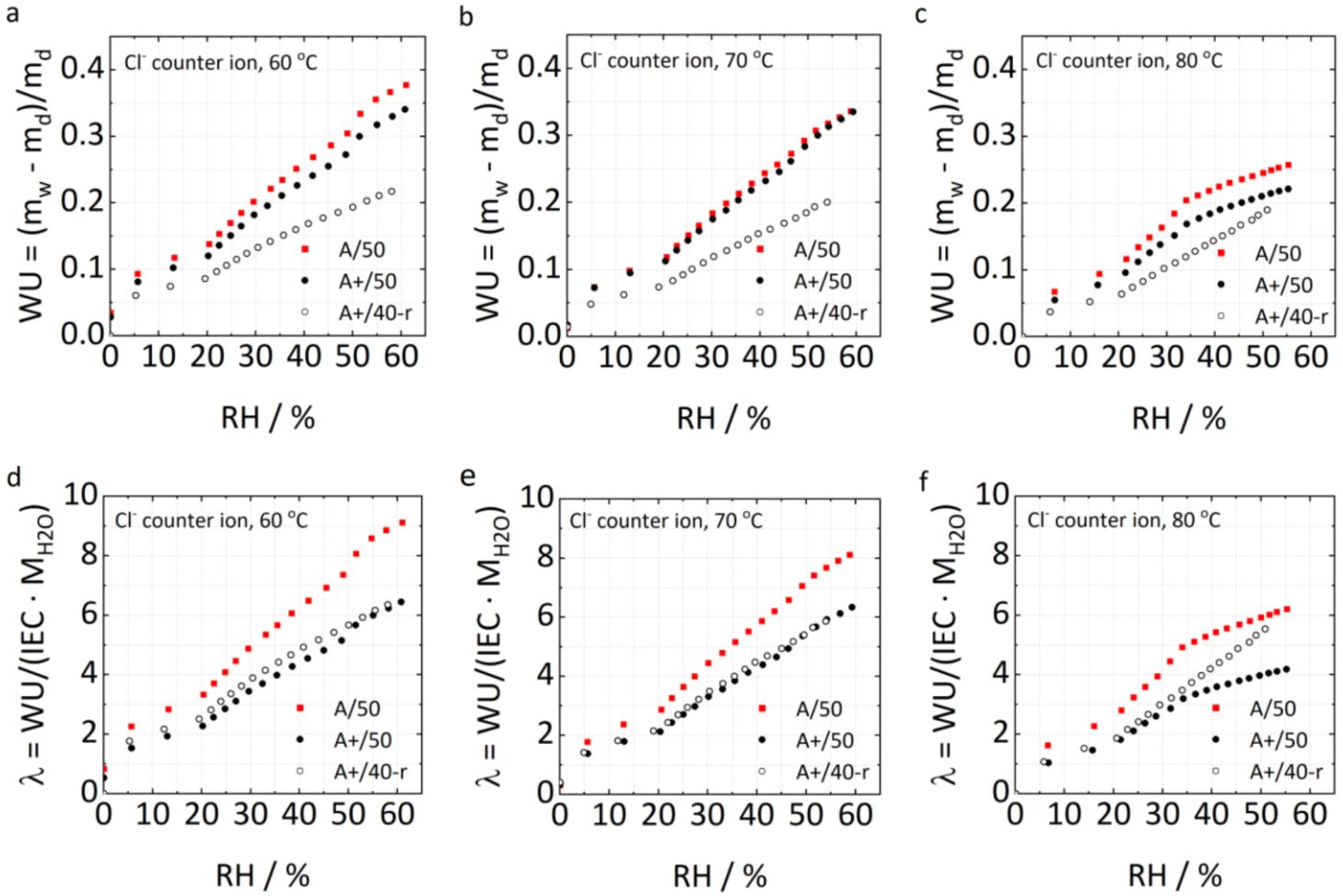

Figure 3-29. DVS for all three temperatures and AEMs investigated in the AEMFC study. Thicker variants were used for direct comparison with the ex-situ conductivity measurements. All isotherms were acquired in the desorption direction (high RH to low). Materials characterized are: Aemion®, 50 µm (red: A/50), Aemion+®, 50 µm (black: A+/50), Aemion+®, 40 µm, reinforced (white: A+/40-r). Adapted from ref[49]

3.4. Summary and future work

The addition of the polyolefin reinforcement composite allows the production of ultra-thin membranes and reduces the thickness of polyimidazolium-based AEM to 10 μm. As shown in Figure 3-26, the 10 μm reinforced Aemion+® membrane shows similar in-plane conductivity values compared to the 50 μm monolithic Aemion+® membrane. Because conductivity values are normalized to the membrane's dimensions, using a thinner membrane with similar conductivity values would decrease the resistance between the electrode, and thus potentially improve the fuel cell performance by decreasing the resistance between the two electrodes.

Compared to the modification of the polymer structure from 1st generation Aemion® to the 2nd generation Aemion+®, the addition of the polyolefin reinforcement, shows bigger effect on a membrane's conductivity values. As shown in in Figure 3-26, the 50 μm monolithic Aemion® material shows similar conductivity values compared to for both in-plane and through-plane directions. In contrast, the 40 μm reinforcement Aemion+® membrane shows half of the conductivity values compare to the 50 μm monolithic Aemion+® membrane. The decreased conductivity of the reinforced membrane could be explained by the lower water uptake values with the addition of polyolefin reinforcement. As shown in Figure 3-29, the addition of polyolefin reinforcement in the 40 μm reinforcement Aemion+® decreases the water uptake by 40%, while the modification of the polymer structure from the 50 μm Aemion® to the 50 μm Aemion+® only decreases the water uptake by 10% at 60°C and 60% RH. At elevated temperatures, the gap of water uptake between three samples are observed to decrease especially at 80°C.

In addition, the addition of polyolefin reinforcement composite also significantly changed the anisotropic properties of the membrane. As shown in Figure 3-27, both the 1st generation Aemion® and 2nd generation Aemion+® monolithic polyimidazolium-based membranes shows higher conductivity values in its through-plane direction than the in-plane direction at each temperature and RH%, while the reinforced membranes shows the opposite trend. Therefore, it is important to perform morphological studies to understand the effect of adding reinforcement composite to polyimidazolium-based membranes.

The conductivity work presented here was obtained using ex-situ characterization techniques. In an electrochemical device, the membranes were usually coated with catalyst on each side to facilitate the cathode and anode reactions. Therefore, in-situ studies are needed to study the effect of the polyolefin composite to the membrane electrode assembly and its contribution of fuel cell performance. Future work could involve studying how the addition of reinforcement composites in the AEM affect the fuel cell performance when operated with humidified gas fuels at various temperatures.

Chapter 4. Visualization of hydroxide ion formation upon electrolytic water splitting in an anion exchange membrane

This chapter have been reproduced with permission from the peer-reviewed article published as Cao, X.; Novitski, D.; Holdcroft, S. Visualization of Hydroxide Ion Formation upon Electrolytic Water Splitting in an Anion Exchange Membrane. ACS Materials Lett. 2019, 1 (3), 362–366. https://doi.org/10.1021/acsmaterialslett.9b00195 from American Chemical Society.

This work was financially supported by Natural Sciences and Engineering Research Council of Canada (NSERC).

Individual contributions were: X.C. cast all the membranes and performed all the ex-situ characterizations. D.N. and S.H. advised and supervised the work.

4.1. Abstract

Measurement of hydroxide ion conductivity is paramount to understanding anion exchange membranes (AEM) operated under alkaline conditions, but the measurement is complicated by dissolved CO_2 and the presence of bicarbonates and carbonates. A technique for accurate measurement has recently been reported that involves measuring the conductivity during water splitting, wherein hydroxide ions are assumed, but not proven, to be produced at the cathode and which purge out other anions. In this preliminary study, we visualize the formation of hydroxide ions and their diffusion from the cathode to anode. We do this by way of an anion exchange membrane cast with an acid/base pH indicator, such that visual confirmation of hydroxide production at the cathode is obtained during application of sustained current load. This proof of concept is demonstrated using the AEM, hexamethyl-p-terphenyl poly(methylbenzamidazolium), and pH indicator, thymolphthalein, included at 0.1 and 0.2 wt% concentration. An additional novelty of this work is that we perform conductivity measurements under potentiostatic load rather than galvanostatic load, which we find substantially increases (6x faster) the time required for the membrane to reach a steady state membrane conductivity.

4.2. Introduction

Anion exchange membrane (AEM) fuel cells operate by generating hydroxide anions at the cathode which are then transported to the anode through the membrane.[6,94] It has long been a problem where upon exposure to ambient atmosphere the hydroxide ions in the membrane rapidly convert to carbonate and/or bicarbonate anions via reaction with carbon dioxide.[95–97] Recently, Krewer et al. used a physiochemical model to draw the concentration profiles of bicarbonate, carbonate and hydroxide anions and found that the impact of CO_2 on the performance of anion exchange membrane fuel cells (AEMFCs) can be limited when operating at high current densities due to the purging of (bi)carbonate ions with electrolytically-formed hydroxide ions.[98] As such, in measuring hydroxide ion conductivity ex-situ, it has until recently been necessary to completely exclude CO_2.[99] To subvert this process a novel technique was reported in which conductivity is measured during electrolysis to produce hydroxide

ions which are assumed to flush out mixed carbonates, akin to the self-purging process that occurs in a fuel cell.[100–103]

In reviewing the literature, it occurred to us that hydroxide ion production in the above electrolytic process is inferred, albeit reasonably.[104] We therefore examined the pH change upon electrolysis using red-cabbage juice indicator dropped on top of a membrane after electrolysis and witnessed a color change from red to blue, indicating an increase in pH, i.e., an increase in hydroxide ion concentration. This provided the idea of creating a color sensitive anion exchange material by co-casting an AEM in the presence of an acid/base indicator. In fact, it has been previously reported that pH indicator strips may be prepared from poly(ionic liquids) and anionic dyes, and because of the interaction of the dye with the polycation leaching of the dye is prevented.[105] The fabrication of pH-color sensitive AEMs for visualizing pH changes may open up new avenues for diagnostic and sensor applications using any one of a variety of pH indicators and/or anion exchange materials.

4.3. Experiment

The anion exchange membrane used to demonstrate the concept was hexamethyl-p-terphenyl poly(methylbenzamidazolium) (HMT-PMBI, Figure 4-1) possessing 89% degree of methylation. The IEC is 1.90 mmol g^{-1} in its I^- form and 2.46 mmol g^{-1} in its OH^- form. The details of synthesis and characterization of HMT-PMBI are omitted in this work but reported elsewhere.[106,107] The acid-base indicator used in the present work was thymolphthalein (Eastman Organic Chemicals), chosen because of its relevant pH range of 9.4 -10.6 where the change of counter-ion from the carbonate/bicarbonate mixture to hydroxide ion takes place. Upon a second deprotonation above pH 9.3 (Figure 4-2) thymolphthalein turns from colorless to blue.[108]

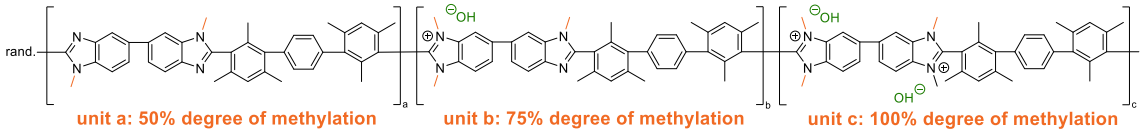

Figure 4-1. Chemical structure of HMT-PMBI (I^-), where the degree of methylation (of the N-atoms) is 89% and I^- denotes it is in the iodide form.

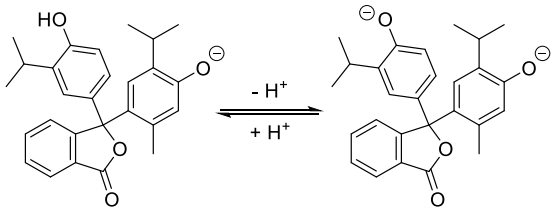

Figure 4-2. Chemical structure of thymolphthalein with varied pH environment. Adapted from ref[51]

HMT-PMBI anion exchange membranes were prepared with either 0.1 wt% or 0.2 wt% thymolphthalein, achieved by co-casting from DMSO solutions. Membrane thicknesses were 43 μm and 47 μm for 0.1 wt% and 0.2 wt% thymolphthalein membranes, respectively. Membranes were prepared and stored with HMT-PMBI in its I^- form. Membranes were immersed in 1M KCl, $KHCO_3$, K_2CO_3 and KOH prepared with Milli-Q water overnight in order to convert them to Cl^-, HCO_3^-, CO_3^{2-} and OH^- form. The membranes were then rinsed in Milli-Q water to remove excess salt solution prior to conductivity and color test.

Membranes in their air-equilibrated OH^- form (i.e., mixed carbonate form) were clamped in a 4-electrode sample holder consisting of an anode, cathode, and two reference electrodes (RE1 and RE2), as shown in Figure 4-3. The holder was loaded into an MTS 740 (Scribner Associates) conductivity cell and operated under constant flow of 500 sccm min^{-1} N_2 balanced with 2% H_2, with the temperature and RH (relative humidity) maintained at 40 °C and 90% RH, respectively.

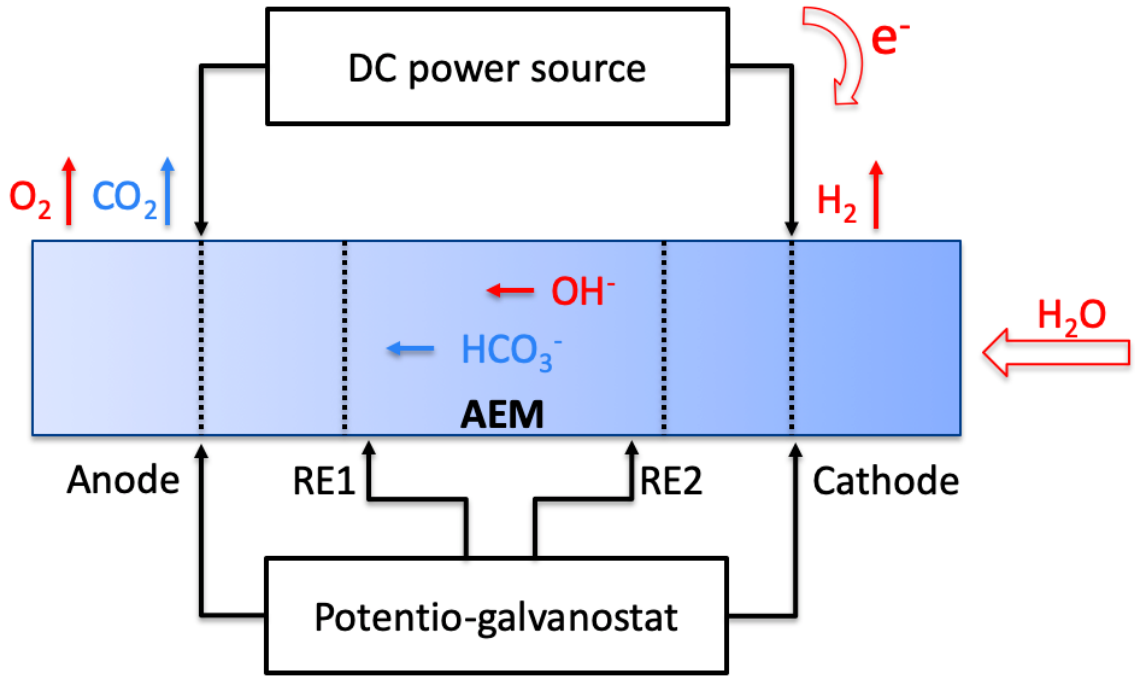

Figure 4-3. Schematic view of the AEM showing current flow and ion transport under potentiostatic water electrolysis and hydroxide formation at the cathode. Adapted from ref[51].

A voltage of 1.75 V was applied across the anode and cathode using a Solartron SI 1260. OH^- ions and H_2 gas were generated at the cathode according to Equation 4-1.

Equation 4-1 $$2H_2O + 2e^- \rightarrow 2OH^- + H_2$$

Anions, including the initially present mixed carbonate/bicarbonate and the electrolytically produced OH^-, diffuse towards the anode. At the anode, carbonate and bicarbonate anions are expelled from the system according to Equation 4-2. Hydroxide ions are oxidized to water and O_2 gas according to Equation 4-3.

Equation 4-2 $$HCO_3^- \rightleftarrows CO_2 + OH^-$$

Equation 4-3 $$4OH^- \rightarrow 2H_2O + O_2 + 4e^-$$

The ionic conductivity (σ) of the AEM was calculated after of 20 min applied potential treatment via:

Equation 4-4 $$\sigma = \frac{l}{AR}$$

where l represents the distance between the two reference electrodes (0.425 cm), A is the cross-sectional area of the membrane in cm^2, and R is the average membrane resistance (in Ω) measured by five potentiodynamic sweeps between + 0.1 V and – 0.1 V. By monitoring the AEM conductivity using potentiodynamic sweeps during the continuous production of hydroxide, a steady state AEM conductivity emerged.

UV-Vis spectroscopy measurements were carried out using a Cary 100 Bio UV-visible spectrometer with the membrane sandwiched between two quartz plates. The scan speed was 600 nm min^{-1} and a baseline correction was carried out using two quartz plates prior to each measurement. For each AEM sample, UV-vis absorption spectra were taken before and after the potential controlled production of hydroxide ions, and after the AEM sample was re-exposed to air (containing 400 ppm CO_2).

4.4. Results and discussion

4.4.1. Red cabbage juice indicator

The plant-based dyes were extracted by blending red cabbage with water, and the filtered liquid stored at room temperature prior to use. Because the red cabbage contains high concentration of anthocyanin (red/blue) dyes and flavonol (colorless/yellow) dyes, the red cabbage juice indicator would display red at low pH, purple at neutral pH and yellow at high pH as shown in Table 4-1.

Table 4-1. Colors of red cabbage juice indicator at various pH values. Adapted from ref[109].

pH	1	2	3	4	5	6	7	8	9	10	11	12	13	14
Color		Red			Pink			Purple			Blue			Green			Yellow

Prior the water electrolysis reaction, the red cabbage juice indicator applied to the pristine HMT-PMBI shown purple color indicating a neutral pH in its HCO3- form as shown in Figure 4-4 (left). The electrolytically generating OH- which flushed out the HCO3- initially presented in the pristine HMT-PMBI were reflected by the color change of the red cabbage juice indicator. As shown in Figure 4-4 (right), the color of the red cabbage juice displayed a green color on the anode side and yellow color on the cathode side of the pristine HMT-PMBI after electrolysis, which indicating a significant

of increase of OH- concentration at the cathode area after the water electrolysis reaction.

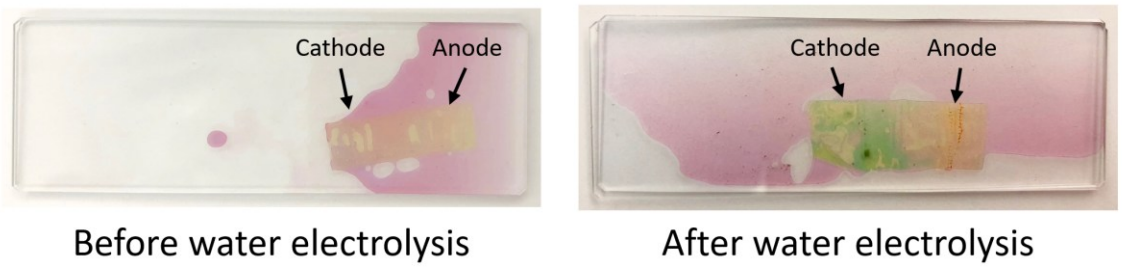

Figure 4-4. Color of red cabbage juice indicator changed from purple to green after water electrolysis, indicating the counter ion of the pristine HMT-PMBI membrane changed from HCO_3^- to OH^- after water electrolysis reaction

4.4.2. Thymolphthalein indicator

Due to the difficulty of extracting the active dyes from red cabbage juice, thymolphthalein pH indicator powder was selected for its simplicity to modify its concentration to the polymer by weight. The method of integrating the pH indicator to the polymer membrane was solvent cocasting. Therefore, the solubility and color change properties of the thymolphthalein pH indicator were tested in the solvents commonly used in membrane casting and treatment process: water, DMSO, methanol, ethanol. As shown in Figure 4-5, thymolphthalein dissolved in all above solvents and displays expected red in acidic environment and blue in basic environment.

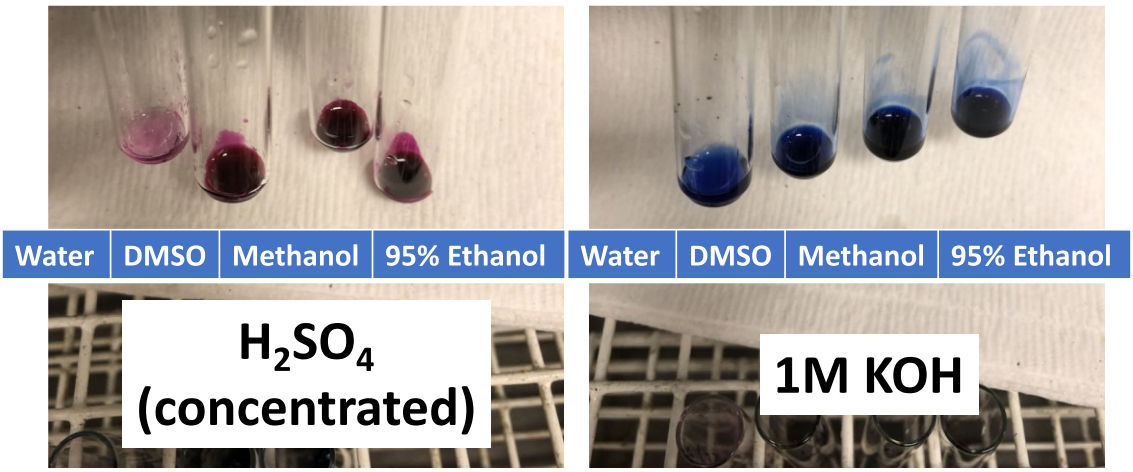

Figure 4-5. Color of thymolphthalein indicator dissolved in water, DMSO, methanol and ethanol solvents at acidic (H_2SO_4) and basic (KOH) conditions

4.4.3. Optimization of co-casting ratio using thymolphthalein indicator

To find the optimal co-casting ratio of the thymolphthalein indicator and polymer for the pH-sensitive anion exchange membrane, six samples were prepared with indicator to polymer ratio ranging from 1:1 to $1:10^6$ as shown in Table 4-2. The casting solvent was chosen to be DMSO due to is high boiling point, which evaporates slowly over time and leaves a smooth membrane.

Table 4-2. Co-casting ratio of thymolphthalein indicator and polymer.

Sample ID	001	002	003	004	005	006
$m_{indicator}$ (g)	0.9785	0.017	0.0015	1.61E-04	1.65E-05	1.59E-06
$m_{membrane}$ (g)	0.8885	0.1738	0.1743	0.1636	0.168	0.1622
m_{DMSO} (g)	9.82	1.69	1.71	1.62	1.68	1.62
mass ratio (membrane/indicator)	1:1	1:10	1:116	1:1018	1:10187	1:101873

For visual demonstration of the ion flushing process, the thymolphthalein co-casted membrane should possess a blue color at high pH, which reflecting the blue color of the thymolphthalein indicator deprotonated form, and a yellow color at low pH, which reflecting the yellow color of the pristine HMT-PMBI membrane, which reflecting the colorless of the thymolphthalein indicator in its protonated form. As shown in Figure 4-6, the thymolphthalein HMT-PMBI co-casted membranes with an indicator to polymer ratio of 1:1 and 1:10 shows intense blue when immersed in 1M KOH; while the co-casted membranes with a $1:10^4$ and $1:10^5$ ratio shows yellow when immersed in 1M KOH. Therefore, the optimal range of the for visual demonstration lies in the range of $1:10^2$ and $1:10^3$ ratio, which shows distinguishable blue when immersed in 1M KOH.

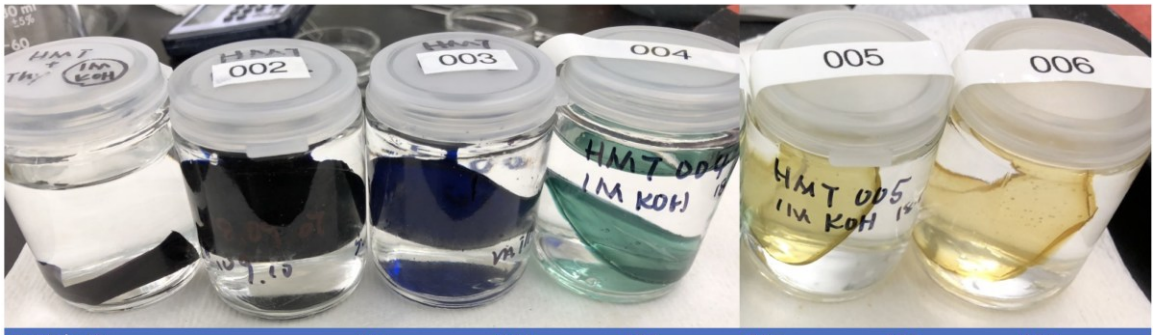

Figure 4-6 Color of thymolphthalein indicator cocasted HMT-PMBI membrane with a indicator to polymer cocasting ratio between 1:1 to $1:10^5$ by mass.

A quick reversibility test was performed on the thymolphthalein indicator HMT-PMBI co-casted membranes by adding a small chuck of dry ice (~ 3 cm^3) to the OH^- form of the co-casted membranes. A large amount of CO_2 was released from the sublimation of dry ice, which reacted with the OH^- ions presented in the membrane and converted the counter ion to HCO_3^- and CO_3^{2-}. As shown in Figure 4-7, the thymolphthalein and HMT-PMBI co-cast membrane with a co-casting ratio of $1:10^3$ shows a yellow band on the path of the dry ice sublimation, which displays a great contrast to its original green color when immersed in 1 M KOH. The thymolphthalein and HMT-PMBI co-cast membrane with a $1:10^2$ indicator to polymer ratio displays a lighter blue band along the area of dry ice sublimation. Therefore, the optimal co-cast ratio for visualizing the counter ion change in an anion exchange membrane should be around $1:10^3$.

Figure 4-7. Color change of the thymolphthalein and HMT-PMBI co-casted membranes. The membranes were initially exchanged to its OH^- form by immersing in 1 M KOH. A lighter blue band was observed after adding a small chunck of dry ice for the membrane co-casted with an indicator to polymer ratio of $1:10^2$ (left), while a yellow band was observed for the membrane co-casted with a $1:10^3$ indicator to polymer ratio (right).

4.4.4. Thymolphthalein and HMT-PMBI co-cast membrane

The thymolphthalein indicator and HTM-PMBI co-casted membranes with a casting ratio of 0.1 wt% and 0.2 wt% were found to display different colors in solutions of different pH as shown in Figure 4-8. Here, membranes were immersed in pure water (pH = 7.0, measured) and in aqueous solutions of 1M $KHCO_3$ (pH = 8.1), 1M K_2CO_3 (pH = 12.1), and 1M KOH (pH = 13.6). Pristine HMT-PMBI retains its yellow color in all solutions, while thymolphthalein-containing membranes display colors ranging from yellow in lower pH solutions (water and $KHCO_3$) to blue in the higher pH solutions (K_2CO_3 and KOH). The stark color differences confirm that co-cast AEM/indicator membranes provide visual evidence of the concentration of hydroxide ion in the membrane.

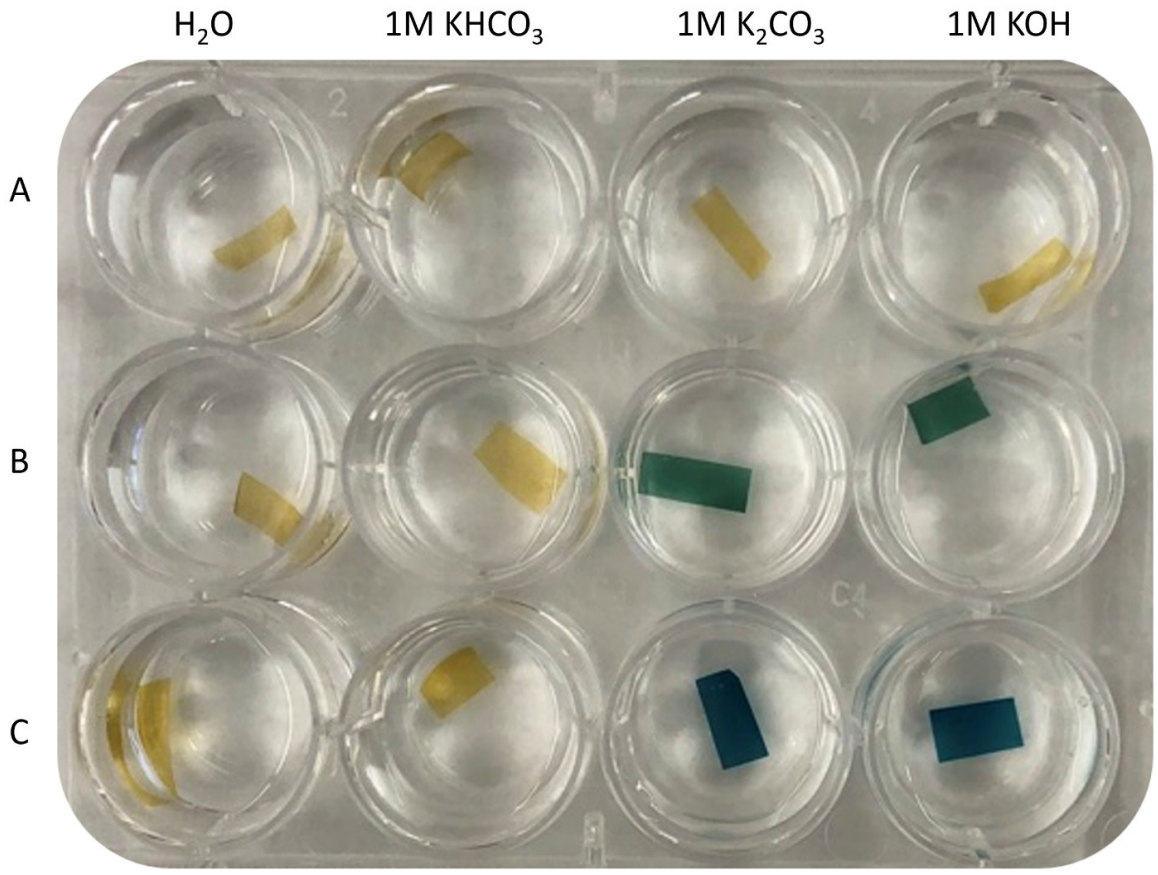

Figure 4-8. Color of HMT-PMBI/thymolphthalein membranes in water (7.0, measured), 1M $KHCO_3$ (pH = 8.1), 1M K_2CO_3 (pH = 12.1), and 1M KOH (pH = 13.6). Row A: pristine HMT-PMBI; Row B: HMT-PMBI with 0.1 wt% thymolphthalein; Row C: HMT-PMBI with 0.2 wt% thymolphthalein. Adapted from ref[51]

In addition, the UV-vis spectra of pristine HMT-PMBI membranes were compared with the HMT-PMBI co-casted with 0.1 wt% and 0.2 wt% membranes to support the color difference in various counter ion form. The pristine HMT-PMBI displays a yellow color regardless the counter ion as shown in Figure 4-8 row A, which was supported by no absorbance at the visible light range (380 nm – 750 nm) in its UV-vis spectra as shown in Figure 4-9. The HMT-PMBI co-casted with 0.1 wt% thymolphthalein indicator displays green color when immersed in 1M $KHCO_3$ and 1M KOH while remains yellow color (Figure 4-8 row B). The green color of the 0.1 wt% thymolphthalein co-casted HMT-PMBI membrane was quantified as an absorption peak of 0.4 at 607 nm (Figure 4-10 left), and the yellow color at high pH condition shows same absorption spectra as the pristine HMT-PMBI. By increasing the concentration of

thymolphthalein in the co-casted membranes by 0.1 wt%, the absorption peak at 607 nm doubled as shown in Figure 4-10 right.

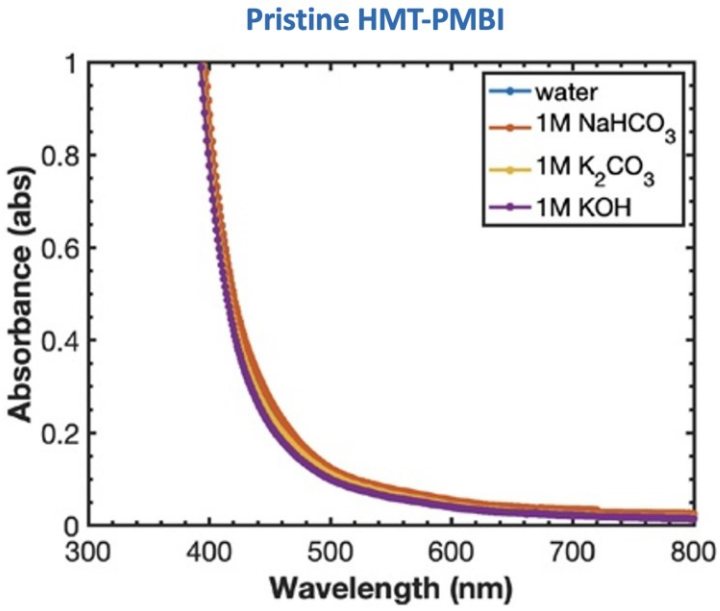

Figure 4-9. UV-vis spectra of pristine HMT-PMBI membranes in its Cl^- form, HCO_3^- form, CO_3^{2-} form and OH^- by immersing in deionized water, 1M $NaHCO_3$, 1M K_2CO_3 and 1M KOH solutions.

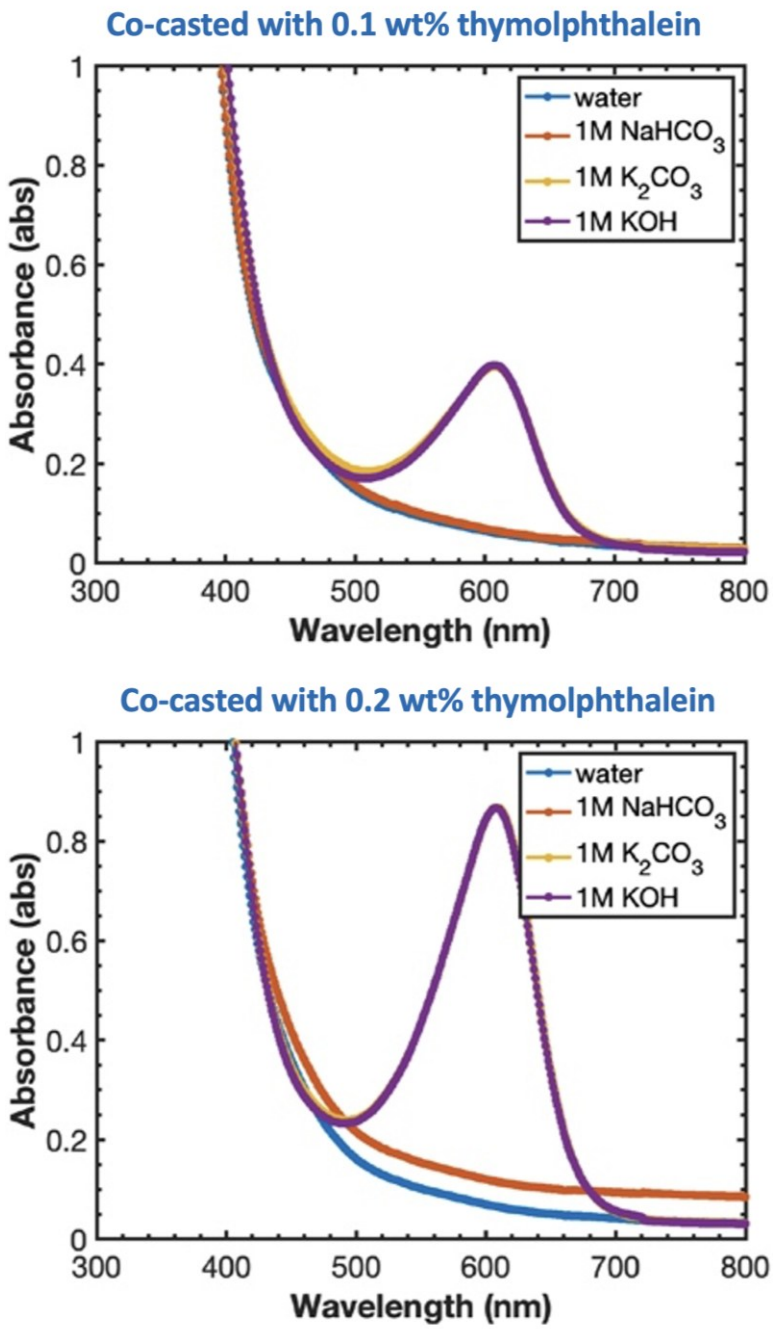

Figure 4-10. UV-vis spectra of HMT-PMBI co-casted with 0.1 wt% (top) and 0.2 wt% (bottom) of thymolphthalein indicator membranes in its Cl^- form, HCO_3^- form, CO_3^{2-} form and OH^- by immersing in deionized water, 1M $NaHCO_3$, 1M K_2CO_3 and 1M KOH solutions.

4.4.5. Visualizing the counter ion change during water electrolysis

In order to observe the change in hydroxide ion concentration in the membrane during water electrolysis, evidence of a colour change was captured by video (**Video**

S1). As observed in **Figure 5**, as the electrolysis of water proceeds, a blue band spreads through the membrane from cathode to anode through the entire membrane, providing corresponding evidence of the increase in pH due to the formation and diffusion of OH^-. After prolonged electrolysis the pH of the entire membrane is increased except over the anode where hydroxide ion is consumed, and the pH is much lower.

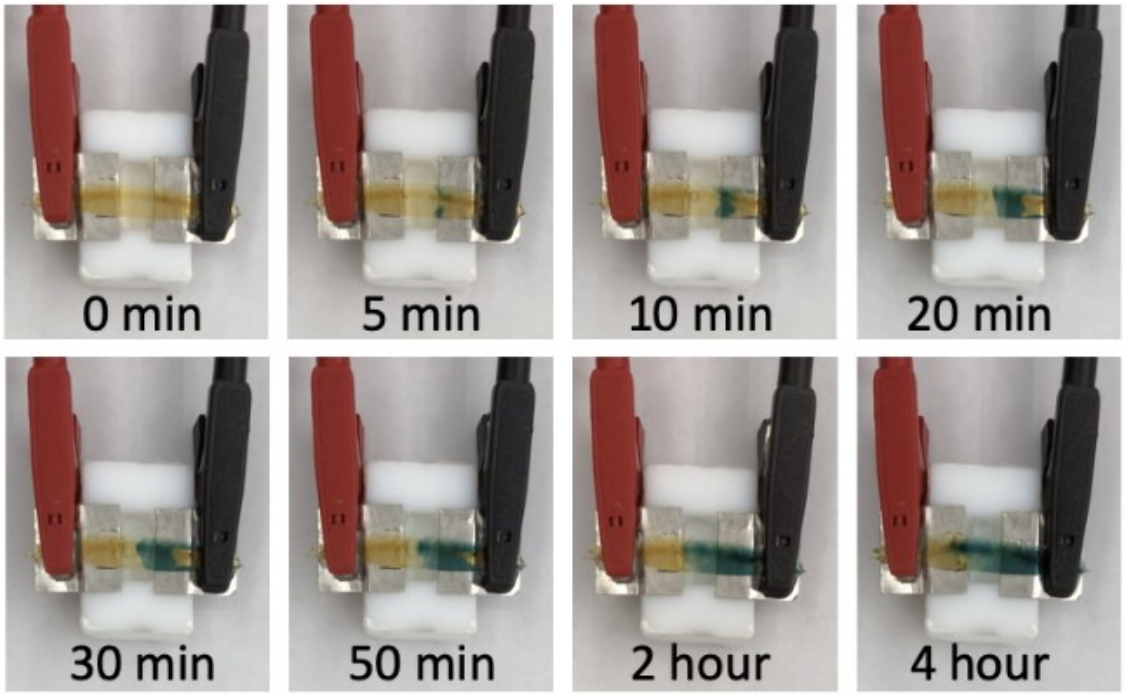

Figure 4-11. Color evolution of HMT-PMBI membrane containing 0.2 wt% thymolphthalein during current-driven water electrolysis. The blue area indicates areas of higher pH due to the production of hydroxide ions at the cathode. The anode remains at lower pH. Video provided in the SI (Video S1). Adapted from ref[51]

In order to investigate the effect of the indicator on the anionic conductivity of the AEM, a modified conductivity measurement protocol was developed that was different to that recently reported by Ziv *et al*.[104] In our method, the conductivity was monitored with electrolysis under potentiostatic control rather than galvanostatic control. The potentiostatic method enabled the membrane conductivity to reach steady state in 5 h rather than 30 h (galvanostaic mode). The details of the conductivity measurements are as follows.

Pristine HMT-PMBI membranes in air-equilibrated mixed carbonate form possessed a conductivity of 9.3 mS cm^{-1} at 40°C and 90% RH (relative humidity). Similarly, membranes containing 0.1 wt% and 0.2 wt% thymolphthalein possessed higher conductivities of 28.2 mS cm^{-1} and 33.0 mS cm^{-1}, respectively. The conductivity of the indicator/membrane composite membranes are slightly higher prior to self-purging with hydroxide. We note that the membranes containing indicator contain a higher water content prior to conductivity measurement (33 wt% and 38 wt% without and with indicator (0.2 wt%), respectively), as measured by dynamic vapor sorption (Surface Measurement Systems Ltd) at 40°C and 90% RH.

After 90 mins of equilibration at 40°C and 90% RH, 1.75V was applied across the membrane to generate OH^- at the cathode. A gradual increase in membrane conductivity was observed as shown in Figure 4-13, consistent with Dekel et al's previous report[104], and is explained as being due to an increase in hydroxide content within the membrane. The maximum conductivity of pristine HMT-PMBI at steady state is found to be 98.4 mS cm^{-1} which is similar to the 103 mS cm^{-1} previously reported.[104] There are observed differences in the absolute conductivities measured between samples, which we speculate are due to variations in membrane morphologies as a result of inconsistencies in the rates of solvent evaporation during membrane solution casting.

Under the potentiostatic mode employed in this work, steady state was reached after 5 hours compared to 30 hours under galvanostatic mode. The decrease in time to reach steady state via a potentiometric hold occurred because the current obtained during operation using potentiostatic mode gradually increased from 100 μA, to 800 μA (Figure 4-12) compared to a constant 100 μA using galvanostatic mode.[7] For the thymolphthalein-containing HMT-PMBI membranes, the observed current increased up to maximum of 1200 μA and 1600 μA for 0.1 wt% and 0.2 wt% indicator, respectively.

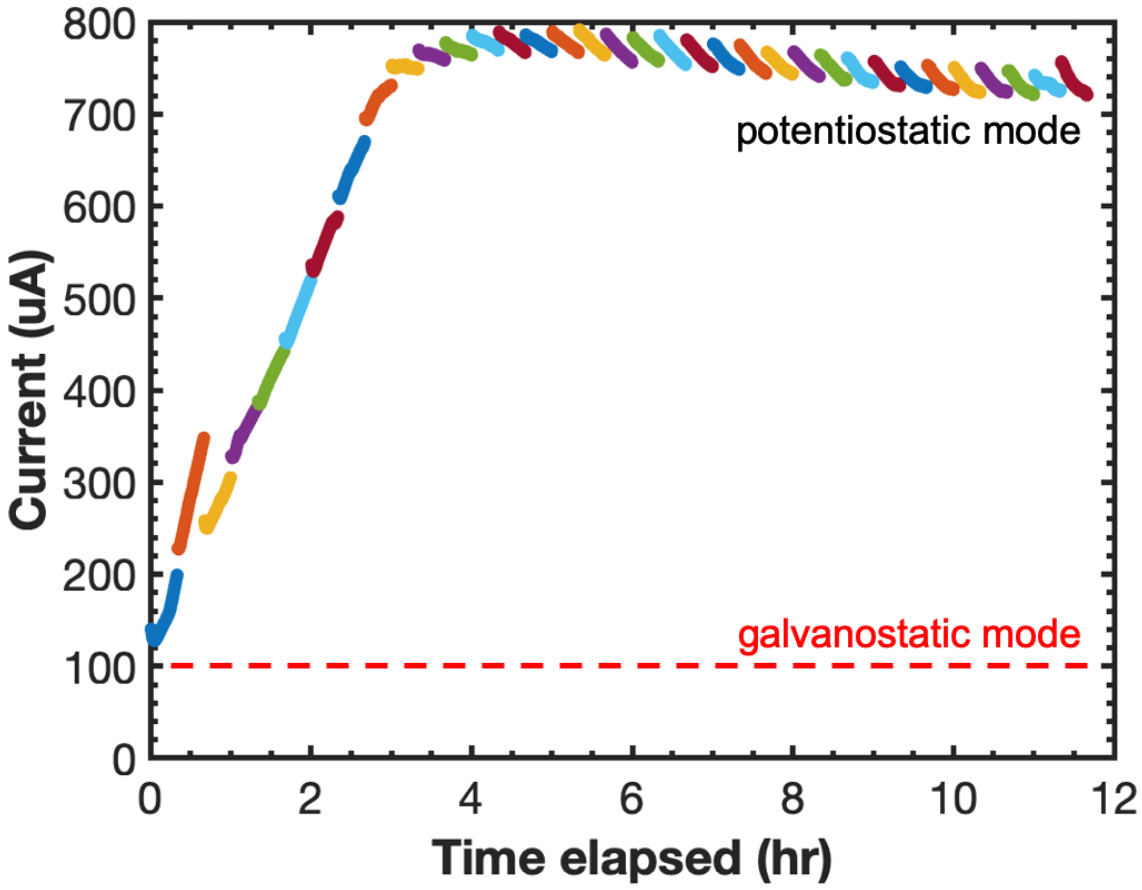

Figure 4-12. Increased current using potentiostatically-controlled mode for water electrolysis. Membrane is pristine HMT-PMBI, and the potential was kept at 1.75 V throughout the entire experiment. Each different color represents a new 20 min potential hold of 1.75V. Adapted from ref[51]

The conductivity of thymolphthalein containing HMT-PMBI membranes also increased during potentiostatically-controlled electrolysis, and faster than galvanostatically-controlled, exhibiting maximum conductivities of 122.8 mS cm^{-1} and 144.1 mS cm^{-1} for 0.1 wt% and 0.2 wt% thymolphthalein, respectively, and steady state values of 92.2, 97.6 and 111.7 mS cm^{-1} for pristine HMT-PMBI, co-cast HMT-PMBI membranes with 0.1 wt%, and 0.2 wt% thymolphthalein, respectively.

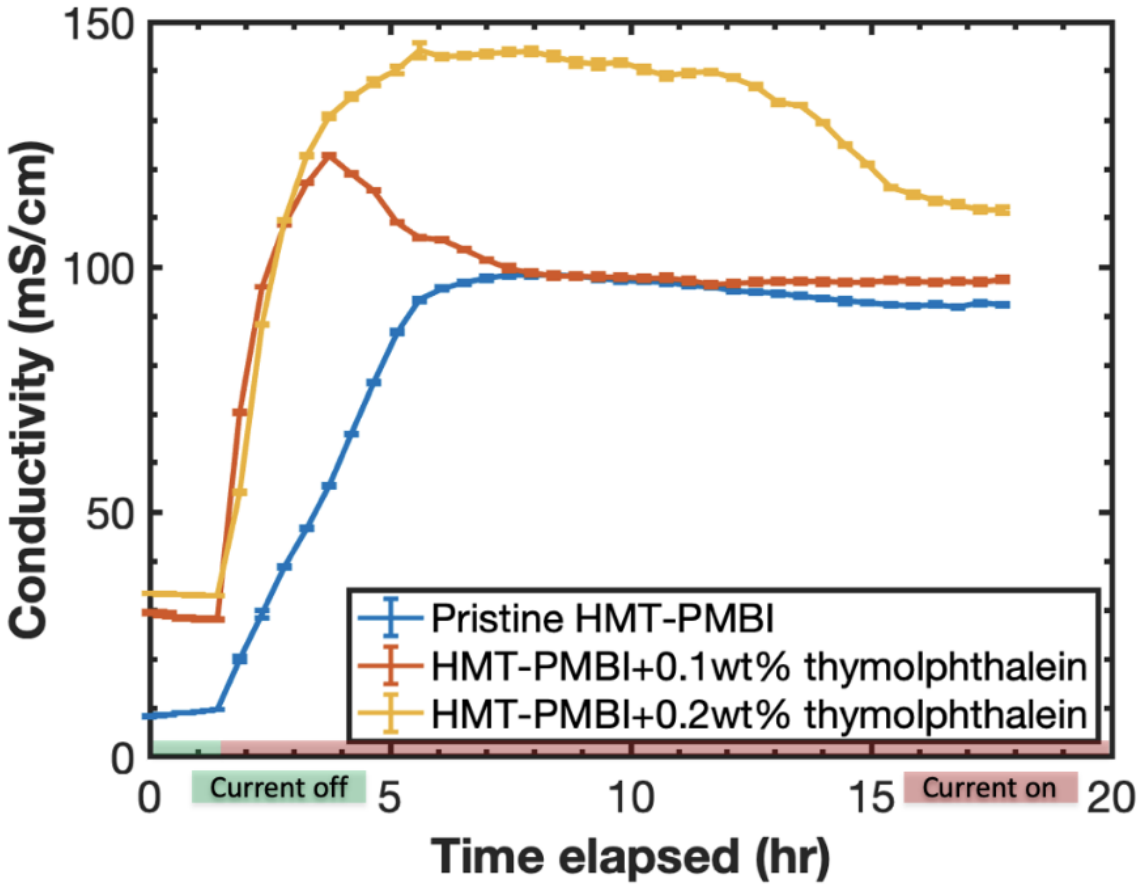

Figure 4-13. Ionic conductivity of membranes before and during electrolysis by applying 1.75V under 90% RH and 40 ^{0}C. Blue: pristine HMT-PMBI. Red curve HMT-PMBI + 0.1 wt% thymolphthalein. Yellow: HMT-PMBI + 0.2 wt% thymolphthalein. Green bar: current off. Pink bar: voltage/current on. Adapted from ref[51]

A UV-vis spectrum of HMT-PMBI + 0.1 wt% thymolphthalein before the potential treatment is shown in (Figure 4-14**,** blue curve). After the membrane had reached steady state conductivity following electrolytic hydroxide formation a new absorption peak was observed at 610 nm (Figure 4-14**,** red curve) quantitatively providing evidence of the membrane color changing to blue. The blue colour gradually faded upon exposure to ambient air (containing 400 ppm CO_2) and the peak at 610 nm correspondingly diminished (Figure 4-14, yellow curve). The reported absorption maximum of thymolphthalein dianion is 595 nm, where the absorbance peak of HMT-PMBI/thymolphthalein membrane is around 610 nm. The blue shift in UV-vis spectra might be caused by the ionic interaction between the positively charged imidazolium cations of HMT-PMBI and the negatively charged thymolphthalein dianions.[105]

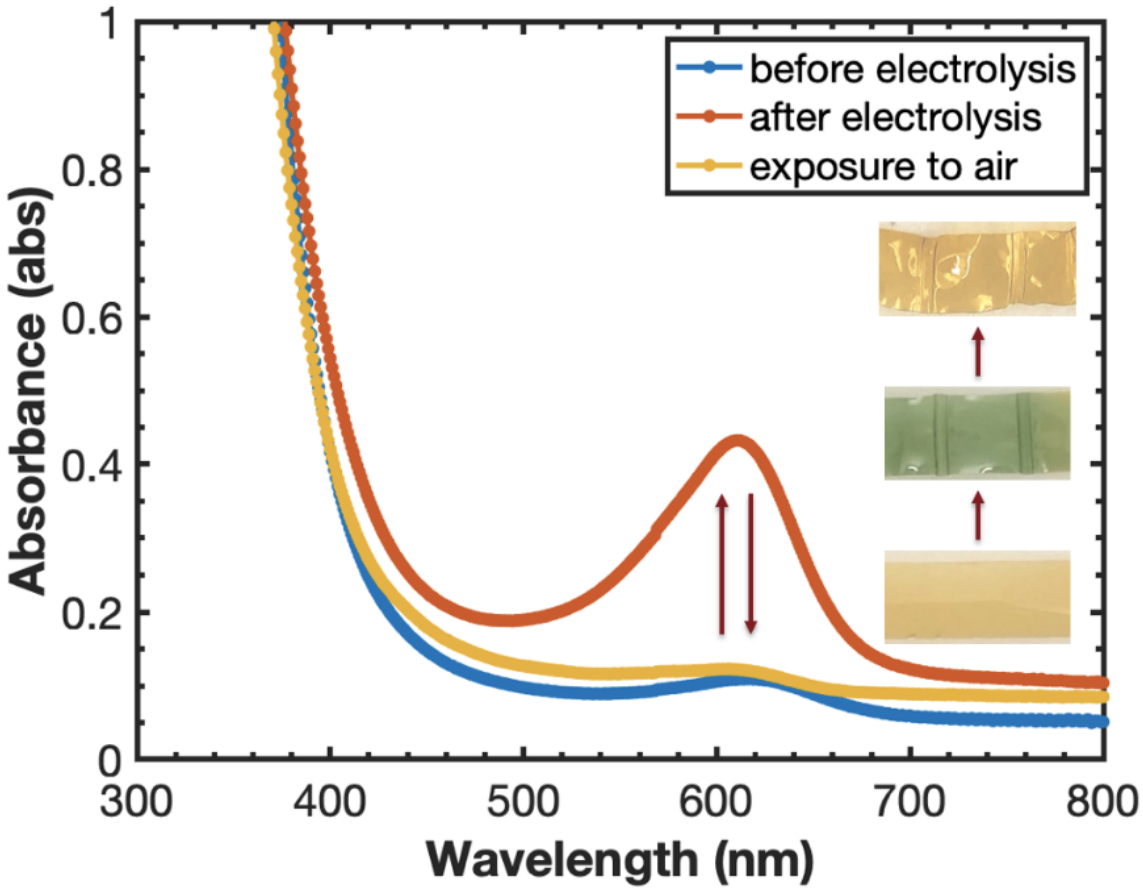

Figure 4-14. UV-vis spectra of initial HMT-PMBI membrane + 0.1% thymolphthalein in its mixed carbonate/bicarbonate form, after electrolytic purging with hydroxide ions, and after electrolysis and exposure to air (400 ppm CO_2). The membranes are shown in the inset. Adapted from ref[51]

4.5. Conclusion and future work

Using the HMT-PMBI and thymolphthalein co-cocast membrane presented in this work, the nature of the anions conducted in the membrane could be deducted from the local pH. The change of color from yellow to blue/green reflects the increase of the local pH in the membrane. Combining the evidence of the increased pH and elevated conductivity, one could confidently conclude the change of the counter ion in the membrane changed from bicarbonate to hydroxide using the ion flushing method predicted from the physiochemical model. Therefore, the method of measuring OH^- conductivity of an anion exchange membrane could be achieved by using water electrolysis to flush out the bicarbonate/carbonate counter ions.

It is herein demonstrated a proof of principle strategy of visualizing the change in hydroxide ion concentration, i.e., pH, in an anion exchange membrane. The concept may be applicable to a wide range of indicators and a wide range of AEMs if the appropriate components exhibit sufficient color contrast. Initial explorations of this work involved simply dropping pH indicator solutions onto membranes post-electrolysis, which evolved into co-casting indicators with the polymer into a cohesive membrane, as in this work. One can easily envisage scenarios wherein the indicator (or indicators) is chemically-bound to the constituent polymers or to a reinforcement material. Moreover, indicators are not restricted to those simply exhibiting a color change but might encompass fluorophores and other probes that are sensitive to local acid/hydroxide concentrations.

The so-called hydroxide ion purging process is visually demonstrated here in a simple solid-state electrolytic cell. However, one can foresee employment in other situations involving fuel cells, electrolyzers, or bipolar membrane technology either for energy conversion/storage devices or for sensor technology, e.g., CO_2 detection. Moreover, the method is not restricted to membranes; under the appropriate circumstances this strategy might be applied to monitor pH changes in ionomers in catalyst layers with appropriate detection devices.

While this report largely demonstrates local pH changes colorimetrically rather qualitatively, colorimetry can be quantified. Future work should be focused on spatially quantifying the visual changes in order to extract rates of diffusion, for example. Such studies would assist in understanding ion transport processes in ion containing polymers, films, and membranes.

An additional novelty of this work is that the conductivity measurements was performed under a potentiostatic load rather than a galvanostatic load, which, because of the increased rates of electrolysis, substantially decreases the time for the membrane to reach a steady state membrane conductivity compared to previously reported galvanostatic conditions. This enables faster measurements of membrane substrates which ultimately leads to more rapid evaluation of materials.

Chapter 5. Study of OH^- concentration in the anion exchange membrane during electrochemical reaction

This chapter contains materials reproduced with permission from the peer-reviewed article published as Fortin, P.; Khoza, T.; Cao, X.; Martinsen, S. Y.; Oyarce Barnett, A.; Holdcroft, S. High-Performance Alkaline Water Electrolysis Using Aemion™ Anion Exchange Membranes. *Journal of Power Sources* **2020**, *451*, 227814. https://doi.org/10.1016/j.jpowsour.2020.227814

This work was financially supported by Natural Sciences and Engineering Research Council of Canada (NSERC).

Individual contributions were: X.C. performed the ex-situ characterizations and wrote the experimental section for the OH^- condcutvity in each study. P.F; K.T., M.S.Y., O.B.A. performed the in-situ water electrolysis test and wrote the rest of the first paper. Li, W. synthesized the polyarylimidazolium ionenes, O.P. characterized the water uptake properties wrote the rest of the second paper. S.H. advised supervised and edited both works.

5.1. Introduction

Global power demand has doubled in the last two decades, primarily driven by population growth, industrialization, and urbanization.[110,111] An unprecedented expansion of fossil fuel combustion has resulted in an increase in greenhouse gases (GHG) and air pollutant emissions.[112] If emissions continue on this trajectory, the International Energy Agency (IEA) predicted this would lead to a temperature rise of 2.7 °C by 2100.[113] Hydrogen stands out among the search for fossil fuel alternatives due to their high gravimetric energy density (141.86 MJ/kg). The implementation of hydrogen as a fuel can be addressed with electrochemical devices that utilize an anion exchange membrane, such as fuel cells, water electrolysis.

Fuel cells convert the chemical energy stored in hydrogen fuels directly to electricity, compared to well-established internal combustion engine which converts the chemical energy stored in fossil fuels to heat, then mechanical energy, and finally electricity.[58] Thus, fuel cells offer significantly high efficiency and much lower GHG emission and are regarded as a most promising energy conversion strategies for sustainable energy development. The reverse of fuel cell technologies is the water electrolysis, which produces hydrogen fuels via electrolytic splitting of water. Consequently, the fuel cell and water electrolysis techniques constitute a low carbon energy solution as an alternative to fossil fuels. CO_2 electrolysis uses the abundant carbon source (CO_2) to produce valuable chemicals like formic acid, carbon monoxide, methanol, methane, ethylene, ethanol, and acetate via electrochemical reduction of C-O bond.[5]

All the above electrochemical devices consist of a cathode, an anode and an electrolyte which separates the two electrodes. Using the ion exchange membrane allows the use of zero-gap cell configuration, which provides a short pathway for the ions to transport from one electrode to the other and minimizes ohmic loss due to the electrolyte. Anion exchange membrane stands out among other electrolyte materials, because the basic environment allows use of Pt-free metal catalyst[114] and non-fluorinated polymer[115], which reduces manufacture and environmental cost. The anions commonly present in an electrochemical system includes hydroxide (OH^-), bicarbonate (HCO_3^-) and carbonate (CO_3^{2-}) as a result of the carbonation reaction (Equation 5-1 and Equation 5-2)[116].

Equation 5-1 $$CO_2 + OH^- \rightleftarrows HCO_3^-$$

Equation 5-2 $$HCO_3^- + OH^- \rightleftarrows CO_3^{2-} + H_2O$$

The concentration of charge carriers in the electrolyte is known to affect the electrochemical reaction and catalytic activity for H_2 fuel cell and CO_2 reduction electrolysers.[93,117–120] Identifying the type of anion being transported in the anion exchange membrane is important for a few reasons. Firstly, the ion conductivity relies on the mobility of the ions being transported. The ionic mobility for OH^- is 2.7 times and 4.5 times higher than CO_3^{2-} and HCO_3^- in aqueous solutions at 25°C, respectively.[93] Therefore, significant losses of efficiency of an electrochemical device is predicted when the OH^- ion are replaced by the larger and less mobile CO_3^{2-} and HCO_3^- anions. Secondly, different anions are transported through the anion exchange membrane via various mechanisms. Like CO_3^{2-} and HCO_3^- anions, the OH^- are transported through the conduction mechanism driven by electrical potential gradient, the diffusion mechanism driven by concentration gradient, and the convection mechanism driven by pressure gradient.[121] In addition, the OH^- are transported through the Grotthuss (proton hopping) mechanism via breaking and forming O-H bonds with the water molecules in the hydrated ion conducting channels.[121] Thirdly, the electrochemical reaction occurred at each electrodes are different when various anions are fed into the electrodes. In an H_2 fuel cell, only reactions described by Equation 5-3 take place at the anode when OH^- ions are transported, while additional oxidation reactions (Equation 5-4 and Equation 5-5) occur when CO_3^{2-} and HCO_3^- ions are transported.[120] In a CO_2 electrolyser, it has been observed that the charge carrier can be oxidized to CO_2 and or O_2 as shown in Equation 5-6 and Equation 5-7.

Equation 5-3 $$2H_2 + 4OH^- \rightleftarrows 4H_2O + 4e^-$$

Equation 5-4 $$2H_2 + 2CO_3^{2-} \rightleftarrows 2H_2O + 2CO_2 + 4e^-$$

Equation 5-5 $$2H_2 + 4CO_3^{2-} \rightleftarrows 4H_2O + 4CO_2 + 4e^-$$

Equation 5-6 $$2OH^- \rightleftarrows O_2 + 2H^+ + 4e^-$$

Equation 5-7 $$2CO_3^{2-} \rightleftarrows 2CO_2 + O_2 + 4e^-$$

The concentration of protons shifts the acid-base equilibrium of HCO_3^{2-}, CO_3^{2-} and OH^- as shown in Equation 5-8, Equation 5-9 and Equation 5-10. Thus, the concentration of the HCO_3^-, CO_3^{2-} and OH^- in an anion exchange membrane can be interpreted by the local pH in the membrane. To illustrate the change of anions (HCO_3^-, CO_3^{2-}, and OH^-) in an anion exchange membrane, an acid-base pH indicator was introduced to the polymer matrix during casting. As the concentration of proton shifts the acid-base equilibrium, the pH indicator shifts between its protonated and deprotonated form. Thus, the nature of charge carrier in the membrane can be measured by spectrophotometry.

Equation 5-8 $\mathrm{H_2CO_{3\,(aq)}} \rightleftarrows \mathrm{H^+_{(aq)}} + \mathrm{HCO^-_{3\,(aq)}}$

Equation 5-9 $\mathrm{HCO^-_{3\,(aq)}} \rightleftarrows \mathrm{H^+_{(aq)}} + \mathrm{CO^{2-}_{3\,(aq)}}$

Equation 5-10 $\mathrm{H_2O_{\,(l)}} \rightleftarrows \mathrm{H^+_{(aq)}} + \mathrm{OH^-_{(aq)}}$

Research has shown that the anion composition is different across the membrane because of the carbonate reactions.[60,75,119,122,123] Of particular relevance to this study are the findings by Krewer and coworkers showing an increase of 25% OH^- across a 28 μm thick membrane simulated in a single cell fuel cell with water-saturated hydrogen at anode and ambient air containing 400 ppm CO_2 at cathode.[124] In addition, the OH^- concentration increased over 100 mM across the 50 μm thick membrane simulated in CO_2 reduction.[125] Currently, the experimental approach of studying the anion composition in an electrochemical system is through in-operando Raman spectroscopy using a modified electrolyzer or fuel cell with a sapphire window.[122] However, this method requires special designed cell and does not separate the spectroscopic response of the membrane from the catalyst layer. In this study, a method of studying the anion composition on a bare membrane by using a pH indicator doped membrane is proposed.

The reversibility and robustness of entrapping a pH indicator in an imidazolium-based membrane was demonstrated by Guo et al, where sulfonated anionic dyes remained ionically bonded to the 1-butyl-3-vinylimidazolium cations over 100 reversible cycles of protonation and deprotonation without leaching into aqueous solution.[126] The application of an anion exchange membrane with pH indicator in a electrochemical

process was demonstrated by Cao et al, where the change of HCO_3^- to OH^- through water electrolysis was visualized using a hexamethyl-p-terphenyl polybenzimidazolium membrane with thymolphthalein dye.[51] It is known that the pH affects the catalytic activity and selectivity of CO_2 reduction reaction.[117–119] An pH indicator doped anion exchange membrane that differentiates between CO_3^{2-} and OH^- as the charge carrier was not available. Herein, the pH change in a series pH indicator doped imidazolium-based membranes is studied to understand the conversion between the anions (HCO_3^-/CO_3^{2-}/OH^-).

5.2. Experimental

5.2.1. Materials and chemicals:

The anion exchange membrane used in this work includes hexamethyl-p-terphenyl polybenzimidazolium (HMT-PMBI), the aniline blue indicator doped HMT-PMBI, and the acid fuchsin indicator doped HMT-PMBI. The synthesis and characterization of HMT-PMBI was reported elsewhere. [55] HMT-PMBI is a polymer consisting of a mixture of three distinct units as shown in Figure 5-1, monomer unit “a” represents a 50% degree of methylation (dm) of the N atoms, monomer unit “b” represents 75% dm, and monomer unit “c” represents 100% dm. The exact degree of methylation of the pristine HMT-PMBI was calculated using the NMR spectroscopic analysis method.[127] The pH indicators utilized, aniline blue and acid fuchsin, are shown Figure 5-2, and their characteristics are listed in Table 5-2.

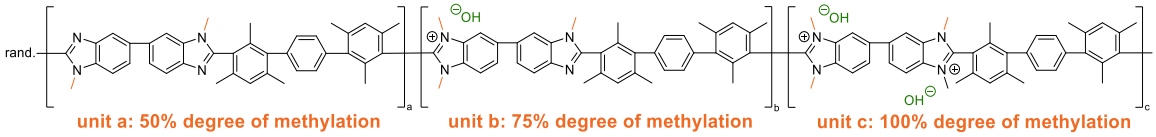

Figure 5-1. Chemical structure of 50-100% dm HMT-PMBI (I-), where dm represents the degree of methylation of the N atoms.

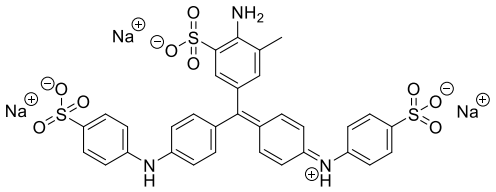

Aniline Blue
pH range 11.0-13.0

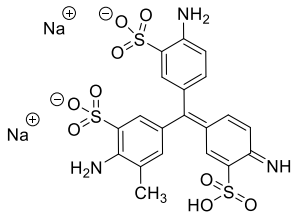

Acid Fuchsin
pH range 12.0-14.0

Figure 5-2. Chemical structure of of the pH indicators: aniline blue (top) and acid fuchsin (bottom)

The pH-indicating anion exchange membrane was prepared by solvent casting with a mixture of the pH-indicator (e.g. acid fuchsin) and the anion exchange membrane (HMT-PMBI). A solution of 7.5% w/w polymer in dimethyl sulfoxide (DMSO) was vacuum filtered through a borosilicate glass fiber at room temperature, coated onto a leveled glass plate using the casting table (K202 Control Coaster) and an adjustable doctor blade (RK Print Coat Instruments Ltd®). After evaporating the DMSO at 80°C for 12 hours, the resulting membrane was peeled off from the glass by immersion in ultra-pure water and dried in a vacuum oven.

Reagent grade KCl, $KHCO_3$, K_2CO_3, KOH, DMSO, deuterated DMSO, purchased from Sigma Aldrich® and Fisher Scientific®, were used as received. All aqueous solution was prepared using ultra-pure water purified by a Milli-Q system (SYNSVHFWW, Synergy® UV Water Purification System). The thickness of the membranes was measured using a Mitutoyo® digital micrometer. The area of the membranes was measured using an Epson® PerfectionV39 scanner at 1600 dpi resolution, and the resulting images were analyzed using ImageJ software. ^{1}H NMR spectroscopic characterizations were performed on a Bruker Avance-500 instrument. The pH of aqueous solutions was measured using Metrohm® 781pH/ion Meter. UV-vis absorption spectra were measured using the Shimadzu® UV-3600 Plus

Spectrophotometer. Electrochemical measurements were performed using Solartron Analytical SI 1287 Potentiostat® and Solartron Analytical 1260 Impedance Analyzer®.

5.2.2. Water sorption properties: water uptake (WU) and volumetric swelling (VS) and hydration number (λ)

The water content of the membranes was determined by measuring the mass and dimensional changes of their fully hydrated and dry states. Small pieces (2 x 3 cm) samples were cut for the water content measurements. The hydrated state was achieved by immersing the membranes in ultra-pure water for at least 24 hours. The thickness (t_{wet}), hydrated area (A_{wet}) and hydrated mass (m_{wet}) were measured on the fully hydrated membranes after removing any surface-bound water with Kimwipe®. To achieve the fully dried state, membrane samples were then sandwiched between filter papers and dried under vacuum oven at 80°C for at least 16 hours. The dry thickness (t_{dry}), dry area (A_{dry}) and dry mass (m_{dry}) were measured on the oven dried membranes.

The water uptake (WU, %) was calculated using the mass change between the fully hydrated and dry states using Equation 5-11. The dimensional swelling in each dimension ($S_{x,y,z}$, %) and volumetric swelling (VS, %) were calculated using the dimensional changes of the fully hydrated and dry states using Equation 5-12 and Equation 5-13 where the $S_{(x,y,z)}$ represents the x,y-directions (length and width) and z-direction (thickness) of the membrane in either fully hydrated $_{(wet)}$ or dry $_{(dry)}$ states.

Equation 5-11 $$\mathrm{WU}(\%) = \frac{\mathrm{m_{wet} - m_{dry}}}{\mathrm{m_{dry}}} \times 100\%$$

Equation 5-12 $$\mathrm{S_{x,y,z}}(\%) = \frac{\mathrm{S_{(x,y,z)wet} - S_{(x,y,z)dry}}}{\mathrm{S_{(x,y,z)dry}}} \times 100\%$$

Equation 5-13 $$\mathrm{VS}(\%) = \frac{\mathrm{t_{wet} \times A_{wet} - t_{dry} \times A_{dry}}}{\mathrm{t_{dry} \times A_{dry}}} \times 100\%$$

5.2.3. Ion exchange capacity ($IEC_{th/ex}$) and anion concentration [X^-]

The ion exchange capacity (IEC, mmol/g) describes the quantity of charged groups in the membrane and can be calculated using the number of functional groups (molar equivalents, eq.) per unit mass of dry membrane (g)[63]. The theoretical IEC (IEC_{th}) of the membrane in their X^- form was determined by NMR spectroscopic

analysis using Equation 5-14, where the dm represents the degree of methylation, M_{dm} represents the mass of the HMT-PMBI of certain dm%. M_{dm} can be calculated using the mass of the 100% dm HMT-PMBI repeating unit (for OH^- counter-ion: M_{R100}=636.82 g/repeating unit) and the molecular weight of the 50% dm HMT-PMBI repeating unit (for OH^- counter-ion: M_{R500}= 572.74 g/repeating unit). As shown in the chemical structure (Figure 5-1), there are 2 counter ions (X^-) in one 100%dm repeating unit; therefore, the equivalent counter ions (X^-) can be calculated using the amount of the 100%dm repeating unit in the membrane which is 2(dm-0.5).

Equation 5-14

$$\mathrm{IEC_{th}}\left(\frac{\mathrm{mmol}}{\mathrm{g}}\right)=\frac{\mathrm{eq.n_{X^-}}}{\mathrm{M_{dm}}}=\frac{\frac{1000\ \mathrm{mmol}}{1\ \mathrm{mol}}\cdot\frac{2[2(\mathrm{dm}-0.5)]\mathrm{eq.\ X^-}}{1\ \mathrm{repeating\ unit}}}{\mathrm{M_{R100}}[2(\mathrm{dm}-0.50)]+\mathrm{M_{R50}}[1-2(\mathrm{dm}-0.50)]}$$

The IEC determined by NMR spectroscopic analysis is theoretical (IEC_{th}), and depends on the dissociation constant of the functional groups. The apparent ion exchange capacity (IEC_{ex}), which is the number of functional groups in the polymer structure accessible to ion exchange, may not be the total amount determined by NMR. Therefore, the apparent ion exchange capacity (IEC_{ex}) was measured experimentally by evaluating the amount of exchanged Cl^- ions using titrimetric analysis described in literature[63–66]. Prior to IEC analysis, membrane samples were converted to Cl^- form by immersing in 1 M KCl solutions twice for 24 hoursrs and washing several times with DI water for 48 hours. To ensure complete exchange of Cl^- to NO_3^- ions, membrane samples were immersed twice in 15 mL of 1 M KNO_3 solution for 24 hours. The Cl^- concentration of the exchanged solution was determined using a Cl^- ion-selective electrode (Cl^- ISE 6.0502.120, Metrohm AG®). The membranes were converted back into their Cl^- form by soaking twice in 1 M KCl for 24 hrours, washing multiple times and soaked with DI water over the course of 48 hourrs and dried under vacuum at 80°C for 24 hours. The dry weight of the membrane in its Cl^- form (m_{dry}) was measured after cooling to room temperature under vacuum. The IEC_{ex} was calculated using the Cl^- concentration ($[Cl^-]$ in ppm), the mass of the exchange solution ($m_{solution}$) and molar mass of chloride ion (M_{Cl}) using Equation 5-15**.**

Equation 5-15

$$\mathrm{IEC_{ex}}\left(\frac{\mathrm{mmol}}{\mathrm{g}}\right)=\frac{[\mathrm{Cl^-}]\cdot\mathrm{m_{solution}}}{1000\cdot\mathrm{M_{cl}}\cdot\mathrm{m_{dry}}}$$

The anion concentration ($[X^-]$) was calculated using the apparent ion exchange capacity (IEC_{ex}), the dry mass of the membrane (m_{dry}), the hydrated thickness (t_{wet}) and area (A_{wet}) using Equation 5-16.

Equation 5-16 $$[X^-] = \frac{IEC_{ex,\,X^-} \cdot m_{dry}}{t_{wet} \cdot A_{wet}}$$

5.3. Results and discussion

5.3.1. pH and concentration of $HCO_3^-/CO_3^{2-}/OH^-$ in aqueous solution

The equilibrium of HCO_3^-, CO_3^{2-} and OH^- in an aqueous solution can be classified as an equilibrium in a closed system (without atmospheric CO_2) or equilibrium in an open system (with atmospheric CO_2). For a closed system, the equilibrium includes the dissociation of carbonic acid (Equation 5-17 and Equation 5-18) and water (Equation 5-19), the mass balance of carbon (Equation 5-20), and the charge balance (Equation 5-21). For an open system, the equilibrium involves an addition equilibrium with atmospheric CO_2 (Equation 5-22). The equilibrium constant for Equation 5-17 and Equation 5-18 are $10^{-6.35}$ and $10^{-10.33}$ at STP (standard temperature and pressure). The Henry's law constant of CO_2 gas in water at 298.15K is $10^{-1.47}$ M atm^{-1} in Equation 5-22.

Equation 5-17 $$H_2CO_{3\,(aq)} \rightleftarrows H^+_{(aq)} + HCO^-_{3\,(aq)}$$

Equation 5-18 $$HCO^-_{3\,(aq)} \rightleftarrows H^+_{(aq)} + CO^{2-}_{3\,(aq)}$$

Equation 5-19 $$H_2O_{\,(l)} \rightleftarrows H^+_{(aq)} + OH^-_{(aq)}$$

Equation 5-20 $$[C]_{total} = [CO_3^{2-}] + [HCO_3^-] + [CO_2]$$

Equation 5-21 $$[H^+] = [HCO_3^-] + 2[CO_3^{2-}] + [OH^-]$$

Equation 5-22 $$CO_{2\,(g)} + H_2O_{\,(l)} \rightleftarrows H_2CO_{3\,(aq)}$$

To understand the anion composition at various pH, the composition of dissolved CO_2, HCO_3^-, CO_3^{2-} pH were calculated as follows. The fraction of dissolved CO_2 (H_2CO_3), HCO_3^-, and CO_3^{2-} is defined by using their concentration divided by the

total concentration of the three species as shown in Equation 5-23, Equation 5-24 and Equation 5-25.

Equation 5-23 $$f_{H_2CO_3} = \frac{[H_2CO_3]}{[H_2CO_3]+[HCO_3^-]+[CO_3^{2-}]}$$

Equation 5-24 $$f_{HCO_3^-} = \frac{[HCO_3^-]}{[H_2CO_3]+[HCO_3^-]+[CO_3^{2-}]}$$

Equation 5-25 $$f_{CO_3^{2-}} = \frac{[CO_3^{2-}]}{[H_2CO_3]+[HCO_3^-]+[CO_3^{2-}]}$$

Dividing both the denominator and numerator by $[HCO_3^-]$ in Equation 5-23, Equation 5-24 and Equation 5-25, the fraction of three species can be expressed as Equation 5-26, Equation 5-27 and Equation 5-28.

Equation 5-26 $$f_{H_2CO_3} = \frac{\frac{[H_2CO_3]}{[HCO_3^-]}}{\frac{[H_2CO_3]}{[HCO_3^-]}+1+\frac{[CO_3^{2-}]}{[HCO_3^-]}}$$

Equation 5-27 $$f_{HCO_3^-} = \frac{1}{\frac{[H_2CO_3]}{[HCO_3^-]}+1+\frac{[CO_3^{2-}]}{[HCO_3^-]}}$$

Equation 5-28 $$f_{CO_3^{2-}} = \frac{\frac{[CO_3^{2-}]}{[HCO_3^-]}}{\frac{[H_2CO_3]}{[HCO_3^-]}+1+\frac{[CO_3^{2-}]}{[HCO_3^-]}}$$

From the dissociation of H_2CO_3 and HCO_3^{2-} (Equation 5-17 and Equation 5-18), the ratio of dissolved CO_2 and HCO_3^- and the ratio of CO_3^{2-} and HCO_3^- can be expressed using concentration of protons and the dissociation constants of carbonic acid as shown in Equation 5-29 and Equation 5-30.

Equation 5-29 $$\frac{[H_2CO_3]}{[HCO_3^-]} = \frac{[H^+]}{K_{a1}}$$

Equation 5-30 $$\frac{[CO_3^{2-}]}{[HCO_3^-]} = \frac{K_{a2}}{[H^+]}$$

By substituting the obtained ratio of dissolved CO_2 and HCO_3^- and the ratio of CO_3^{2-} and HCO_3^- (Equation 5-29 and Equation 5-30) into the anion composition expression, the fraction of dissolved CO_2 (H_2CO_3), HCO_3^-, and CO_3^{2-} is be expressed as (Equation 5-31, Equation 5-32 and Equation 5-33). Therefore, the fraction of the

dissolved CO_2, HCO_3^- and CO_3^{2-} were expressed as a function of pH (Figure 5-3 left) or concentration of OH^- (Figure 5-3 right).

Equation 5-31 $$f_{H_2CO_3} = \frac{\frac{[H^+]}{K_{a1}}}{\frac{[H^+]}{K_{a1}}+1+\frac{K_{a2}}{[H^+]}}$$

Equation 5-32 $$f_{HCO_3^-} = \frac{1}{\frac{[H^+]}{K_{a1}}+1+\frac{K_{a2}}{[H^+]}}$$

Equation 5-33 $$f_{CO_3^{2-}} = \frac{\frac{K_{a2}}{[H^+]}}{\frac{[H^+]}{K_{a1}}+1+\frac{K_{a2}}{[H^+]}}$$

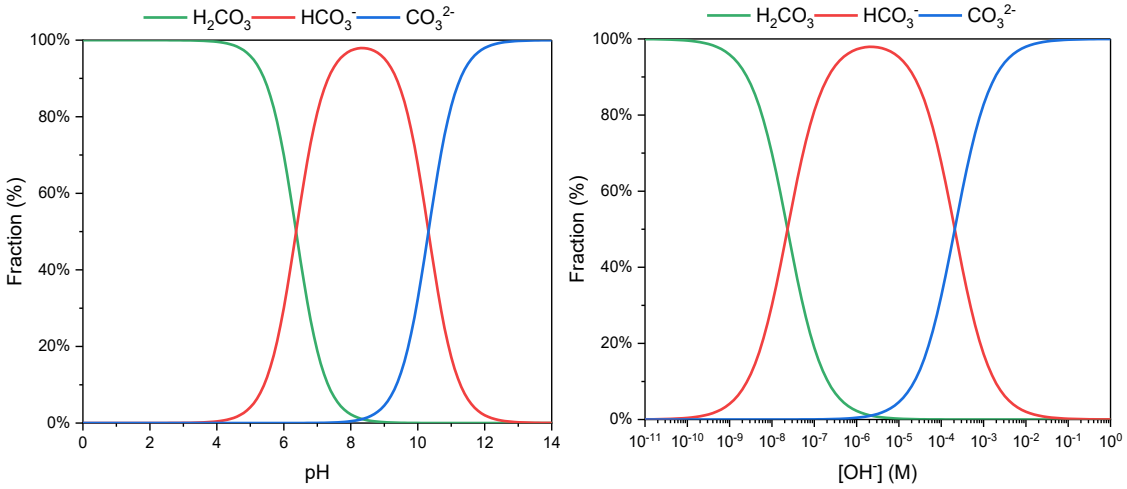

Figure 5-3. The fraction of dissolved CO_2, HCO_3^- and CO_3^{2-} as a function of pH (left) and of [OH^-] (right).

The anion concentrations of pristine 89%dm HMT-PMBI are 1.7 M for KCl, 1.57 M for $KHCO_3$, 1.69 M for K_2CO_3 and 1.51 M for KOH.[55] Therefore, concentrations of 1.5 M and 2.0 M of: KCl, $KHCO_3$, K_2CO_3, and KOH solutions were used to ensure the anion concentration in the membrane equilibrate to the aqueous solutions for the colorimetric analysis. The pH of the 1.5 M and 2.0 M of KCl, $KHCO_3$, K_2CO_3, and KOH solutions for both closed or open system were calculated using Equation 5-17 to Equation 5-22 and listed in Table 5-1. The pH of KOH gradually decreases to the same pH as $KHCO_3$ and K_2CO_3 as a result of carbonation of OH^- with atmospheric CO_2.

Table 5-1. pH of solutions of 1.5 M and 2.0 M KCl/$KHCO_3$/K_2CO_3/KOH in both closed system (excluding equilibration with atmospheric CO_2) and open system (including equilibration with atmospheric CO_2) at 25°C

	closed system		open system (with 400 ppm CO2)	
	1.5M	2.0M	1.5M	2.0M
KCl	6.92	6.91	5.59	5.6
$KHCO_3$	7.88	7.84	10.28	10.33
K_2CO_3	11.72	11.75	10.41	10.47
KOH	13.89	13.99	10.28	10.33

5.3.2. Colorimetric study of indicators cocast with HMT-PMBI to form a pH-indicating anion exchange membrane

The current study focuses on differentiating CO_3^{2-} from OH^-, which requires an indicator with a specific basic pKa value. Among commercially available indicators listed in the CRC handbook of acid-base indicators, two candidates were chosen for study: aniline blue, orange II and acid fuchsin.[108] Their pH range and color change and absorption maximum (λ_{max}) were summarized in Table 5-2.

Table 5-2. Acid-base indicators used in this study.

Indicator	Molecular Formular	Molecular Weight (g/mol)	pH Range	Color Change (acidic to basic)	λ_{max} (nm)
Aniline blue	$C_{32}H_{23}N_3Na_2O_9S_3$	737.73	11.0-13.0	Blue to violet-pink	Not reported
Acid fuchsin	$C_{20}H_{17}N_3O_9S_3Na_2$	585.55	12.0-14.0	Red to colorless	546[a]

Note: Previously reported by Bruno et al.[108]

Pristine HMT-PMBI membrane

The yellow color of pristine HMT-PMBI membrane is caused by absorbing light in the violet (380 nm - 450 nm) and ultra-violet (200 nm – 380 nm) region. As shown in **Figure3**, the dry pristine HMT-PMBI membrane shows complete absorption of light of wavelengths from 250 nm to 404 nm, where the absorbance beyond 100% is interpreted as complete absorption and no transmission.

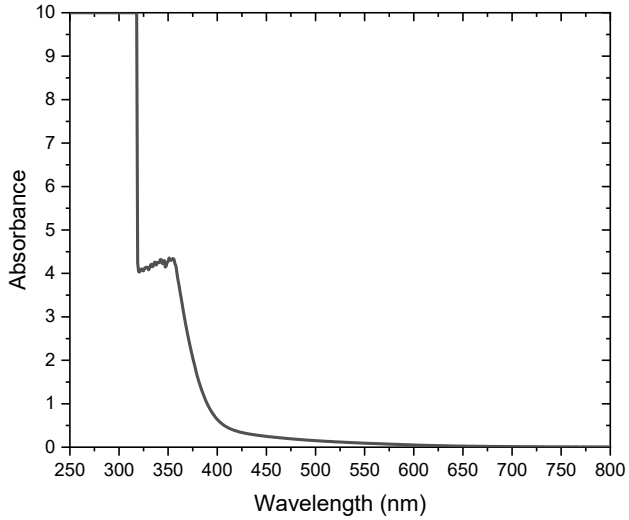

Figure 5-4. UV-vis absoprtion spectrum of dry pristine HMT-PMBI membrane sandwitched with two quartz plates, corrected with two quartz plate as blank (0% absorption or 100% transmission).

Cocast HMT-PMBI with aniline blue indicator

A series of concentration of aniline blue indicator were co-cast with HMT-PMBI to prepare the co-cast color sensitive membrane as shown in Table 5-3. The structure of aniline blue in its protonated and deprotonated form is shown in Figure 5-5.

Table 5-3. Cocast ratio of aniline blue indicator and HMT-PMBI.

Membrane label	Weight percent of aniline blue to HMT-PMBI (g/g of polymer × 100%)	Mole percent of aniline blue to HMT-PMBI (mol/mol of repeating unit × 100%)[a]
Pristine	0 wt%	0 mol%
ANB-02	0.20 wt%	0.21 mol%
ANB-04	0.40 wt%	0.42 mol%
aNB-1	0.99 wt%	1.04 mol%
ANB-3	3.09 wt%	3.27 mol%
ANB-10	10.13 wt%	10.69 mol%

[a] The mol ratio was calculated using the moles of one repeating unit of HMT-PMBI

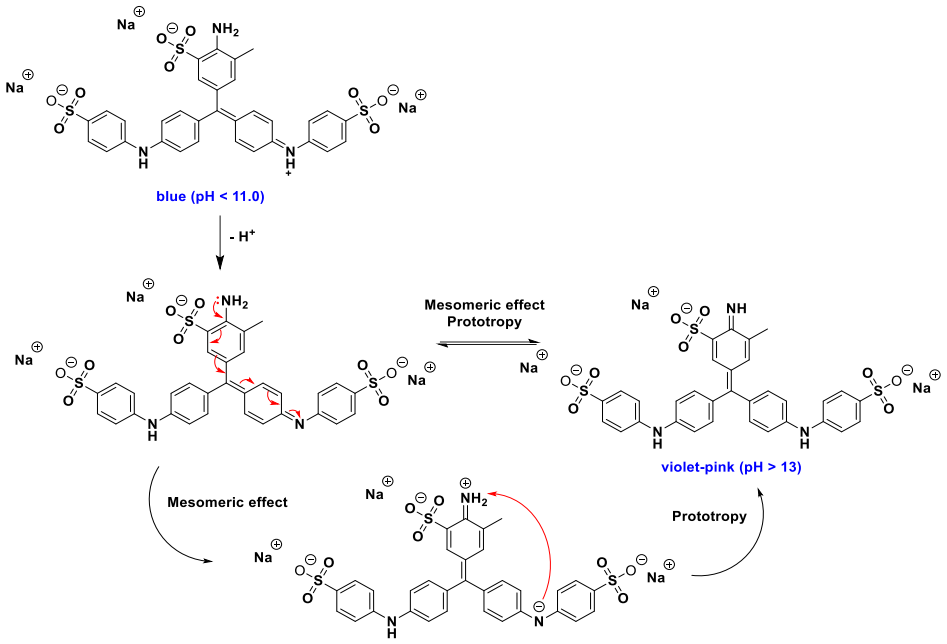

Figure 5-5. Chemical structure of aniline blue. CAS registry number 28631-66-5. Molecular weight 737.73 g/mol. pH range of 11.0-13.0. Color change of blue (pH<11.0) to violet-pink (pH>13.0).

As shown in Figure 5-6, the HMT-PMBI membranes with aniline blue indicator displays a deeper blue for high cocast concentration of 0.99 wt% to 10.13 wt% samples and a low cocast concentration resulted in blue colored membranes as shown in 0.2 wt% and 0.4 wt% samples.

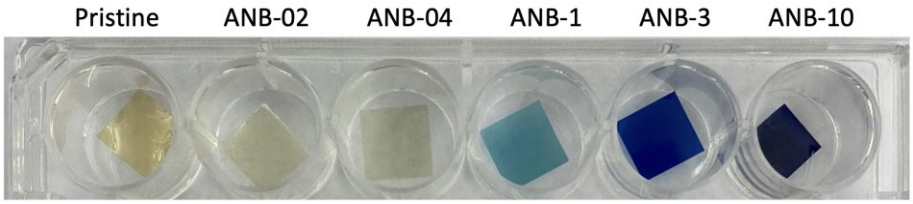

Figure 5-6. Color of cocast membrane of HMT-PMBI with aniline blue indicator. The cocast concentration increases from left to right: pristine 86%dm HMT-PMBI (column 1), co-cast with 0.20 wt% (0.21 mol%) aniline blue (column 2), co-cast with 0.40 wt% (0.42 mol%) anilne blue (column 3), co-cast with 0.99 wt% (1.04 mol%) aniline blue (column 4), co-cast with 3.09 wt% (3.27 mol%) aniline blue (column 5), co-cast with 10.13 wt% (10.69 mol%) aniline blue (column 6).

After adding water, 1.002 M $NaHCO_3$, in 1.001M Na_2CO_3 and in 1.004M NaOH solutions, co-cast HMT-PMBI with aniline blue indicator membranes changed to red color in both Na_2CO_3 and NaOH solutions as shown in Figure 5-7 (left), regardless of

the cocast concentration ratio between the HMT-PMBI polymer and aniline blue indicator. Because the cocast membrane displayed the same color in both Na_2CO_3 and NaOH solutions, the indicates aniline blue indicator cocast with HMT-PMBI membranes does not distinguish CO_3^{2-} from OH^-. A controlled color test of the aniline blue indicator in water, 1.002 M $NaHCO_3$, in 1.001 M Na_2CO_3 and in 1.004 M NaOH solutions were shown in Figure 5-7 (right). The aniline blue indicator itself in aqueous solutions displayed two distinct colors in Na_2CO_3 and in NaOH solutions: a purple color was observed in Na_2CO_3 solution and a red color was observed in NaOH solution. Because the color trrend was consistent by adding 1 drop or 3 drop of the aniline blue indicator into the salt solutions, the concentration of the indicator was found to not affect the color appearance in various salt solutions. Increasing the cocast concentration aniline blue indicator also shows no affect on the color appearance of the membrane in various salt solutions.

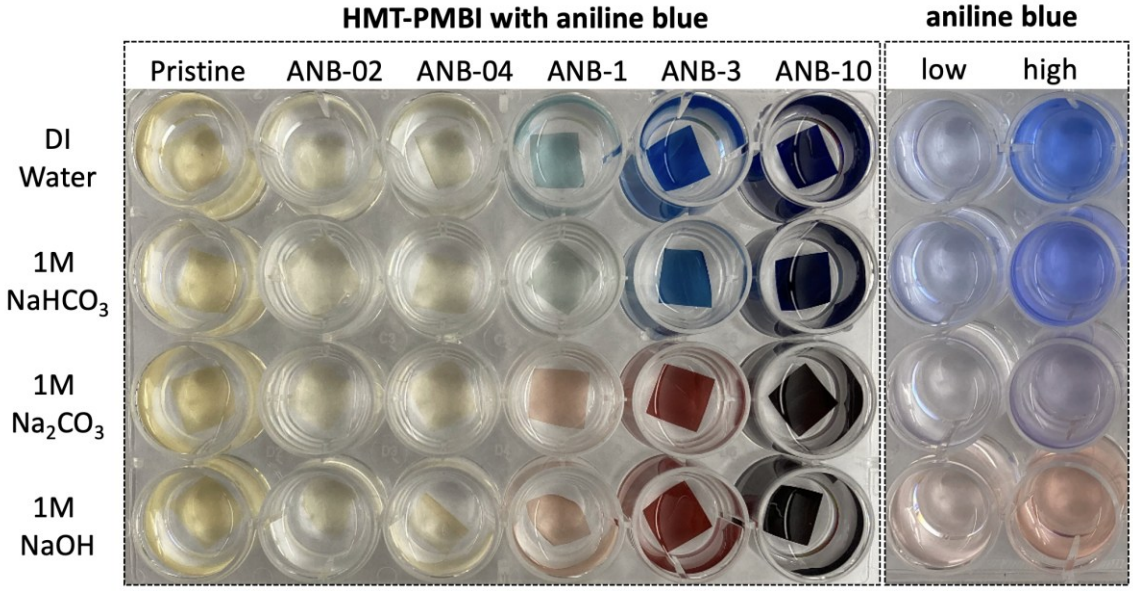

Figure 5-7. **Color test of pristine 86%dm HMT-PMBI (column 1), co-cast with 0.20 wt% (0.21 mol%) aniline blue (column 2), co-cast with 0.40 wt% (0.42 mol%) anilne blue (column 3), co-cast with 0.99 wt% (1.04 mol%) aniline blue (column 4), co-cast with 3.09 wt% (3.27 mol%) aniline blue (column 5), co-cast with 10.13 wt% (10.69 mol%) aniline blue (column 6), 2 mM aniline blue (column 7), and 4 mM aniline blue (column 8) in deionized water (18.2 MΩ) (row 1), in 1.002 M $NaHCO_3$ (row 2), in 1.001 M Na_2CO_3 (row 3) and in 1.004 M NaOH (row 4) at room temperature.**

The UV-vis absorption spectrum was obtained on both the aniline blue indicator itself and the cocast HMT-PMBI with aniline blue to investigate the color of aniline blue indicator in solution and in the membrane.

As shown in Figure 5-8, the UV-vis absorption spectrum of 3 drops of aniline blue indicator shows a blue shifting of the absorption maximum from 598 nm to 584 nm to 577 nm to 489 nm as the pH of the salt solution was increased from DI water to 1 M $NaHCO_3$ to 1 M Na_2CO_3 to 1 M NaOH. The absorption maximum of aniline blue indicator in DI water (598 nm) lies in the range of orange (590 nm to 620 nm). Absorption of orange light indicates a perceived blue color as the complementary color of orange is blue. The absorption maximum of the aniline blue indicator in 1 M $NaHCO_3$ (584 nm) and in 1 M Na_2CO_3 (577 nm) lies in the range of yellow (570 nm to 590 nm), which corelates the observed purple color of the solution in Figure 5-7. The absorption maximum of the aniline blue indicator shifted to lower wavelength in 1 M NaOH (489 nm), which lies in the range of blue (450 nm to 495 nm). The complementary color of blue is orange, which explains the orange color of aniline blue indicator in 1 M NaOH solutions.

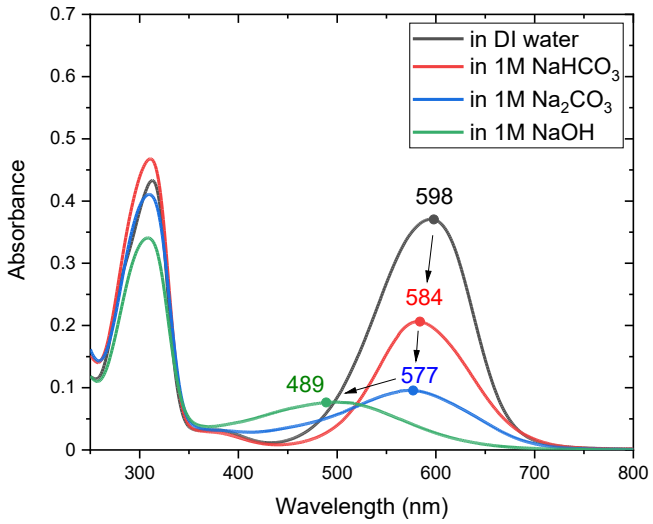

Figure 5-8. Absorption spectrum obtained by adding 3 drops of aniline blue indicator bulk solution to a standard 1 cm path length cuvette filled with DI water, 1 M $NaHCO_3$, 1 M Na_2CO_3 and 1 M NaOH. The absorption maximum shits to lower wavelength as pH increases.

In contrast, the UV-vis absorption spectrum of cocast HMT-PMBI with aniline blue indicator membrane shown in Figure 5-9 does not show the same shift in the absorption maximum. HMT-PMBI cocast with 3.09 wt% aniline blue membrane shows

an absorption maximum of 604 nm in DI water and 597 nm in 1M $NaHCO_3$ which are both orange range. The absorption maximum of HMT-PMBI cocast with aniline blue membrane in 1M Na_2CO_3 and 1M NaOH are the same (521 nm and 523 nm). Because the cocast aniline and HMT-PMBI membrane absorbs green light in both 1M Na_2CO_3 and 1M NaOH, no color difference was observed as shown in Figure 5-7.

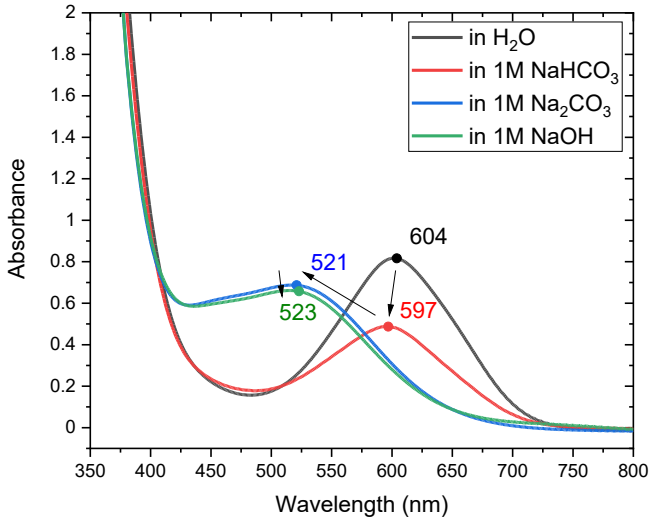

Figure 5-9. Absorption spectrum for the HMT-PMBI cocast with 3.09 wt% aniline blue membranes in DI water, 1 M $NaHCO_3$, 1 M Na_2CO_3 and 1 M NaOH.

The observed color change could be explained as the wavelength shift in the absorption spectrum, resulting from change of conjugation in the chemical structure of aniline blue indicator as shown in Figure 5-5.

As observed in Figure 5-7, the change in cocast concentration of aniline blue indicator in HMT-PMBI does not change the color behavior. The difference of the color trend observed between the aniline blue indicator itself in solution and the anline blue cocast HMT-PMBI membrane in solution was likely due to an increased local concentration of anions in the membrane phase. Therefore, a pH indicator with higher pH range was investigated next.

HMT-PMBI membranes cocast with acid fuchsin indicator

HMT-PMBI were prepared with a series of concentrations of acid fuchsin indicator as shown in Table 5-4. The structure of the acid fuchsin in its protonated and deprotonated form is shown in Figure 5-10.

Table 5-4. HMT-PMBI membranes cocast with acid fuchsin indicator.

Membrane label	Weight percent of aniline blue to HMT-PMBI (g/g of polymer × 100%)	Mole percent of aniline blue to HMT-PMBI (mol/mol of repeating unit × 100%)[a]
Pristine	0 wt%	0 mol%
2 wt%	1.75 wt%	2.32 mol%
4 wt%	3.99 wt%	5.32 mol%

[a] The mol ratio was calculated using the moles of one repeating unit of HMT-PMBI.

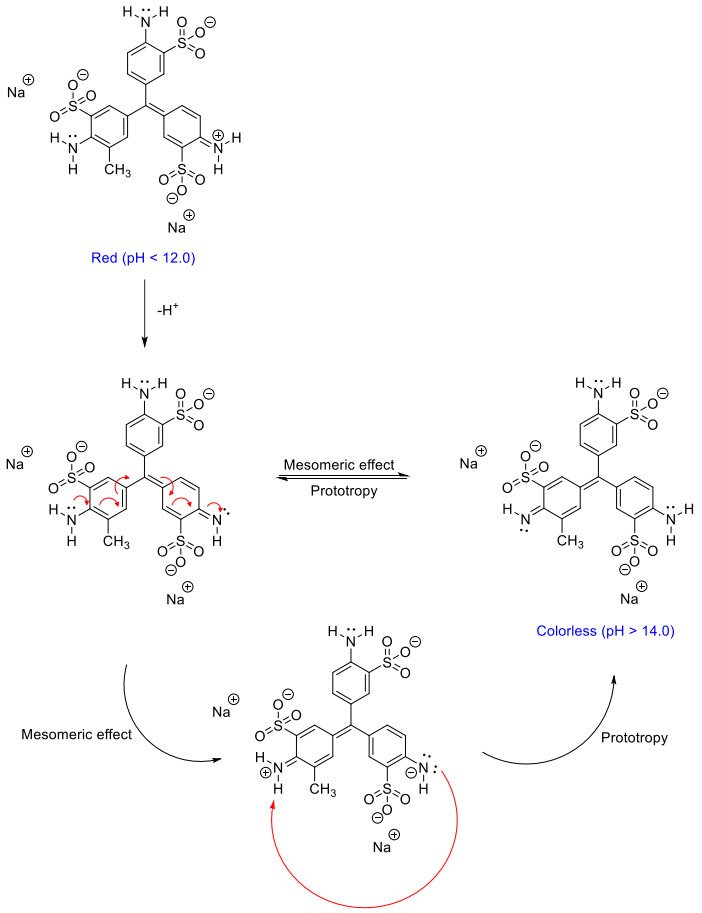

Figure 5-10. Chemical structure of acid fuchsin. CAS registry number 3244-88-0. Molecular weight 737.73 g/mol. pH range of 11.0-14.0. Color change of red (pH<12.0) to colorless (pH>14.0).

The molar concentration of acid fuchsin indicator in a hydrated anion exchange membrane was calculated using the membrane's water uptake in various salt solutions according to Equation 5-34, where cocast wt% referred to the cocast ratio of the indicator and the dry polymer by mass calculated in Equation 5-35, $\mathrm{MW}_{\mathrm{indicator}}$ refers to the molecular weight of indicator (585.55 g/mol for acid fuchsin), $\mathrm{WU}\%$ refers to the

water uptake of the pristine HMT-PMBI as shown in Equation 5-11, and ρ_{H_2O} refers to the density of water. As shown in Table 5-5, the HMT-PMBI membranes cocast with acid fuchsin resulted in an average molar concentration of 1.39 mM in its fully hydrated state in KCl, $KHCO_3$, K_2CO_3 and KOH solutions with a 1.75 wt% cocast concentration and 3.17 mM with a 3.99 wt% cocast concentration.

Equation 5-34 $$c_{ind} = \text{cocast wt\%} \times \frac{1}{MW_{indicator}} \times WU\% \times \rho_{H_2O}$$

Equation 5-35 $$\text{cocast wt\%} \frac{m_{indicator}}{m_{polymer,dry}} \times 100\%$$

Table 5-5. Concentration of acid fuchsin indicator to HMT-PMBI.

cocasting ratio (g indicator/g polymer)	Salt solution	Water uptake (%)[a]	[Indicator] (mM)
1.75 wt%	**KCl**	36.53	1.09
	$KHCO_3$	51.04	1.53
	K_2CO_3	43.23	1.29
	KOH	55.31	1.65
3.99 wt%	**KCl**	36.53	2.49
	$KHCO_3$	51.04	3.48
	K_2CO_3	43.23	2.95
	KOH	55.31	3.77

[a] Previously reported in ref[55].

To calibrate the absorbance of acid fuchsin indicator under various pH, the UV-vis absorbance spectra of 2.11 mM acid fuchsin indicator in pH 11.0 - 13.5 buffer solutions of Na_2HPO_4/Na_3PO_4 was obtained. The calibration was performed on a concentration of acid fuchsin similar to its concentration in the hydrated membrane as shown in Table 5-5. The absorption peak decreased for pH > 11.5 and completely diminished at pH > 12.3, which indicates all the protonated form of acid fuchsin was deprotonated at pH > 12.3. The observed pH range of deprotonation was lower than the reported pH range of 12.0 - 14.0 in the literature.[108]

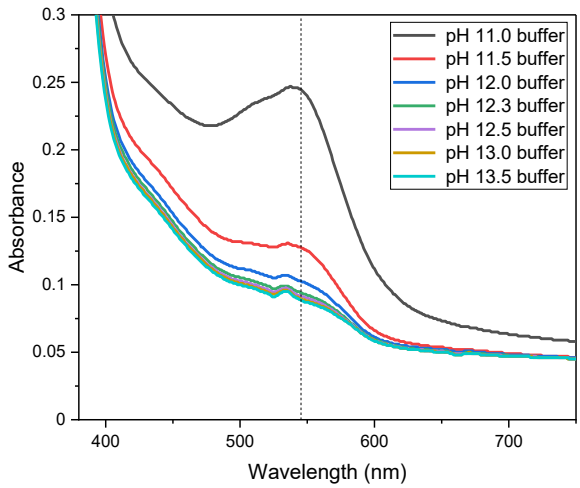

Figure 5-11. UV-vis absorption spectra of the 2.11 mM acid fuchsin indicator in Na_2HPO_4 and Na_3PO_4 buffer solutions with pH 11.0 to 13.5. The dotted line indicates the absorption maximum (546 nm) of acid fuchsin as reported in the literature.[128]

Similarly, HMT-PMBI membrane cocast with 3.76 wt% acid fuchsin were immersed in a Na_3PO_4/Na_2HPO_4 buffer solutions ranging from pH 11.0 to 13.5 for at least 24 hours equilibration and the UV-vis absorbance spectrum was measured. A completely diminished peak at pH > 12.0 was observed shown on Figure 5-12, indicating the counter ion of the anion exchange membrane changed from CO_3^{2-} to OH^- as the pH was increased to > 12.

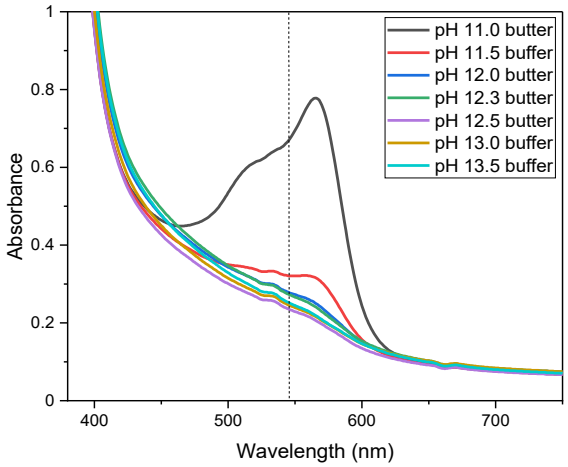

Figure 5-12. UV-vis absorption spectra of the HMT-PMBI membrane containing 3.76 wt% acid fuchsin indicator in Na_3PO_4/Na_2HPO_4 buffer solutions ranging from pH 11.0 to 13.5. The dotted line indicates the absorption maximum of acid fuchsin indicator as reported in the literature.[128]

No obvious difference in colors was observed with the naked eye for the color of the acid fuchsin in aqueous solution nor the HMT-PMBI membranes cocast with acid fuchsin in various pH Na_2HPO_4/Na_3PO_4 buffer solutions as shown in Figure 5-13. However, in comparing the UV-vis absorption spectra of the acid fuchsin in aqueous solution and in HMT-PMBI membrane, the absorption peak started to decrease at basic pH and completely diminished at pH > 12.0 in the membrane but completely diminished at pH > 12.3 in aqueous solution. This difference could be due to its larger local concentration in the ion conducting channel of the membrane. A pH difference of 0.3 is equivalent to 0.5 M OH^-, therefore the local OH^- concentration in the ion conducting channel might be 0.5 M higher than the bulk solution where the membrane was immersed in.

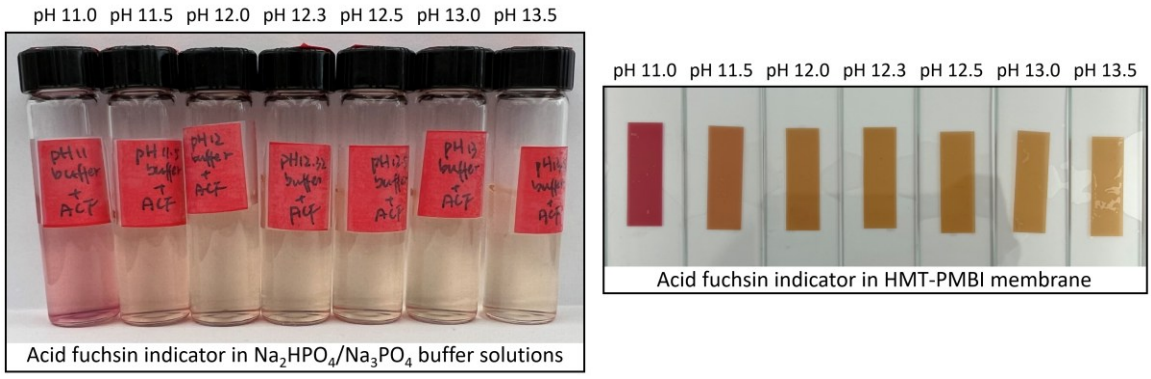

Figure 5-13. Left: photograph of 2.11 mM acid fuchsin indicator in Na_2HPO_4 and Na_3PO_4 buffer solutions (pH 11.0 to 13.5). Right: photograph of 3.76 wt% acid fuchsin in HMT-PMBI membrane equilibrated with Na_2HPO_4 and Na_3PO_4 buffer solutions with the range from pH 11.0 to 13.5.

To study the difference in pKa of acid fuchsin in aqueous solution and in the membrane, the absorbance of its absorption peak was plotted against the pH of the buffer solution as shown in Figure 5-14. The absorbance was observed to drop noticably in the pH range 11-12 for both the acid fuchsin in aqueous solution and in membrane; however, an accurate value of the pKa of acid fuchsin could not be determined based on the absence of data for pH < 11.

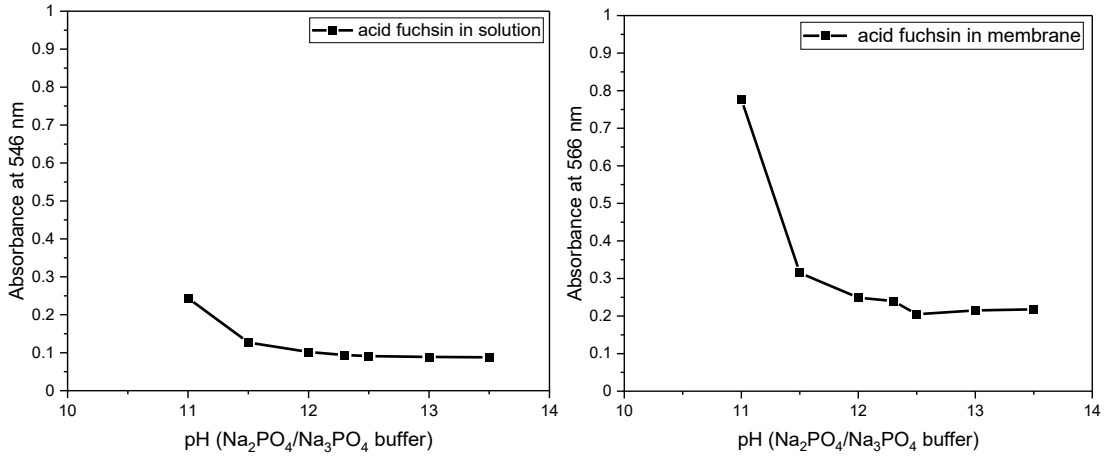

Figure 5-14. The comparison of absorbance change for 2.11 mM acid fuchsin in Na_2HPO_4 and Na_3PO_4 buffer solutions (left) and 3.76 wt% acid fuchsin in the membrane equilibrated in Na_2HPO_4 and Na_3PO_4 buffer solutions (right).

By comparing the UV-vis spectrum of the acid fuchsin indicator in Na_2HPO_4 and Na_3PO_4 buffer solutions (Figure 5-11) and the UV-vis spectrum of the acid fuchsin cocast membrane in Na_2HPO_4 and Na_3PO_4 buffer solutions(Figure 5-12), the absorption peak of the acid fuchsin indicator was observed to shift from 546 nm in aqueous solution to 566 nm in the membrane. The observed shift in the absorption band to a longer wavelength in the membrane indicates the change of the energy gap between the electronic ground state and the excited state of the indicator. Solvatochromic effects often explain a change of position, intensity and shape of the absorption band of a solute in different solvents due to a change in the dielectric constant and hydrogen bonding capacity of various solvating media.[129]

To investigate the reason of the observed shift in absorption maximum, absorption spectra of the acid fuchsin and HMT-PMBI polymer mixtures dissolved in DMSO-water solvent were determined and compared to the acid fuchsin in HMT-PMBI membrane. As shown in Figure 5-15, HMT-PMBI does not show any absorption in the visible region (380 nm – 750 nm) of the spectrum, the absorption peak of acid fuchsin indicator in DMSO-water solution was found to be the same, with or without HMT-PMBI polymer present. The absorption peak of acid fuchsin in the presence of HMT-PMBI in solution was 540 nm and the absorbance was 0.64, which is only 0.03 lower than that of the acid fuchsin in solution. This indicates the ionic interaction between the positively charged functional groups in HMT-PMBI polymer and the deprotonated acid fuchsin

indicator was not significant to cause the absorption peak shift observed for the indicator cocast in the HMT-PMBI membrane for which the absorption maximum shifted from 546 nm to 566 nm. The observed bathochromic shift may be explained by J-aggregation of acid fuchsin indicator due to their solid-state interaction when packed in a solid membrane.

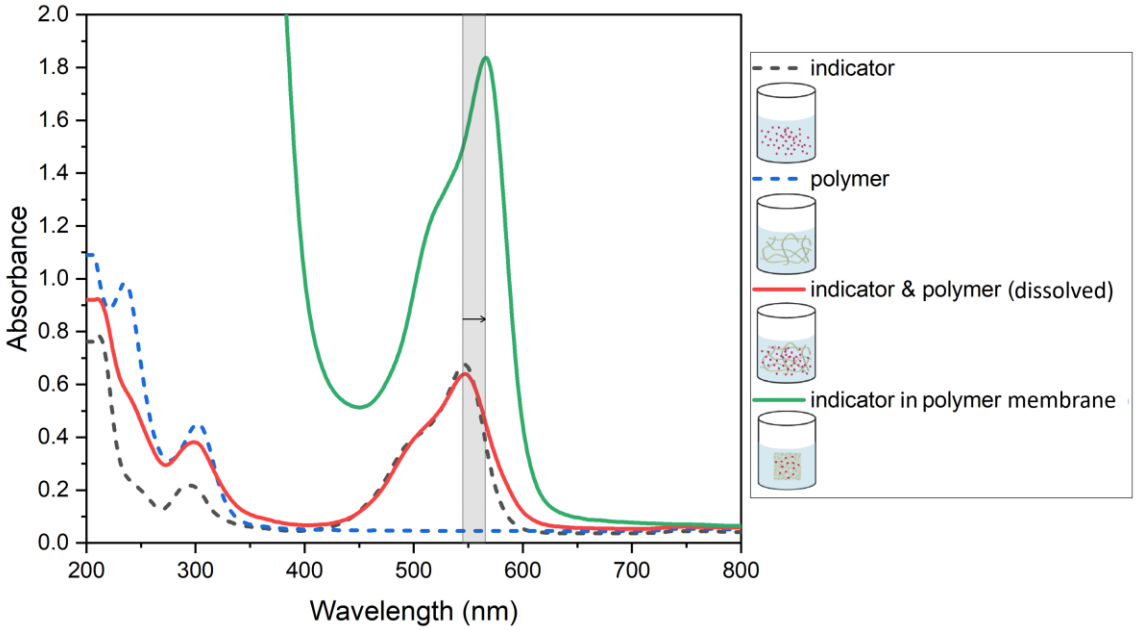

Figure 5-15. Comparison of absorbance spectra of the acid fuchsin indicator (--), HMT-PMBI polymer (--), acid fuchsin and HMT-PMBI dissolved DMSO-water solution (—), and 3.76 wt% acid fuchsin in HMT-PMBI a membrane immersed in water (—).

Although the acid fuchsin cocast HMT-PMBI membranes was found to have a different absorption peak compared to acid fuchsin indicator in aqueous solutions, there is enough evidence to show the cocast membranes does change color as internal pH changes around pH 11-13. Therefore, the acid fuchsin cocast in HMT-PMBI membranes can be examined to investigate the local pH change in a membrane as the counter-ion changes from CO_3^{2-} to OH^-.

Two concentrations of acid fuchsin in HMT-PMBI were initially studied: 1.75 wt% and 3.99 wt% as shown in Figure 5-16. The 1.75 wt% $[\text{acid fuchsin}]_{mem}$ was yellow in color to the naked eye in both the CO_3^{2-} form and OH^- form, while the 3.99 wt% $[\text{acid fuchsin}]_{mem}$ were orange in color in CO_3^{2-} form and yellow in color in OH^- form. This color difference is reflected in the absorbance change from its CO_3^{2-} form to its OH^-

form. Figure 5-17 shows a comparison of the absorbance change at the absorption maximum (566 nm) of the acid fuchsin in HMT-PMBI membranes with 1.75 wt% and 3.99 wt% cocast concentrations. The absorbance at its absorption peak decreased by 0.03 for the 1.75 wt% indicator membrane, which is similar to the absorbance change of 0.04 for the 3.99 wt% indicator membrane. In order to visualize the color change as the local pH changes in the membrane, a cocast ratio of 3.99 wt% was chosen for demonstration because of the higher absorbance drop from its CO_3^{2-} form to its OH^- form.

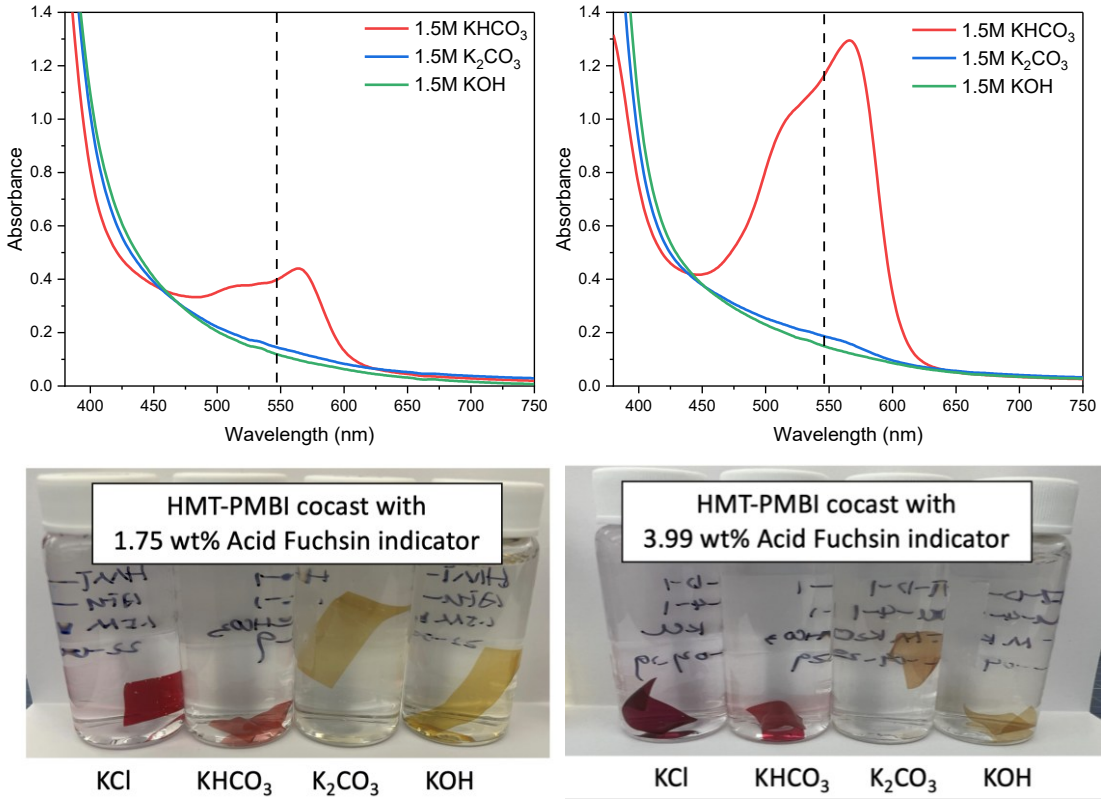

Figure 5-16. Comparison of absorbance spectra and photographs of 1.75 wt% acid fuchsin (left) and 3.99 wt% acid fuchsin (right) in HMT-PMBI and equilibrated in 1.5 M KCl, 1.5 M $KHCO_3$, 1.5 M K_2CO_3 and 1.5 M KOH. The dotted line in the absorption spectra indicates the absorption peakof acid fuchsin in aqueous solution (546 nm) reported in the litrature.[128]

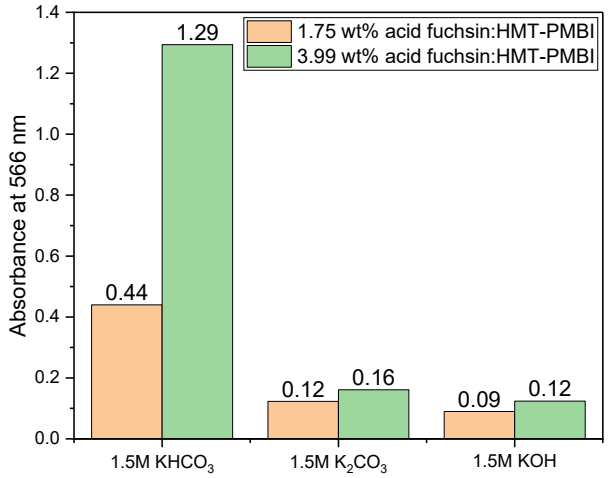

Figure 5-17. Absorbance at absorption maximum (566 nm) of 1.75 wt% acid fuchsin (left) and 3.99 wt% acid fuchsin (right) in HMT-PMBI membranes.

The color change of the acid fuchsin indicator in water, 2.0 M KCl, $KHCO_3$, K_2CO_3 and KOH solutions was compared for HMT-PMBI membrane containing 3.99 wt% acid fuchsin exposed to the same solutions as shown in Figure 5-18. The shade of red color for both acid fuchsin indicator and the acid fuchsin cocast HMT-PMBI membrane was found to gradually diminish as the pH increases in traversing the KCl, $KHCO_3$, K_2CO_3 and KOH solutions.

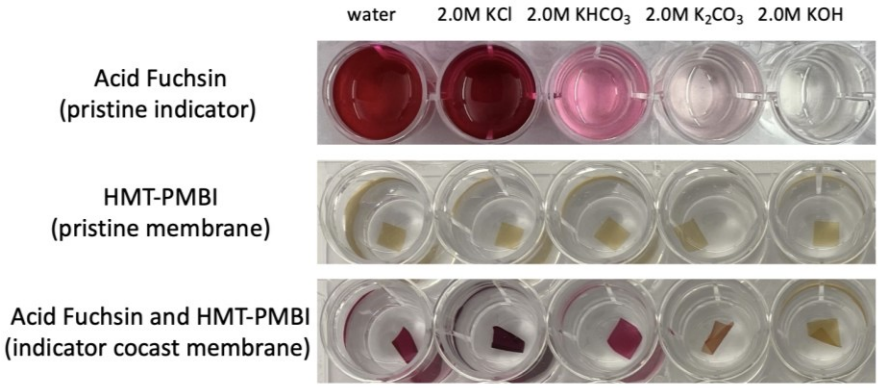

Figure 5-18. Photographs of acid fuchsnin indicator, pristine HMT-PMBI membrane, HMT-PMBI membranes containing 3.99 wt% acid fuchsin exposed in 2.0 M KCl, $KHCO_3$, K_2CO_3 and KOH.

5.3.3. Visualizing the ion exchange process during water electrolysis

As shown in Chapter 4, the ion flushing process during water electrolysis can be visualized using the thymolphthalein incorporated into HMT-PMBI membranes.

However, thymolphthalein indicator is useful for visualising pH changed between 9.3 - 10.5 and can only differentiate HCO_3^- from CO_3^{2-} and OH^-. To differentiate the exchange of CO_3^{2-} to OH^-, aniline blue and acid fuchsin were incorporated into HMT-PMBI to visualize the ion flushing due to their higher pH range.

As shown in Video 5-1. , HMT-PMBI membranes incorporating the 10.7 wt% aniline blue changed from navy blue to maroon upon application of voltage (10 V) across the 1 cm long membrane. Because the useful pH range of the aniline blue indicator is 11.0 to 13.0, the observed color change indicates the OH^- generated via water electrolysis increases the local pH > 13, since at pH > 13, HCO_3^- is replaced with CO_3^{2-}/OH^- according the equilibrium of HCO_3^-, CO_3^{2-} and OH^- shown inFigure 5-3.

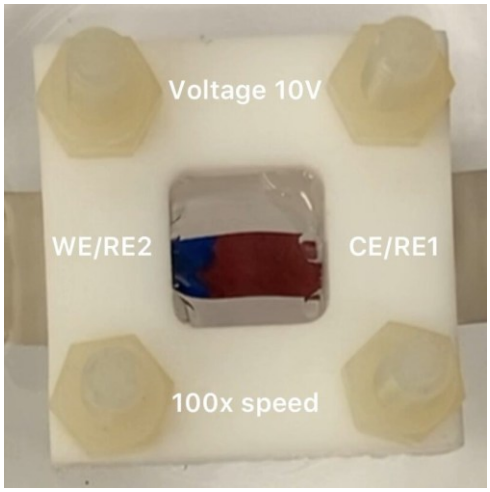

Video 5-1. The color change for 10.7 wt% aniline blue indicator in HMT-PMBI membrane. A voltage of 10 V was applied across the membrane. The membrane was exchanged to its HCO_3^- form prior to the water electrolysis process. Video speed: 100 times.

Note: If you are reading an electronic copy of this thesis, please click the image to be redirected to the video in the Summit Repository or use this link: https://summit.sfu.ca/item/38075

Similarly, the visualization of the ion flushing process induced by water electrolysis was repeated with the 3.99 wt% acid fuchsin incorporated in HMT-PMBI membranes. As shown in Video 5-2, the membrane changed from a pink color to yellow color by applying a voltage of 10 V across the membrane. Because the pH range of the acid fuchsin indicator is 12.0-14.0, the observed color change indicates the OH^- generated via water electrolysis increases the local pH > 14. The 3.99 wt% acid fuchsin incorporated in HMT-PMBI membrane remained orange color when immersed in 2.0 M K_2CO_3 solution and changed to yellow color when immersed in 2.0 M KOH solution as

shown in Figure 5-18. Therefore, it is reasonable to assume OH^- generated by electrolysis flushes out HCO_3^- initially presented in the membrane and reaches concentration equivalent to that of a membrane as the traditional solution exchanged using 2.0 M KOH solution.

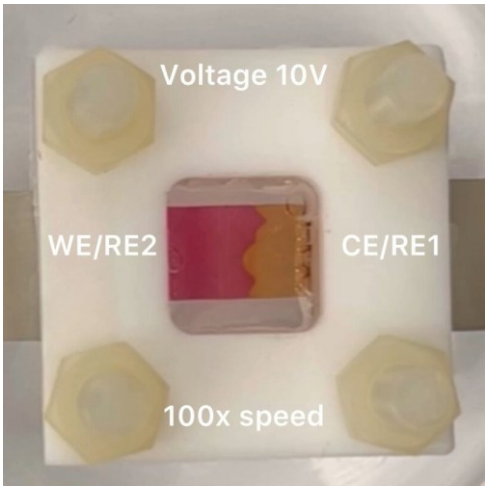

Video 5-2. Video of the color change of 3.99 wt% acid fuchsin indicator incorporated in HMT-PMBI membrane. A voltage of 10 V was applied across the membrane. The membrane was exchanged to its HCO_3^- form prior to the water electrolysis process. Video speed: 100 times.

Note: If you are reading an electronic copy of this thesis, please click the image to be redirected to the video in the Summit Repository or use this link: https://summit.sfu.ca/item/38076

5.3.4. True OH^- conductivity

The OH^- conductivity plays a crucial role in distinguishing between various membranes and identifying those most suitable for fuel cell applications. However, accurately measuring the OH^- conductivity is challenging due to the rapid interaction of OH^- with atmospheric CO_2. This interaction leads to the replacement of OH^- with larger and less mobile anions such as bicarbonate (HCO_3^-) and carbonate (CO_3^{2-}). The visualization of ion flushing process via water electrolysis suggests that the OH^- can be generated by applying a voltage across the membrane. Therefore, the true OH^- conductivity values were also measured using water electrolysis inside a glove box with constant 500 sccm N_2 flow. The membrane was originally in its HCO_3^- form via solution exchange by immersing the membrane in 2.0 M $KHCO_3$ for at least 30 days at room temperature as evident in Figure 5-19. The membrane appears as bright pink color in its solution exchanged HCO_3^- form. The conductivity of the membrane was monitored

under continuous inert gas protection to avoid interference with atmospheric CO_2, except for the period where the membrane was taken out of the glove box and a photograph of the membrane appearance was taken. At the first stage, the conductivity of the membrane increased by 10 mS/cm due to the increased temperature (room temperature to controlled 40°C) and relative humidity (atmospheric ~ 50% to controlled 90%). The appearance of the membrane changed from a bright pink color to an orange color due to the equilibrium of shift from HCO_3^- dominant to CO_3^{2-} dominant. While the membrane was temporarily removed from the glove box to record the appearance of the membrane, the membrane was exposed to atmospheric CO_2, dried out at atmospheric ~ 50% relative humidity, and cooled down to room temperature. Therefore, prior to applying a constant current of 100 μA to initiate the water electrolysis, the membrane was allowed to re-equilibrate to the same temperature and RH with no current applied. The conductivity decreased by 2 mS/cm, which may be explained by an the increased contact resistance as some regions the membrane may have lost contact with the Pt wire electrode while drying out in air. When a constant 100 μA current was applied, the conductivity of the membrane increased due to electrolytically generated OH^-. The conductivity of the membrane increased 400% during the water electrolysis process. The membrane appears yellow for both the region between cathode and anode and outside the anode, orange for region outside the cathode. The yellow region of the membrane after electrolysis maybe explained as the OH^- was generated via electrochemically splitting water at cathode and migrating towards the positively charged anode driven by the potential difference between electrodes.

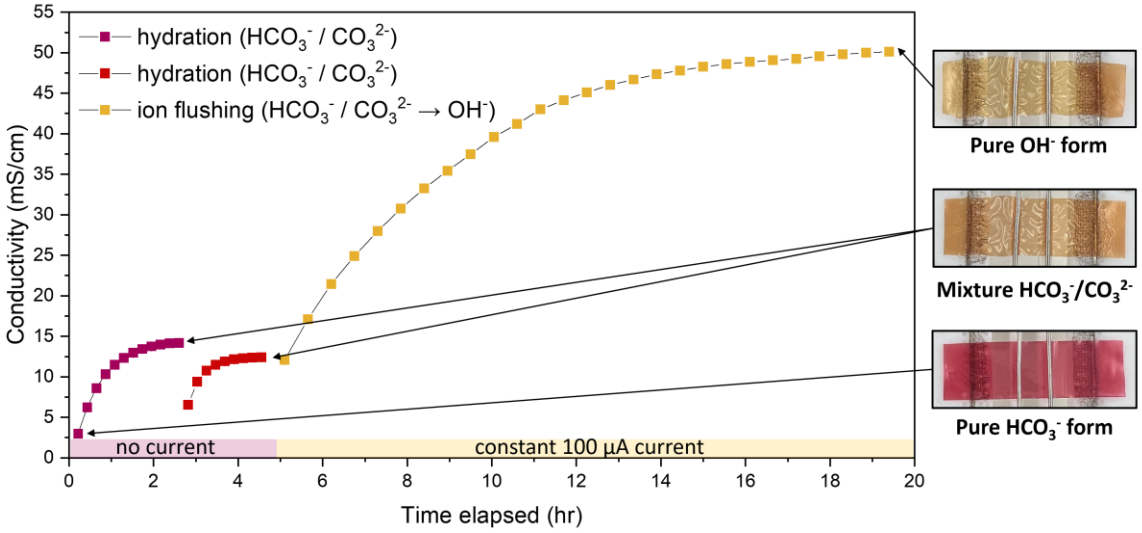

Figure 5-19. Change of conductivity of HMT-PMBI membrane containing 3.99 wt% acid fuchsin during water electrolysis with a 500 sccm flow of inert gas N_2 protection. The membrane was originaly in HCO_3^- form via solution exchange. Prior to applying a constant current of 100 µA to electrolytically generate OH^-, the membrane is pink. After 5 hours equilibration to 40°C and 90%RH, the membrane changed to orange. The yellow color of the membrane after 15 hours electrolysis indicates it reaches pure OH^- form.

5.4. Conclusion and future work

The previous chapter demonstrated the use of a pH indicator to visualize the local pH change in the anion exchange membrane during water electrolysis. However, the thymolphthalein indicator could not distinguish between CO_3^{2-} and OH^-. By using a higher pKa indicator (acid fuchsin), three distinct colours for HCO_3^- (pink) CO_3^{2-} (orange) and OH^- (yellow) could be visualized.

A variety of indicator/polymer concentrations were studied using aniline blue indicator and HMT-PMBI polymer. As the cocast concentration was increased from 0 wt% to10 wt%, the membrane consistently displays as blue in $NaHCO_3$ solution and red in both Na_2CO_3 and NaOH solutions. Therefore, a high cocast concentration of 10 wt% (10 mol% equivalent) only altered the color intensity of the membrane and does not contribute to the observed shift in pKa. The absorbance spectra confirmed aniline blue incorporated in HMT-PMBI membrane shifted to longer wavelength compared to the aniline blue indicator in aqueous solution. The absorption peak of both the CO_3^{2-} form

and OH^- form membrane was found to be ~ 522 nm, while the absorption peak of the aniline blue indicator shifted from 577 nm in 1 M Na_2CO_3 to 498 nm in 1 M NaOH.

The absorption peak of the acid fuchsin cocast HMT-PMBI membrane was also found to be different than the acid fuchsin indicator in aqueous salt solutions. To understand the pKa change of acid fuchsin indicator in aqueous form and cocast with HMT-PMBI in membrane form, future work could be investigating the pKa of acid fuchsin in aqueous solution by a continuous titration among the broader pH range (e.g., pH 7 to 13). However, measuring the pKa of the acid fuchsin incorporated in HMT-PMBI membrane using a continuous titration may be challenging because the delayed response due to the time it takes for the hydrated ionic domains in the membrane equilibrate to the bulk solution into which the membrane is immersed. Alternatively, the pKa of the acid fuchsin in membrane should be determined using a similar method shown in Figure 5-14 with smaller pH increments (e.g., Δ pH 0.2) over a broad range of pH (e.g., pH 7 to 14).

In addition, future work could focus on the search of an appropriate pH indicator with multiple absorption peaks at the visible region. The change of the pKa could be determined by the decrease of absorbance in one absorption peak and by the increase of absorbance in other absorption peak.

Chapter 6. Global Conclusion and Future Work

The work presented in this thesis focuses on understanding the ion transport process that occurs in an anion exchange membrane by measuring the physiochemical properties of the membrane. Various anion forms (e.g. Cl^-, HCO_3^-, CO_3^{2-} and OH^-) were scrutinized. As a summary of the measurements taken: the degree of methylation of the polymer and the theoretical ion exchange capacity of the membrane were determined using NMR spectroscopic analysis, the water uptake and dimensional swell were determined using image analysis and gravimetric analysis, the conductivity of the membrane was determined using electrochemical impedance spectroscopy and linear sweep voltammetry, the experimental ion exchange capacity of a membrane and the pH of the bulk solution were determined using ion-selecting electrode and pH electrode, and finally, the color of the indicator and membranes were analyzed using UV-vis absorption spectra.

In chapter 3, the conductivity of the commercialized polyimidazolium based membrane (Aemion$^+$) was measured to study the effect of the polyolefin substrate reinforcement on the membrane performance for H_2 fuel cell application. The protocols for measuring the conductivity of a membrane for both the in-plane and through-plane were optimized. The anisotropic ratio (through-plane / in-plane conductivity) of the 10 μm reinforced Aemion$^+$ in its Cl^- form increased by 200% for every 10°C increase in temperature, while the 40 μm reinforced Aemion$^+$ in its Cl^- form increased less than 10%. Therefore, the polyolefin reinforcement substrate has a greater impact on the membrane's anisotropic property of a thinner membrane than a thicker membrane. The in-plane conductivity of the reinforced 40 μm Aemion$^+$ membrane (Cl^- form) was similar to the in-plane conductivity of monolithic 50 μm Aemion$^+$ membrane (Cl^- form); however, the through-plane conductivity of the reinforced 40 μm Aemion$^+$ membrane (Cl^- form) was only ¼ of the through-plane conductivity of the monolithic 50 μm Aemion$^+$ membrane (Cl^- form). Thus, the reinforcement substrate mainly affects the through-plane conductivity.

In chapter 4, a method was proposed for using a pH indicator to visualize the anion change in an anion exchange membrane, measuring the conductivity of the membrane in its pure OH^- form by electrolytically generating OH^- through water

electrolysis. The thymolphthalein-doped HMT-PMBI is yellow in its HCO_3^- form and blue in its CO_3^{2-} and OH^- forms. The colour of the thymolphthalein-doped HMT-PMBI changes from yellow to blue after 15 hours of water electrolysis, indicating that the initially presented HCO_3^- in the membrane was flushed out with the electrolytically generated OH^-. The in-plane conductivity of the thymolphthalein-doped HMT-PMBI membrane increased by 400% after the electrolysis, which also indicates the anions in the membrane changed to a more mobile OH^-. However, the thymolphthalein indicator could not distinguish between CO_3^{2-} with OH^- because its pH range where it changes colour of 9.4 -10.6.

In chapter 5, indicators with higher pKa (aniline blue and acid fuchsin) were used to prepare the indicator doped membrane to distinguish CO_3^{2-} and OH^-. The aniline blue (pH range 11.0-13.0) doped HMT-PMBI membrane displays the same colour in its CO_3^{2-} and OH^- form, while the acid fuchsin (pH range 12.0-14.0) doped membrane displays three distinct colours for HCO_3^- (pink) CO_3^{2-} (orange) and OH^- (yellow). The visualization of ion conversion from HCO_3^- to OH^- by water electrolysis was repeated with the HMT-PMBI membrane containing acid fuchsin indicator. The acid fuchsin in HMT-PMBI membrane was pink before applying a 100 μA current to initiate the water electrolysis reaction. As the membrane equilibrated to the target temperature and relative humidity in the environmental chamber, the pink colour changed to orange which indicates the presence of a mixture of HCO_3^-, CO_3^{2-} and OH^-. The conductivity of the membrane increased by 400% for 15 hours of water electrolysis, and the membrane changed to yellow indicating the electrolytically generated OH^- is the dominant charge carrier.

The work presented in this thesis has provided experimental evidence that the water electrolysis on a bare membrane generated enough hydroxide ions which increased the local pH and the conductivity of the anion exchange membrane. The increased pH was visualized by the color change of the pH indicator doped membrane (HMT-PMBI with thymolphthalein, aniline blue and acid fuchsin indicators). The increased conductivity was calculated from the decreased slope of the potentiodynamic sweep. Future work in this area should include theoretical modeling of the anion concentration change to support the observed color change as shown in published by Kubannek et al in 2023.[130] As the aniline blue and acid fuchsin indicator possesses a higher pKa than thymolphthalein, the simulation of the decarbonation process of the

aniline blue and acid fuchsin doped membrane should provide future evidence on the local pH change, especially in differentiating CO_3^{2-} with OH^-.

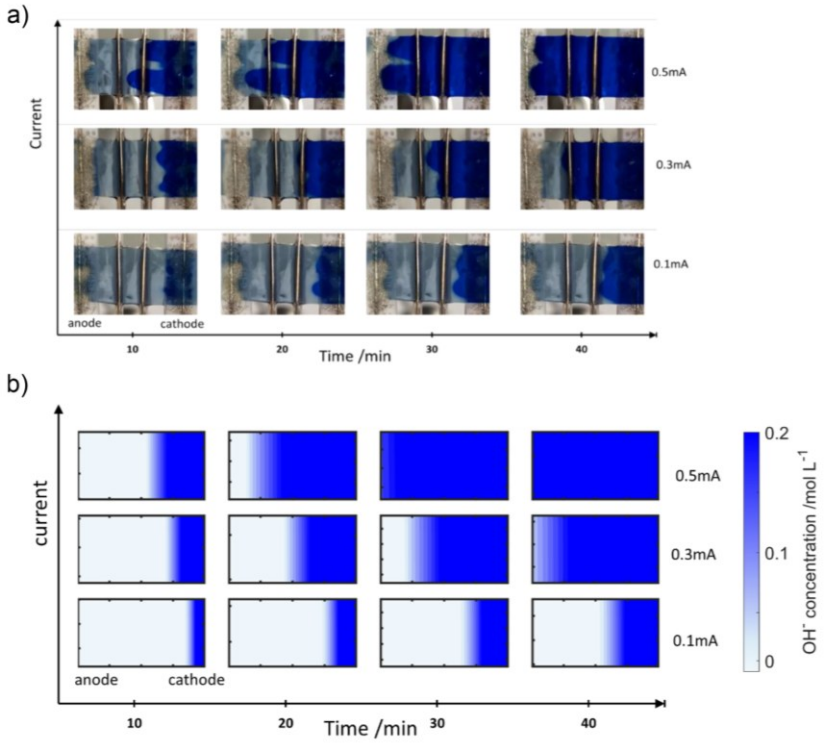

Figure 6-1. Comparison of the experimental observed color change of the decarbonation process for an ldpe-btma membrane pretreated with 0.2 wt% thymolphthalein solution (a) and the simulated OH^- concentration (b). The decarbonation was conducted repeated with 0.1 mA, 0.3 mA and 0.5 mA current. Adapted from ref[130]

It is also worth designing specialized electrochemical cells to investigate other membrane materials. Hohenadel et al studied the “unwanted” co-ion leakage of anions from the catholyte to anolyte and cations from the anolyte to catholyte in a bipolar membrane using a specialized quartz cell and the thymolphthalein doped HMT-PMBI as the anion exchange component of the bipolar membrane.[131]

This thesis only compared the Cl^- conductivity of the AEMION® with and without reinforcement at two thickness (10 μm and 40 μm). Additional reinforcement should be investigated to investigate how does the through plane conductivity changed with the thickness of the membrane.

References

(1) Sharaf, O. Z.; Orhan, M. F. An Overview of Fuel Cell Technology: Fundamentals and Applications. Renew. Sustain. Energy Rev. 2014, 32, 810–853. https://doi.org/10.1016/j.rser.2014.01.012.

(2) Bockris, J. O. M. The Hydrogen Economy: Its History. Int. J. Hydrog. Energy 2013, 38 (6), 2579–2588. https://doi.org/10.1016/j.ijhydene.2012.12.026.

(3) Marbán, G.; Valdés-Solís, T. Towards the Hydrogen Economy? Int. J. Hydrog. Energy 2007, 32 (12), 1625–1637. https://doi.org/10.1016/j.ijhydene.2006.12.017.

(4) Balat, M. Potential Importance of Hydrogen as a Future Solution to Environmental and Transportation Problems. Int. J. Hydrog. Energy 2008, 33 (15), 4013–4029. https://doi.org/10.1016/j.ijhydene.2008.05.047.

(5) Lee, M.-Y.; Park, K. T.; Lee, W.; Lim, H.; Kwon, Y.; Kang, S. Current Achievements and the Future Direction of Electrochemical CO 2 Reduction: A Short Review. Crit. Rev. Environ. Sci. Technol. 2020, 50 (8), 769–815. https://doi.org/10.1080/10643389.2019.1631991.

(6) Varcoe, J. R.; Atanassov, P.; Dekel, D. R.; Herring, A. M.; Hickner, M. A.; Kohl, Paul. A.; Kucernak, A. R.; Mustain, W. E.; Nijmeijer, K.; Scott, K.; Xu, T.; Zhuang, L. Anion-Exchange Membranes in Electrochemical Energy Systems. Energy Env. Sci 2014, 7 (10), 3135–3191. https://doi.org/10.1039/C4EE01303D.

(7) Merle, G.; Wessling, M.; Nijmeijer, K. Anion Exchange Membranes for Alkaline Fuel Cells: A Review. J. Membr. Sci. 2011, 377 (1–2), 1–35. https://doi.org/10.1016/j.memsci.2011.04.043.

(8) Dekel, D. R. Review of Cell Performance in Anion Exchange Membrane Fuel Cells. J. Power Sources 2018, 375, 158–169. https://doi.org/10.1016/j.jpowsour.2017.07.117.

(9) Gottesfeld, S.; Dekel, D. R.; Page, M.; Bae, C.; Yan, Y.; Zelenay, P.; Kim, Y. S. Anion Exchange Membrane Fuel Cells: Current Status and Remaining Challenges. J. Power Sources 2018, 375, 170–184. https://doi.org/10.1016/j.jpowsour.2017.08.010.

(10) Brauns, J.; Turek, T. Alkaline Water Electrolysis Powered by Renewable Energy: A Review. Processes 2020, 8 (2), 248. https://doi.org/10.3390/pr8020248.

(11) Park, J. E.; Kang, S. Y.; Oh, S.-H.; Kim, J. K.; Lim, M. S.; Ahn, C.-Y.; Cho, Y.-H.; Sung, Y.-E. High-Performance Anion-Exchange Membrane Water Electrolysis. Electrochimica Acta 2019, 295, 99–106. https://doi.org/10.1016/j.electacta.2018.10.143.

(12) Vincent, I.; Bessarabov, D. Low Cost Hydrogen Production by Anion Exchange Membrane Electrolysis: A Review. Renew. Sustain. Energy Rev. 2018, 81, 1690–1704. https://doi.org/10.1016/j.rser.2017.05.258.

(13) Henkensmeier, D.; Najibah, M.; Harms, C.; Žitka, J.; Hnát, J.; Bouzek, K. Overview: State-of-the Art Commercial Membranes for Anion Exchange Membrane Water Electrolysis. J. Electrochem. Energy Convers. Storage 2021, 18 (2), 024001. https://doi.org/10.1115/1.4047963.

(14) Wei, P.; Li, H.; Lin, L.; Gao, D.; Zhang, X.; Gong, H.; Qing, G.; Cai, R.; Wang, G.; Bao, X. CO2 Electrolysis at Industrial Current Densities Using Anion Exchange Membrane Based Electrolyzers. Sci. China Chem. 2020, 63 (12), 1711–1715. https://doi.org/10.1007/s11426-020-9825-9.

(15) Salvatore, D. A.; Gabardo, C. M.; Reyes, A.; O'Brien, C. P.; Holdcroft, S.; Pintauro, P.; Bahar, B.; Hickner, M.; Bae, C.; Sinton, D.; Sargent, E. H.; Berlinguette, C. P. Designing Anion Exchange Membranes for CO2 Electrolysers. Nat. Energy 2021, 6 (4), 339–348. https://doi.org/10.1038/s41560-020-00761-x.

(16) O'Hayre, R.; Suk-Won, C.; Whitney G., C.; Fritz B., P. Fuel Cell Fundamentals, Third edition.; Wiley, 2016.

(17) Palo, D. R.; Dagle, R. A.; Holladay, J. D. Methanol Steam Reforming for Hydrogen Production. Chem. Rev. 2007, 107 (10), 3992–4021. https://doi.org/10.1021/cr050198b.

(18) Haryanto, A.; Fernando, S.; Murali, N.; Adhikari, S. Current Status of Hydrogen Production Techniques by Steam Reforming of Ethanol: A Review. Energy Fuels 2005, 19 (5), 2098–2106. https://doi.org/10.1021/ef0500538.

(19) Carmo, M.; Fritz, D. L.; Mergel, J.; Stolten, D. A Comprehensive Review on PEM Water Electrolysis. Int. J. Hydrog. Energy 2013, 38 (12), 4901–4934. https://doi.org/10.1016/j.ijhydene.2013.01.151.

(20) Wendt, H.; Kreysa, G. Electrochemical Engineering: Science and Technology in Chemical and Other Industries; Springer Science & Business Media, 1999.

(21) Ulleberg, O. Modeling of Advanced Alkaline Electrolyzers: A System Simulation Approach. Int. J. Hydrog. Energy 2003, 28 (1), 21–33. https://doi.org/10.1016/S0360-3199(02)00033-2.

(22) Grigoriev, S. A.; Fateev, V. N.; Bessarabov, D. G.; Millet, P. Current Status, Research Trends, and Challenges in Water Electrolysis Science and Technology. Int. J. Hydrog. Energy 2020, 45 (49), 26036–26058. https://doi.org/10.1016/j.ijhydene.2020.03.109.

(23) Schröder, V.; Emonts, B.; Janßen, H.; Schulze, H.-P. Explosion Limits of Hydrogen/Oxygen Mixtures at Initial Pressures up to 200 Bar. Chem. Eng. Technol. 2004, 27 (8), 847–851. https://doi.org/10.1002/ceat.200403174.

(24) Wang, M.; Wang, Z.; Gong, X.; Guo, Z. The Intensification Technologies to Water Electrolysis for Hydrogen Production – A Review. Renew. Sustain. Energy Rev. 2014, 29, 573–588. https://doi.org/10.1016/j.rser.2013.08.090.

(25) Grigoriev, S. A.; Fateev, V. N.; Millet, P. Alkaline Electrolysers; 2022.

(26) Phillips, R.; Edwards, A.; Rome, B.; Jones, D. R.; Dunnill, C. W. Minimising the Ohmic Resistance of an Alkaline Electrolysis Cell through Effective Cell Design. Int. J. Hydrog. Energy 2017, 42 (38), 23986–23994. https://doi.org/10.1016/j.ijhydene.2017.07.184.

(27) Grigor'ev, S. A.; Khaliullin, M. M.; Kuleshov, N. V.; Fateev, V. N. Electrolysis of Water in a System with a Solid Polymer Electrolyte at Elevated Pressure. 2001, 1 (8).

(28) Xu, D.; Stevens, M. B.; Cosby, M. R.; Oener, S. Z.; Smith, A. M.; Enman, L. J.; Ayers, K. E.; Capuano, C. B.; Renner, J. N.; Danilovic, N.; Li, Y.; Wang, H.; Zhang, Q.; Boettcher, S. W. Earth-Abundant Oxygen Electrocatalysts for Alkaline Anion-Exchange-Membrane Water Electrolysis: Effects of Catalyst Conductivity and Comparison with Performance in Three-Electrode Cells. ACS Catal. 2019, 9 (1), 7–15. https://doi.org/10.1021/acscatal.8b04001.

(29) Xu, Z.; Wan, L.; Liao, Y.; Wang, P.; Liu, K.; Wang, B. Anisotropic Anion Exchange Membranes with Extremely High Water Uptake for Water Electrolysis and Fuel Cells. J. Mater. Chem. A 2021, 9 (41), 23485–23496. https://doi.org/10.1039/D1TA06579C.

(30) Wang, X.; Qiao, X.; Liu, S.; Liu, L.; Li, N. Poly(Terphenyl Piperidinium) Containing Hydrophilic Crown Ether Units in Main Chains as Anion Exchange Membranes for Alkaline Fuel Cells and Water Electrolysers. J. Membr. Sci. 2022, 653, 120558. https://doi.org/10.1016/j.memsci.2022.120558.

(31) Luo, X.; Rojas-Carbonell, S.; Yan, Y.; Kusoglu, A. Structure-Transport Relationships of Poly(Aryl Piperidinium) Anion-Exchange Membranes: Eeffect of Anions and Hydration. J. Membr. Sci. 2020, 598, 117680. https://doi.org/10.1016/j.memsci.2019.117680.

(32) Jin, S.; Hao, Z.; Zhang, K.; Yan, Z.; Chen, J. Advances and Challenges for the Electrochemical Reduction of CO 2 to CO: From Fundamentals to Industrialization. Angew. Chem. 2021, 133 (38), 20795–20816. https://doi.org/10.1002/ange.202101818.

(33) Mao, J.; Iocozzia, J.; Huang, J.; Meng, K.; Lai, Y.; Lin, Z. Graphene Aerogels for Efficient Energy Storage and Conversion. Energy Environ. Sci. 2018, 11 (4), 772–799. https://doi.org/10.1039/C7EE03031B.

(34) Larrazábal, G. O.; Strøm-Hansen, P.; Heli, J. P.; Zeiter, K.; Therkildsen, K. T.; Chorkendorff, I.; Seger, B. Analysis of Mass Flows and Membrane Cross-over in CO 2 Reduction at High Current Densities in an MEA-Type Electrolyzer. ACS Appl. Mater. Interfaces 2019, 11 (44), 41281–41288. https://doi.org/10.1021/acsami.9b13081.

(35) Burdyny, T.; Smith, W. A. CO 2 Reduction on Gas-Diffusion Electrodes and Why Catalytic Performance Must Be Assessed at Commercially-Relevant Conditions. Energy Environ. Sci. 2019, 12 (5), 1442–1453. https://doi.org/10.1039/C8EE03134G.

(36) Dufek, E. J.; Lister, T. E.; McIlwain, M. E. Bench-Scale Electrochemical System for Generation of CO and Syn-Gas. J. Appl. Electrochem. 2011, 41 (6), 623–631. https://doi.org/10.1007/s10800-011-0271-6.

(37) Wakerley, D.; Lamaison, S.; Wicks, J.; Clemens, A.; Feaster, J.; Corral, D.; Jaffer, S. A.; Sarkar, A.; Fontecave, M.; Duoss, E. B.; Baker, S.; Sargent, E. H.; Jaramillo, T. F.; Hahn, C. Gas Diffusion Electrodes, Reactor Designs and Key Metrics of Low-Temperature CO2 Electrolysers. Nat. Energy 2022, 7 (2), 130–143. https://doi.org/10.1038/s41560-021-00973-9.

(38) Deavin, O. I.; Murphy, S.; Ong, A. L.; Poynton, S. D.; Zeng, R.; Herman, H.; Varcoe, J. R. Anion-Exchange Membranes for Alkaline Polymer Electrolyte Fuel Cells: Comparison of Pendent Benzyltrimethylammonium- and Benzylmethylimidazolium-Head-Groups. Energy Environ. Sci. 2012, 5 (9), 8584. https://doi.org/10.1039/c2ee22466f.

(39) Zhang, M.; Kim, H. K.; Chalkova, E.; Mark, F.; Lvov, S. N.; Chung, T. C. M. New Polyethylene Based Anion Exchange Membranes (PE–AEMs) with High Ionic Conductivity. Macromolecules 2011, 44 (15), 5937–5946. https://doi.org/10.1021/ma200836d.

(40) Kostalik, H. A.; Clark, T. J.; Robertson, N. J.; Mutolo, P. F.; Longo, J. M.; Abruña, H. D.; Coates, G. W. Solvent Processable Tetraalkylammonium-Functionalized Polyethylene for Use as an Alkaline Anion Exchange Membrane. Macromolecules 2010, 43 (17), 7147–7150. https://doi.org/10.1021/ma101172a.

(41) Ko, B.-S.; Sohn, J.-Y.; Shin, J. Radiation-Induced Synthesis of Solid Alkaline Exchange Membranes with Quaternized 1,4-Diazabicyclo[2,2,2] Octane Pendant Groups for Fuel Cell Application. Polymer 2012, 53 (21), 4652–4661. https://doi.org/10.1016/j.polymer.2012.08.002.

(42) Zhou, J.; Joseph, K.; Ahlfield, J. M.; Park, D.-Y.; Kohl, P. A. Poly(Arylene Ether) Ionomers with Pendant Quinuclidium Groups and Varying Molecular Weight for Alkaline Electrodes. J. Electrochem. Soc. 2013, 160 (6), F573–F578. https://doi.org/10.1149/2.077306jes.

(43) Arges, C. G.; Wang, L.; Parrondo, J.; Ramani, V. Best Practices for Investigating Anion Exchange Membrane Suitability for Alkaline Electrochemical Devices: Case Study Using Quaternary Ammonium Poly(2,6-Dimethyl 1,4-Phenylene)Oxide Anion Exchange Membranes. J. Electrochem. Soc. 2013, 160 (11), F1258–F1274. https://doi.org/10.1149/2.049311jes.

(44) Lee, J. Y.; Lim, D.-H.; Chae, J. E.; Choi, J.; Kim, B. H.; Lee, S. Y.; Yoon, C. W.; Nam, S. Y.; Jang, J. H.; Henkensmeier, D.; Yoo, S. J.; Kim, J.-Y.; Kim, H.-J.; Ham, H. C. Base Tolerant Polybenzimidazolium Hydroxide Membranes for Solid Alkaline-Exchange Membrane Fuel Cells. J. Membr. Sci. 2016, 514, 398–406. https://doi.org/10.1016/j.memsci.2016.05.012.

(45) Henkensmeier, D.; Cho, H.; Brela, M.; Michalak, A.; Dyck, A.; Germer, W.; Duong, N. M. H.; Jang, J. H.; Kim, H.-J.; Woo, N.-S.; Lim, T.-H. Anion Conducting Polymers Based on Ether Linked Polybenzimidazole (PBI-OO). Int. J. Hydrog. Energy 2014, 39 (6), 2842–2853. https://doi.org/10.1016/j.ijhydene.2013.07.091.

(46) An, L.; Zeng, L.; Zhao, T. S. An Alkaline Direct Ethylene Glycol Fuel Cell with an Alkali-Doped Polybenzimidazole Membrane. Int. J. Hydrog. Energy 2013, 38 (25), 10602–10606. https://doi.org/10.1016/j.ijhydene.2013.06.042.

(47) Thomas, O. D.; Soo, K. J. W. Y.; Peckham, T. J.; Kulkarni, M. P.; Holdcroft, S. A Stable Hydroxide-Conducting Polymer. J. Am. Chem. Soc. 2012, 134 (26), 10753–10756. https://doi.org/10.1021/ja303067t.

(48) Hou, H.; Sun, G.; He, R.; Sun, B.; Jin, W.; Liu, H.; Xin, Q. Alkali Doped Polybenzimidazole Membrane for Alkaline Direct Methanol Fuel Cell. Int. J. Hydrog. Energy 2008, S036031990801152X. https://doi.org/10.1016/j.ijhydene.2008.09.023.

(49) Wei, Q.; Cao, X.; Veh, P.; Konovalova, A.; Mardle, P.; Overton, P.; Cassegrain, S.; Vierrath, S.; Breitwieser, M.; Holdcroft, S. On the Stability of Anion Exchange Membrane Fuel Cells Incorporating Polyimidazolium Ionene (Aemion+®) Membranes and Ionomers. Sustain. Energy Fuels 2022, 6 (15), 3551–3564. https://doi.org/10.1039/D2SE00690A.

(50) Overton, P.; Li, W.; Cao, X.; Holdcroft, S. Tuning Ion Exchange Capacity in Hydroxide-Stable Poly(Arylimidazolium) Ionenes: Increasing the Ionic Content Decreases the Dependence of Conductivity and Hydration on Temperature and Humidity. Macromolecules 2020, 53 (23), 10548–10560. https://doi.org/10.1021/acs.macromol.0c02014.

(51) Cao, X.; Novitski, D.; Holdcroft, S. Visualization of Hydroxide Ion Formation upon Electrolytic Water Splitting in an Anion Exchange Membrane. ACS Mater. Lett. 2019, 1 (3), 362–366. https://doi.org/10.1021/acsmaterialslett.9b00195.

(52) Fortin, P.; Khoza, T.; Cao, X.; Martinsen, S. Y.; Oyarce Barnett, A.; Holdcroft, S. High-Performance Alkaline Water Electrolysis Using AemionTM Anion Exchange Membranes. J. Power Sources 2020, 451, 227814. https://doi.org/10.1016/j.jpowsour.2020.227814.

(53) Fan, J.; Willdorf-Cohen, S.; Schibli, E. M.; Paula, Z.; Li, W.; Skalski, T. J. G.; Sergeenko, A. T.; Hohenadel, A.; Frisken, B. J.; Magliocca, E.; Mustain, W. E.; Diesendruck, C. E.; Dekel, D. R.; Holdcroft, S. Poly(Bis-Arylimidazoliums) Possessing High Hydroxide Ion Exchange Capacity and High Alkaline Stability. Nat. Commun. 2019, 10 (1), 2306. https://doi.org/10.1038/s41467-019-10292-z.

(54) Hu, M.; Pearce, E. M.; Kwei, T. K. Modification of Polybenzimidazole: Synthesis and Thermal Stability of Poly(N1-Methylbenzimidazole) and Poly(N1,N3-Dimethylbenzimidazolium) Salt. J. Polym. Sci. Part Polym. Chem. 1993, 31 (2), 553–561. https://doi.org/10.1002/pola.1993.080310228.

(55) Wright, A. G.; Fan, J.; Britton, B.; Weissbach, T.; Lee, H.-F.; Kitching, E. A.; Peckham, T. J.; Holdcroft, S. Hexamethyl-p-Terphenyl Poly(Benzimidazolium): A Universal Hydroxide-Conducting Polymer for Energy Conversion Devices. Energy Environ. Sci. 2016, 9 (6), 2130–2142. https://doi.org/10.1039/C6EE00656F.

(56) Jiang, S. P.; Li, Q. Introduction to Fuel Cells: Electrochemistry and Materials; Springer Singapore: Singapore, 2022. https://doi.org/10.1007/978-981-10-7626-8.

(57) Veh, P.; Britton, B.; Holdcroft, S.; Zengerle, R.; Vierrath, S.; Breitwieser, M. Improving the Water Management in Anion-Exchange Membrane Fuel Cells via Ultra-Thin, Directly Deposited Solid Polymer Electrolyte. RSC Adv. 2020, 10 (15), 8645–8652. https://doi.org/10.1039/C9RA09628K.

(58) O'Hayre, R. P.; Cha, S.-W.; Colella, W. G.; Prinz, F. B. Fuel Cell Fundamentals, Third edition.; John Wiley & Sons Inc: Hoboken, New Jersey, 2016.

(59) Wiley, J. Fundamentals of Electrochemistry, Edited by Vladimir S. Bagotsky, John Wiley & Sons, Incorporated, 2005. ProQuest Ebook Central, Http://Ebookcentral.Proquest.Com/Lib/Sfu-Ebooks/Detail.Action?docID=242872. Created from Sfu-Ebooks on 2023-04-27 17:29:57. Fundam. Electrochem.

(60) Ziv, N.; Mondal, A. N.; Weissbach, T.; Holdcroft, S.; Dekel, D. R. Effect of CO2 on the Properties of Anion Exchange Membranes for Fuel Cell Applications. J. Membr. Sci. 2019, 586, 140–150. https://doi.org/10.1016/j.memsci.2019.05.053.

(61) Cahan, B. D.; Wainright, J. S. AC Impedance Investigations of Proton Conduction in NafionTM. J. Electrochem. Soc. 1993, 140 (12), L185. https://doi.org/10.1149/1.2221160.

(62) Bard, A. J.; Faulkner, L. R. Electrochemical Methods: Fundamentals and Applications, 2nd ed.; Wiley: New York, 2001.

(63) Moukheiber, E.; De Moor, G.; Flandin, L.; Bas, C. Investigation of Ionomer Structure through Its Dependence on Ion Exchange Capacity (IEC). J. Membr. Sci. 2012, 389, 294–304. https://doi.org/10.1016/j.memsci.2011.10.041.

(64) Guler, E.; Zhang, Y.; Saakes, M.; Nijmeijer, K. Tailor-Made Anion-Exchange Membranes for Salinity Gradient Power Generation Using Reverse Electrodialysis. ChemSusChem 2012, 5 (11), 2262–2270. https://doi.org/10.1002/cssc.201200298.

(65) Slade, R. C. T.; Varcoe, J. R. Investigations of Conductivity in FEP-Based Radiation-Grafted Alkaline Anion-Exchange Membranes. Solid State Ion. 2005, 176 (5–6), 585–597. https://doi.org/10.1016/j.ssi.2004.09.044.

(66) Karas, F.; Hnát, J.; Paidar, M.; Schauer, J.; Bouzek, K. Determination of the Ion-Exchange Capacity of Anion-Selective Membranes. Int. J. Hydrog. Energy 2014, 39 (10), 5054–5062. https://doi.org/10.1016/j.ijhydene.2014.01.074.

(67) Tse, Y.-L. S.; Sarode, H. N.; Lindberg, G. E.; Witten, T. A.; Yang, Y.; Herring, A. M.; Voth, G. A. Chloride Enhances Fluoride Mobility in Anion Exchange Membrane/Polycationic Systems. J. Phys. Chem. C 2014, 118 (2), 845–853. https://doi.org/10.1021/jp409728a.

(68) Wang, S.; Jiang, S. P. Prospects of Fuel Cell Technologies. Natl. Sci. Rev. 2017, 4 (2), 163–166. https://doi.org/10.1093/nsr/nww099.

(69) Ramaswamy, N.; Mukerjee, S. Alkaline Anion-Exchange Membrane Fuel Cells: Challenges in Electrocatalysis and Interfacial Charge Transfer. Chem. Rev. 2019, 119 (23), 11945–11979. https://doi.org/10.1021/acs.chemrev.9b00157.

(70) Omasta, T. J.; Wang, L.; Peng, X.; Lewis, C. A.; Varcoe, J. R.; Mustain, W. E. Importance of Balancing Membrane and Electrode Water in Anion Exchange Membrane Fuel Cells. J. Power Sources 2018, 375, 205–213. https://doi.org/10.1016/j.jpowsour.2017.05.006.

(71) Pan, J.; Chen, C.; Li, Y.; Wang, L.; Tan, L.; Li, G.; Tang, X.; Xiao, L.; Lu, J.; Zhuang, L. Constructing Ionic Highway in Alkaline Polymer Electrolytes. Energy Env. Sci 2014, 7 (1), 354–360. https://doi.org/10.1039/C3EE43275K.

(72) Pan, J.; Chen, C.; Zhuang, L.; Lu, J. Designing Advanced Alkaline Polymer Electrolytes for Fuel Cell Applications. Acc. Chem. Res. 2012, 45 (3), 473–481. https://doi.org/10.1021/ar200201x.

(73) Wang, J.; Li, S.; Zhang, S. Novel Hydroxide-Conducting Polyelectrolyte Composed of an Poly(Arylene Ether Sulfone) Containing Pendant Quaternary Guanidinium Groups for Alkaline Fuel Cell Applications. Macromolecules 2010, 43 (8), 3890–3896. https://doi.org/10.1021/ma100260a.

(74) Gu, S.; Cai, R.; Luo, T.; Jensen, K.; Contreras, C.; Yan, Y. Quaternary Phosphonium-Based Polymers as Hydroxide Exchange Membranes. ChemSusChem 2010, 3 (5), 555–558. https://doi.org/10.1002/cssc.201000074.

(75) Arges, C. G.; Parrondo, J.; Johnson, G.; Nadhan, A.; Ramani, V. Assessing the Influence of Different Cation Chemistries on Ionic Conductivity and Alkaline Stability of Anion Exchange Membranes. J. Mater. Chem. 2012, 22 (9), 3733. https://doi.org/10.1039/c2jm14898f.

(76) Arges, C. G.; Zhang, L. Anion Exchange Membranes' Evolution toward High Hydroxide Ion Conductivity and Alkaline Resiliency. ACS Appl. Energy Mater. 2018, 1 (7), 2991–3012. https://doi.org/10.1021/acsaem.8b00387.

(77) Weissbach, T.; Wright, A. G.; Peckham, T. J.; Sadeghi Alavijeh, A.; Pan, V.; Kjeang, E.; Holdcroft, S. Simultaneous, Synergistic Control of Ion Exchange Capacity and Cross-Linking of Sterically-Protected Poly(Benzimidazolium)s. Chem. Mater. 2016, 28 (21), 8060–8070. https://doi.org/10.1021/acs.chemmater.6b03902.

(78) Kienitz, B.; Kolde, J.; Priester, S.; Baczkowski, C.; Crum, M. Ultra-Thin Reinforced Ionomer Membranes to Meet Next Generation Fuel Cell Targets. ECS Trans. 2011, 41 (1), 1521–1530. https://doi.org/10.1149/1.3635683.

(79) Li, M.; Scott, K. A Polymer Electrolyte Membrane for High Temperature Fuel Cells to Fit Vehicle Applications. Electrochimica Acta 2010, 55 (6), 2123–2128. https://doi.org/10.1016/j.electacta.2009.11.044.

(80) Zhao, Y.; Yu, H.; Yang, D.; Li, J.; Shao, Z.; Yi, B. High-Performance Alkaline Fuel Cells Using Crosslinked Composite Anion Exchange Membrane. J. Power Sources 2013, 221, 247–251. https://doi.org/10.1016/j.jpowsour.2012.08.053.

(81) Wang, X.; Li, M.; Golding, B. T.; Sadeghi, M.; Cao, Y.; Yu, E. H.; Scott, K. A Polytetrafluoroethylene-Quaternary 1,4-Diazabicyclo-[2.2.2]-Octane Polysulfone Composite Membrane for Alkaline Anion Exchange Membrane Fuel Cells. Int. J. Hydrog. Energy 2011, 36 (16), 10022–10026. https://doi.org/10.1016/j.ijhydene.2011.05.054.

(82) Park, A. M.; Turley, F. E.; Wycisk, R. J.; Pintauro, P. N. Electrospun and Cross-Linked Nanofiber Composite Anion Exchange Membranes. Macromolecules 2014, 47 (1), 227–235. https://doi.org/10.1021/ma401932h.

(83) Wright, A. G.; Holdcroft, S. SI: Hydroxide-Stable Ionenes. ACS Macro Lett. 2014, 3 (5), 444–447. https://doi.org/10.1021/mz500168d.

(84) Fan, J.; Wright, A. G.; Britton, B.; Weissbach, T.; Skalski, T. J. G.; Ward, J.; Peckham, T. J.; Holdcroft, S. Cationic Polyelectrolytes, Stable in 10 M KOHaq at 100 °C. ACS Macro Lett. 2017, 6 (10), 1089–1093. https://doi.org/10.1021/acsmacrolett.7b00679.

(85) Gangrade, A. S.; Cassegrain, S.; Chandra Ghosh, P.; Holdcroft, S. Permselectivity of Ionene-Based, Aemion® Anion Exchange Membranes. J. Membr. Sci. 2022, 641 (July 2021), 119917–119928. https://doi.org/10.1016/j.memsci.2021.119917.

(86) Ferreira, T.; Rasband, W. ImageJ User Guide.

(87) Williams, M. V.; Kunz, H. R.; Fenton, J. M. Analysis of Polarization Curves to Evaluate Polarization Sources in Hydrogen/Air PEM Fuel Cells. J. Electrochem. Soc. 2005, 152 (3), A635. https://doi.org/10.1149/1.1860034.

(88) Cooper, K. R. Progress Toward Accurate Through-Plane Ion Transport Resistance Measurement of Thin Solid Electrolytes. J. Electrochem. Soc. 2010, 157 (11), B1731. https://doi.org/10.1149/1.3481561.

(89) Cooper, K. R. Progress toward Accurate Through-Plane Ion Transport Resistance Measurement of Thin Solid Electrolytes. J. Electrochem. Soc. 2010, 157 (11). https://doi.org/10.1149/1.3481561.

(90) Soboleva, T.; Xie, Z.; Shi, Z.; Tsang, E.; Navessin, T.; Holdcroft, S. Investigation of the Through-Plane Impedance Technique for Evaluation of Anisotropy of Proton Conducting Polymer Membranes. J. Electroanal. Chem. 2008, 622 (2), 145–152. https://doi.org/10.1016/j.jelechem.2008.05.017.

(91) Kusoglu, A.; Weber, A. Z. New Insights into Perfluorinated Sulfonic-Acid Ionomers. Chem. Rev. 2017, 117 (3), 987–1104. https://doi.org/10.1021/acs.chemrev.6b00159.

(92) Alberti, G.; Narducci, R. Evolution of Permanent Deformations (or Memory) in Nafion 117 Membranes with Changes in Temperature, Relative Humidity and Time, and Its Importance in the Development of Medium Temperature PEMFCs. Fuel Cells 2009, 9 (4), 410–420. https://doi.org/10.1002/fuce.200800148.

(93) Kimura, T.; Yamazaki, Y. Effects of CO2 Concentration and Electric Current on the Ionic Conductivity of Anion Exchange Membranes for Fuel Cells. Electrochemistry 2011, 79 (2), 94–97. https://doi.org/10.5796/electrochemistry.79.94.

(94) Lu, S.; Pan, J.; Huang, A.; Zhuang, L.; Lu, J. Alkaline Polymer Electrolyte Fuel Cells Completely Free from Noble Metal Catalysts.

(95) Suzuki, S.; Muroyama, H.; Matsui, T.; Eguchi, K. Influence of CO2 Dissolution into Anion Exchange Membrane on Fuel Cell Performance. Electrochimica Acta 2013, 88, 552–558. https://doi.org/10.1016/j.electacta.2012.10.105.

(96) Li, G.; Wang, Y.; Pan, J.; Han, J.; Liu, Q.; Li, X.; Li, P.; Chen, C.; Xiao, L.; Lu, J.; Zhuang, L. Carbonation Effects on the Performance of Alkaline Polymer Electrolyte Fuel Cells. Int. J. Hydrog. Energy 2015, 40, 6655–6660. https://doi.org/10.1016/j.ijhydene.2015.03.119.

(97) Marino, M. G.; Melchior, J. P.; Wohlfarth, A.; Kreuer, K. D. Hydroxide, Halide and Water Transport in a Model Anion Exchange Membrane. J. Membr. Sci. 2014, 464, 61–71. https://doi.org/10.1016/j.memsci.2014.04.003.

(98) Krewer, U.; Weinzierl, C.; Ziv, N.; Dekel, D. R. Impact of Carbonation Processes in Anion Exchange Membrane Fuel Cells. Electrochimica Acta 2018, 263, 433–446. https://doi.org/10.1016/j.electacta.2017.12.093.

(99) Ziv, N.; Mustain, W. E.; Dekel, D. R. The Effect of Ambient Carbon Dioxide on Anion-Exchange Membrane Fuel Cells. ChemSusChem 2018, 11, 1136–1150. https://doi.org/10.1002/cssc.201702330.

(100) Dekel, D. R. Review of Cell Performance in Anion Exchange Membrane Fuel Cells. J. Power Sources 2018, 375, 158–169. https://doi.org/10.1016/j.jpowsour.2017.07.117.

(101) Adams, L. A.; Poynton, S. D.; Tamain, C.; Slade, R. C. T.; Varcoe, J. R. A Carbon Dioxide Tolerant Aqueous-Electrolyte-Free Anion-Exchange Membrane Alkaline Fuel Cell. ChemSusChem 2008, 1, 79–81. https://doi.org/10.1002/cssc.200700013.

(102) S. Watanabe, K. F. and H. Y. Determination of Carbonate Ion in MEA During the Alkaline Membrane Fuel Cell(AMFC) Operation. ECS Trans. 2010, 33, 1837–1845.

(103) Siroma, Z.; Watanabe, S.; Yasuda, K.; Fukuta, K.; Yanagi, H. Mathematical Modeling of the Concentration Profile of Carbonate Ions in an Anion Exchange Membrane Fuel Cell. J. Electrochem. Soc. 2011, 158, B682. https://doi.org/10.1149/1.3576120.

(104) Ziv, N.; Dekel, D. R. A Practical Method for Measuring the True Hydroxide Conductivity of Anion Exchange Membranes. Electrochem. Commun. 2018, 88, 109–113. https://doi.org/10.1016/j.elecom.2018.01.021.

(105) Guo, J.; Qiu, L.; Deng, Z.; Yan, F. Plastic Reusable pH Indicator Strips: Preparation via Anion-Exchange of Poly(Ionic Liquids) with Anionic Dyes. Polym. Chem. 2013, 4, 1309–1312. https://doi.org/10.1039/c2py21076b.

(106) Wright, A. G.; Holdcroft, S. Hydroxide-Stable Ionenes. ACS Macro Lett. 2014, 3, 444–447. https://doi.org/10.1021/mz500168d.

(107) Wright, A. G.; Fan, J.; Britton, B.; Weissbach, T.; Lee, H. F.; Kitching, E. A.; Peckham, T. J.; Holdcroft, S. Hexamethyl-: P -Terphenyl Poly(Benzimidazolium): A Universal Hydroxide-Conducting Polymer for Energy Conversion Devices. Energy Environ. Sci. 2016, 9, 2130–2142. https://doi.org/10.1039/c6ee00656f.

(108) Thomas J. Bruno and Paris D. N. Svoronos. Indicators for Acids and Bases. CRC Handb. Chem. Phys. 2016, 8–88.

(109) Suzuki, C. Making Colorful Patterns on Paper Dyed with Red Cabbage Juice. J. Chem. Educ. 1991, 68 (7), 588. https://doi.org/10.1021/ed068p588.

(110) Crippa, M.; Janssens-Maenhout, G.; Dentener, F.; Guizzardi, D.; Sindelarova, K.; Muntean, M.; Van Dingenen, R.; Granier, C. Forty Years of Improvements in European Air Quality: Regional Policy-Industry Interactions with Global Impacts. Atmospheric Chem. Phys. 2016, 16 (6), 3825–3841. https://doi.org/10.5194/acp-16-3825-2016.

(111) Klimont, Z.; Kupiainen, K.; Heyes, C.; Purohit, P.; Cofala, J.; Rafaj, P.; Borken-Kleefeld, J.; Schöpp, W. Global Anthropogenic Emissions of Particulate Matter Including Black Carbon. Atmospheric Chem. Phys. 2017, 17 (14), 8681–8723. https://doi.org/10.5194/acp-17-8681-2017.

(112) Tong, D.; Zhang, Q.; Davis, S. J.; Liu, F.; Zheng, B.; Geng, G.; Xue, T.; Li, M.; Hong, C.; Lu, Z.; Streets, D. G.; Guan, D.; He, K. Targeted Emission Reductions from Global Super-Polluting Power Plant Units. Nat. Sustain. 2018, 1 (1), 59–68. https://doi.org/10.1038/s41893-017-0003-y.

(113) Net Zero by 2050 - A Roadmap for the Global Energy Sector.

(114) Piana, M.; Boccia, M.; Filpi, A.; Flammia, E.; Miller, H. A.; Orsini, M.; Salusti, F.; Santiccioli, S.; Ciardelli, F.; Pucci, A. H2/Air Alkaline Membrane Fuel Cell Performance and Durability, Using Novel Ionomer and Non-Platinum Group Metal Cathode Catalyst. J. Power Sources 2010, 195 (18), 5875–5881. https://doi.org/10.1016/j.jpowsour.2009.12.085.

(115) Wang, L.; Brink, J. J.; Liu, Y.; Herring, A. M.; Ponce-González, J.; Whelligan, D. K.; Varcoe, J. R. Non-Fluorinated Pre-Irradiation-Grafted (Peroxidated) LDPE-Based Anion-Exchange Membranes with High Performance and Stability. Energy Environ. Sci. 2017, 10 (10), 2154–2167. https://doi.org/10.1039/C7EE02053H.

(116) Siroma, Z.; Watanabe, S.; Yasuda, K.; Fukuta, K.; Yanagi, H. Mathematical Modeling of the Concentration Profile of Carbonate Ions in an Anion Exchange Membrane Fuel Cell. J. Electrochem. Soc. 2011, 158 (6), B682–B689. https://doi.org/10.1149/1.3576120.

(117) Bohra, D.; Chaudhry, J. H.; Burdyny, T.; Pidko, E. A.; Smith, W. A. Modeling the Electrical Double Layer to Understand the Reaction Environment in a CO 2 Electrocatalytic System. Energy Environ. Sci. 2019, 12 (11), 3380–3389. https://doi.org/10.1039/C9EE02485A.

(118) Ma, M.; Clark, E. L.; Therkildsen, K. T.; Dalsgaard, S.; Chorkendorff, I.; Seger, B. Insights into the Carbon Balance for CO 2 Electroreduction on Cu Using Gas Diffusion Electrode Reactor Designs. Energy Environ. Sci. 2020, 13 (3), 977–985. https://doi.org/10.1039/D0EE00047G.

(119) Liu, M.; Pang, Y.; Zhang, B.; De Luna, P.; Voznyy, O.; Xu, J.; Zheng, X.; Dinh, C. T.; Fan, F.; Cao, C.; De Arquer, F. P. G.; Safaei, T. S.; Mepham, A.; Klinkova, A.; Kumacheva, E.; Filleter, T.; Sinton, D.; Kelley, S. O.; Sargent, E. H. Enhanced Electrocatalytic CO2 Reduction via Field-Induced Reagent Concentration. Nature 2016, 537 (7620), 382–386. https://doi.org/10.1038/nature19060.

(120) Vega, J. A.; Mustain, W. E. Effect of CO2, HCO3− and CO3−2 on Oxygen Reduction in Anion Exchange Membrane Fuel Cells. Electrochimica Acta 2010, 55 (5), 1638–1644. https://doi.org/10.1016/j.electacta.2009.10.041.

(121) Grew, K. N.; Chiu, W. K. S. A Dusty Fluid Model for Predicting Hydroxyl Anion Conductivity in Alkaline Anion Exchange Membranes. J. Electrochem. Soc. 2010, 157 (3), B327. https://doi.org/10.1149/1.3273200.

(122) Zhang, Z.; Melo, L.; Jansonius, R. P.; Habibzadeh, F.; Grant, E. R.; Berlinguette, C. P. pH Matters When Reducing CO 2 in an Electrochemical Flow Cell. ACS Energy Lett. 2020, 5 (10), 3101–3107. https://doi.org/10.1021/acsenergylett.0c01606.

(123) Grew, K. N.; Ren, X.; Chu, D. Effects of Temperature and Carbon Dioxide on Anion Exchange Membrane Conductivity. Electrochem. Solid-State Lett. 2011, 14 (12), B127. https://doi.org/10.1149/2.011112esl.

(124) Krewer, U.; Weinzierl, C.; Ziv, N.; Dekel, D. R. Impact of Carbonation Processes in Anion Exchange Membrane Fuel Cells. Electrochimica Acta 2018, 263, 433–446. https://doi.org/10.1016/j.electacta.2017.12.093.

(125) Weng, L.-C.; Bell, A. T.; Weber, A. Z. Towards Membrane-Electrode Assembly Systems for CO 2 Reduction: A Modeling Study. Energy Environ. Sci. 2019, 12 (6), 1950–1968. https://doi.org/10.1039/C9EE00909D.

(126) Guo, J.; Qiu, L.; Deng, Z.; Yan, F. Plastic Reusable pH Indicator Strips: Preparation via Anion-Exchange of Poly(Ionic Liquids) with Anionic Dyes. Polym. Chem. 2013, 4 (5), 1309. https://doi.org/10.1039/c2py21076b.

(127) Wright, A. G.; Holdcroft, S. Hydroxide-Stable Ionenes. ACS Macro Lett. 2014, 3 (5), 444–447. https://doi.org/10.1021/mz500168d.

(128) Sabnis, R. W. Handbook of Acid-Base Indicators. CRC Press 2008.

(129) Lerf, C.; Suppan, P. Hydrogen Bonding and Dielectric Effects in Solvatochromic Shifts. J. Chem. Soc. Faraday Trans. 1992, 88 (7), 963. https://doi.org/10.1039/ft9928800963.

(130) Kubannek, F.; Zhegur-Khais, A.; Li, S.; Dekel, D. R.; Krewer, U. Model-Based Insights into the Decarbonation Dynamics of Anion-Exchange Membranes. Chem. Eng. J. 2023, 459, 141534. https://doi.org/10.1016/j.cej.2023.141534.

(131) Hohenadel, A.; Powers, D.; Wycisk, R.; Adamski, M.; Pintauro, P.; Holdcroft, S. Electrochemical Characterization of Hydrocarbon Bipolar Membranes with Varying Junction Morphology. ACS Appl. Energy Mater. 2019, 2 (9), 6817–6824. https://doi.org/10.1021/acsaem.9b01257.